Shallow Mixing Layers

Ondiepe Menglagen

STELLINGEN
behorende bij het proefschrift
Ondiepe Menglagen
van
Bram van Prooijen
Delft, 1 maart 2004

1. Het snelheidsverschil over en de breedte van een ondiepe menglaag bepalen niet de waarde, maar de groeisnelheid van de grootte en de intensiteit van horizontale coherente structuren in de menglaag.

Dit proefschrift.

2. Horizontale coherente structuren in een ondiepe menglaag komen voort uit grootschalige componenten van de bodemturbulentie.

Dit proefschrift.

3. Voor de voorspelling van de breedteontwikkeling van de menglaag is gedetailleerde kennis over de ontwikkeling van horizontale coherente structuren in de menglaag niet noodzakelijk.

Dit proefschrift.

4. De impulsoverdracht tussen de hoofdgeul en de uiterwaard van een rivier wordt niet bepaald door secundaire stroming.

Dit proefschrift,

in reactie op Shiono&Knight, Journal of Fluid Mechanics, Vol. 222, 1991.

5. Momentane stromingsgrootheden als de waterdiepte en de stroomsnelheid bepalen niet de waarde, maar de groeisnelheid van de hoogte van rivierduinen tijdens een hoogwatergolf.

In reactie op Julien & Klaassen, Journal of Hydraulic Engineering Vol.121(9),1995.

6. De kosten van de uitgifte van wetenschappelijke publicaties dienen niet verhaald te worden op de lezers, maar op de auteurs.

7. Wetenschappers hebben liever een verre vriend op hun eigen vakgebied dan een goede buur op een aanverwant vakgebied.

8. De complexiteit van de presentatie van een computersimulatie is een goede indicatie voor de onnauwkeurigheid van de simulatie.

9. Vanwege de grote draagwijdte van lage tonen en de geringe draagwijdte van hoge tonen wordt de uit auto's afkomstige moderne popmuziek te vaak als eentonig bestempeld.

10. Het als zodanig studeren van hoge noten (hoger dan g3) op een trompet is vergeefse moeite. Het uit den treure studeren van lage noten (lager dan $f^\#0$) geeft uiteindelijk het beoogde resultaat.

Deze stellingen worden verdedigbaar geacht en zijn als zodanig goedgekeurd door de promotor prof. dr ir J.A. Battjes.

PROPOSITIONS
additional to the thesis
Shallow Mixing Layers
of
Bram van Prooijen
Delft, 1 March 2004

1. The velocity difference over and the width of a shallow mixing layer do not determine the values but the growth rates of the size and intensity of horizontal coherent structures in the mixing layer.

<div align="right">This thesis.</div>

2. Horizontal coherent structures in a shallow mixing layer are initiated by large scale components of the bottom turbulence.

<div align="right">This thesis.</div>

3. Detailed knowledge of the development of horizontal coherent structures is not required for the prediction of the development of the width of a shallow mixing layer.

<div align="right">This thesis.</div>

4. The momentum exchange between the main channel and the flood plain of a compound channel is not dominated by secondary circulations.

<div align="right">This thesis,</div>

<div align="right">in response to Shiono & Knight, Journal of Fluid Mechanics Vol. 222, 1991.</div>

5. Instantaneous flow quantities like the water depth and the velocity do not determine the value but the growth rate of the height of river dunes.

   In response to Julien&Klaassen, Journal of Hydraulic Engineering Vol.121(9), 1995.

6. The publication costs of scientific journals should be borne by the authors rather than by the readers.

7. Scientists prefer a distant friend in their own field to a neighbour in a related research area.

8. The complexity of the presentation of a computer simulation is a good indication of the inaccuracy of that simulation.

9. Because low tones travel farther than high tones, modern popular music, emanating from cars, is too often labeled monotonous.

10. Practicing high blowing on a trumpet (above g3) by trying to play high notes is a waste of time. The desired goal is better achieved by long term practice on pedal tones (lower than $f^\#0$).

These propositions are considered defendable and as such have been approved by the supervisor prof. dr ir J.A. Battjes.
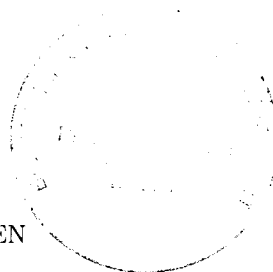
Shallow Mixing Layers

Proefschrift

ter verkrijging van de graad van doctor
aan de Technische Universiteit Delft,
op gezag van de Rector Magnificus prof. dr ir J.T. Fokkema,
voorzitter van het College voor Promoties,
in het openbaar te verdedigen op maandag 1 maart 2004 om 15.30 uur

door

Bram Christiaan VAN PROOIJEN
civiel ingenieur
geboren te 's-Gravenhage

Dit proefschrift is goedgekeurd door de promotor:
   Prof. dr ir J.A. Battjes

Toegevoegd promotor:
   Dr ir W.S.J. Uijttewaal

Samenstelling promotiecommissie:
   Rector Magnificus,   voorzitter
   Prof. dr ir J.A. Battjes   Technische Universiteit Delft, promotor
   Dr ir W.S.J. Uijttewaal   Technische Universiteit Delft, toegevoegd promotor
   Prof. dr ir H.J. de Vriend   Technische Universiteit Delft
   Prof. dr ir A.E. Mynett   UNESCO-IHE, Delft
   Prof. dr ir G.J.F. van Heijst   Technische Universiteit Eindhoven
   Prof. dr G.H. Jirka   Universität Karlsruhe, Duitsland
   Prof. dr P.K. Stansby   University of Manchester Institute for Science and Technology,
                                       Groot-Brittanië.

"At the time we were all convinced that we must talk and talk and write and publish as quickly as possible, and as much as possible, and that this was all necessary for the good of mankind. And thousands of us, contradicting and abusing one another, published and wrote with the aim of teaching others. Failing to notice that we knew nothing, that we did not know the answer to the most basic question of life - what is good and what is evil - we all spoke at the same time, never listening to one another. At times we indulged and praised each other in order to be indulged and praised in return, at other times we grew angry and shrieked at each other, just as if we were in a madhouse".

Leo Tolstoy (1882)
A Confession and Other Religious Writings.
tr. Jane Kentish. London: Penguin Books, 1987.

Abstract

At the confluence of two parallel streams with different velocities a mixing layer develops. If the flow domain is bounded by a bottom and a free surface and the width of the mixing region is large compared to the water depth, we deal with a shallow mixing layer. Horizontal coherent structures with dimensions of the order of the mixing layer width develop in the mixing layer due to instabilities in the transverse shear flow. The bottom boundary layer gives rise to turbulence with dominant length scales in the order of the water depth. This bottom turbulence dissipates energy of the horizontal coherent structures.

Shallow shear flows are often found in the natural environment. Examples are: the confluence of rivers, compound channel flows, wakes behind islands, or flow in groyne fields. As shallow flows accommodate a variety of functions, like navigation, disposal for waste water and drinking water intakes, and as the surroundings have to be protected against flooding, there is a need for reliable models predicting these flows.

In this thesis the development of shallow mixing layer flow and its coherent structures is studied using three methodologies: experiments, analytical modeling, and numerical modeling. The aim is to obtain better insights in the development of shallow mixing layers and to translate these insights into reliable modeling tools.

Experiments are carried out for two flow conditions, differing in water depth. Particle Tracking Velocimetry is performed resulting in timeseries of two-dimensional surface velocity maps. From the mean streamwise velocity data the characteristic properties of the downstream development of a shallow mixing layer were determined: the decrease of the velocity difference, the non-linear widening of the mixing layer and the shift of the mixing layer to the low velocity side. The high turbulence intensities indicate a large momentum transfer in the mixing zone. In this region, significant peaks were found in the energy density spectra, representing the large scale horizontal coherent structures. By means of an eduction method based on pattern recognition, the coherent structures could be detected and conditionally averaged. The mean flow, the turbulence intensities and the conditionally averaged vortices are used later on for validation of the analytical and numerical models.

The analytical modeling consists of two parts. First, the mean streamwise velocity is modeled. The concept of self-similarity is used for determination of the transverse profile of the streamwise velocity. Subsequently the downstream development of the velocity difference, the velocity in the center of the mixing layer, the mixing layer width and the lateral shift of the mixing layer were determined, resulting in a closed set of equations for the mean velocity field, with the entrainment coefficient as the only remaining constant. A good agreement was found between the modeled velocity fields and the measured ones. Second, the downstream development of the coherent structures is determined. Linear stability analysis has been used for the determination of the growth rates of instabilities for the velocity profiles as found by the self-similarity model. By integrating the growth rates for each wavenumber in downstream direction, the energy densities at each downstream position could be determined, for given energy density spectra at the inflow. The energy density spectra so obtained compared well with the measurements, despite the assumption

of linear behavior.

Validity of the linear theory for the development of the coherent structures has the important consequence that the intensity of the coherent structures depends on the energy density level of the perturbations at the inflow boundary. This hypothesis has been validated using a numerical model, in which the large scale depth averaged motion is resolved while the small scale bottom turbulence is modeled by means of an eddy viscosity concept. Computations are performed with perturbations of different energy density levels at the inflow. Analogous to the linear analytical model, the perturbations at the inflow condition were required for the numerical simulations as well. The necessary large scale perturbations were associated with the large scale components of the bottom turbulence.

In order to determine the properties of the large scale motions, a fully three-dimensional Large Eddy Simulation of a wide uniform open channel flow has been performed. In this simulation the spectrum of the length scales associated with bottom turbulence is resolved for the greater part. Averaging over the depth resulted in the required components of the bottom turbulence. This depth-averaged motion is subsequently mimicked by means of a kinematic simulation, which is implemented as a forcing term in the two-dimensional shallow-water equations resulting in the 2D-TRANS+ks model. This model has been validated using the data sets of the two measured shallow mixing layers. The mean flow properties were well represented, but some discrepancies were found between the measured and simulated intensities of the horizontal coherent structures. In addition to the developing mixing layer, the model has been applied to a compound channel flow with lateral roughness variation. This qualitative analysis confirmed the need for an implementation of the forcing terms as proposed in the 2D-TRANS+ks model.

The findings of this study are extended also to the flow in a straight uniform compound channel with transverse depth variation, described in Appendix I. A new physically based model is presented for the transverse exchange of streamwise momentum. The model takes into account the effects of bottom turbulence and horizontal coherent structures. Special attention was paid to the effect of the depth variation on the dynamics of the horizontal coherent structures. A comparison with experimental data from literature confirmed the validity of the model.

New insights have been obtained in the development of shallow mixing layers and the coherent structures therein. Quick and simple tools have been developed for a rough prediction of the mean streamwise velocity and the development of the coherent structures. For a more detailed description of shallow mixing layers, the developed numerical model 2D-TRANS+ks is recommended.

Samenvatting

Wanneer twee parallele stromen met verschillende snelheden samenvloeien ontwikkelt zich tussen de stromen een menglaag, waarin impuls wordt overgedragen van de hoge naar de lage snelheidszijde. We spreken van een ondiepe menglaag als de stroming hoofdzakelijk horizontaal is en beperkt wordt door de bodem en het vrij wateroppervlak, zo dat de breedte van de menglaag groot is ten opzichte van de opgelegde waterdiepte. Grootschalige horizontale wervels, coherente structuren, kunnen ontstaan in een dergelijke ondiepe menglaag. Deze worden gevoed door het snelheidsverschil. Naast de grootschalige wervels is er kleinschalige turbulentie met lengteschalen in de orde van grootte van de waterdiepte. Deze zogenaamde bodemturbulentie speelt een belangrijke rol in de ontwikkeling van de grootschalige wervels.

Ondiepwaterstromingen waarin een horizontaal snelheidsverschil een rol speelt komen op vele plaatsen voor. Voorbeelden zijn: de samenvloeiïng van rivieren; de stroming in rivieren bestaande uit een hoofdgeul en uiterwaarden; zogstroming achter een eiland en kribvakstroming. Ondiepwaterstromingen zoals rivieren en estuaria vervullen vaak een groot aantal functies, zoals scheepvaart; lozing van afval- en koelwater; aanvoer van gebruikswater. Bovendien vormt ondiep water een belangrijke ecologische functie en dient de omgeving tegen overstromingen beschermd te worden. Er is daarom een behoefte aan betrouwbare modellen voor de voorspelling van ondiep-waterstroming.

In dit proefschrift wordt de ondiepe menglaag onderzocht aan de hand van drie verschillende methoden: laboratorium experimenten, analytische modellering en numerieke modellering. Het doel van deze studie is om meer inzicht te krijgen in de ontwikkeling van ondiepe menglagen en om de inzichten te vertalen naar een betrouwbaar modelinstrumentarium.

Twee experimenten zijn uitgevoerd met verschillende stromingscondities. *Particle Tracking Velocimetry* is gebruikt als meetmethode, resulterend in tijdreeksen van snelheidsvelden van de oppervlaktesnelheid. Op basis van de tijdsgemiddelde snelheidsvelden zijn de volgende karakteristieke eigenschappen van de stroming bepaald: de afname van het snelheidsverschil tussen de twee parallelle stromen, de niet-lineaire verbreding van de menglaag en de verschuiving van het centrum van de menglaag naar de lage- snelheidszijde. De hoge turbulentie-intensiteiten in de menglaag wijzen op een verhoogde impulsoverdracht in de menglaag. Een sterke piek in de energiedichtheidsspectra representeert grootschalige coherente structuren. Met behulp van een patroonherkenningstechniek zijn deze gedetecteerd, resulterend in conditioneel gemiddelde wervels. De gemiddelde snelheid, de turbulentie-intensiteit, en de conditioneel gemiddelde wervels zijn later in dit proefschrift gebruikt voor de validatie van analytische en numerieke modellen.

De analytische modellering is gesplitst in twee onderdelen. Ten eerste is de gemiddelde snelheid gemodelleerd. Het gelijkvormigheidsprincipe is gebruikt voor de bepaling van het dwarsprofiel van de snelheid in de stroomrichting. Daartoe is een stelsel vergelijkingen afgeleid voor de benedenstroomse ontwikkeling van het laterale snelheidsverschil, de menglaagbreedte en de verschuiving van het centrum van de menglaag met een dimensieloze *entrainment* factor als enig overblijvende empirische constante. Bij gebruikmaking

van een realistische, uit de literatuur bekende waarde voor deze constante wordt een goede overeenkomst gevonden tussen de gemodelleerde en de gemeten snelheidsvelden.

Ten tweede is de stroomafwaartse ontwikkeling van de coherente structuren bepaald. Er is gebruik gemaakt van lineaire stabiliteitsanalyse voor de bepaling van de groeisnelheden van instabiliteiten behorend bij de reeds bepaalde snelheidsprofielen. Integratie van de groeisnelheden, per golfgetal, in stroomafwaartse richting geeft de lokale energiedichtheid voor een gegeven energiedichtheid op de instroomrand. Ondanks de ruwe aanname van lineair gedrag blijken de gemodelleerde energiedichtheidsspectra redelijk goed overeen te komen met de gemeten energiedichtheidsspectra.

De geldigheid van de lineaire theorie voor de ontwikkeling van grootschalige wervels heeft de belangrijke consequentie dat de intensiteit van de coherente structuren afhangt van de energiedichtheid van bovenstrooms opgelegde perturbaties. Deze hypothese is gevalideerd met een numeriek model, waarin de grootschalige dieptegemiddelde waterbeweging is opgelost en waarin de kleinschalige bodemturbulentie is gemodelleerd met behulp van een turbulentiemodel. Evenals uit de analytische modellering bleek dat perturbaties op de instroomrand benodigd zijn voor de simulatie van grootschalige wervels.

Om te bepalen welke perturbaties op de instroomrand opgelegd dienen te worden is een volledig driedimensionale simulatie van een kanaalstroming uitgevoerd, waarbij de domeinlengte en -breedte vele malen groter zijn dan de waterdiepte. In deze simulatie wordt de bodemturbulentie grotendeels opgelost. Middeling van de snelheden over de diepte geeft de benodigde dieptegemiddelde fluctuaties. Deze fluctuaties zijn vervolgens nagebootst met behulp van een kinematische simulatie. Ten slotte zijn de nagebootste fluctuaties geïmplementeerd in de tweedimensionale ondiep-watervergelijkingen, resulterend in het zogenaamde 2D-TRANS+ks model. Dit model is getoetst aan de hand van de gegevens verkregen uit de laboratoriumexperimenten. De gemiddelde snelheid werd goed gerepresenteerd, maar verschillen werden gevonden tussen de gemeten en de gemodelleerde coherente structuren. Naast de samenvloeiïng van twee parallelle stromen is het model toegepast voor een stromingssituatie bestaande uit een kanaal met ruwheidsvariatie in de dwarsrichting. Uit een kwalitatieve analyse van de resultaten bleek de noodzaak van de implementatie van de perturbatietermen, zoals voorgesteld in het 2D-TRANS+ks model.

In Appendix A wordt een nieuw model beschreven voor de impulsoverdracht tussen de hoofdgeul en de uiterwaard in een samengesteld kanaal. Dit model houdt rekening met de effecten van bodemturbulentie en grootschalige horizontale wervels. Speciale aandacht is besteed aan de effecten van de dieptevariatie op de grootschalige wervels. Het ontwikkelde model is getoetst aan de hand van meetgegevens uit de literatuur.
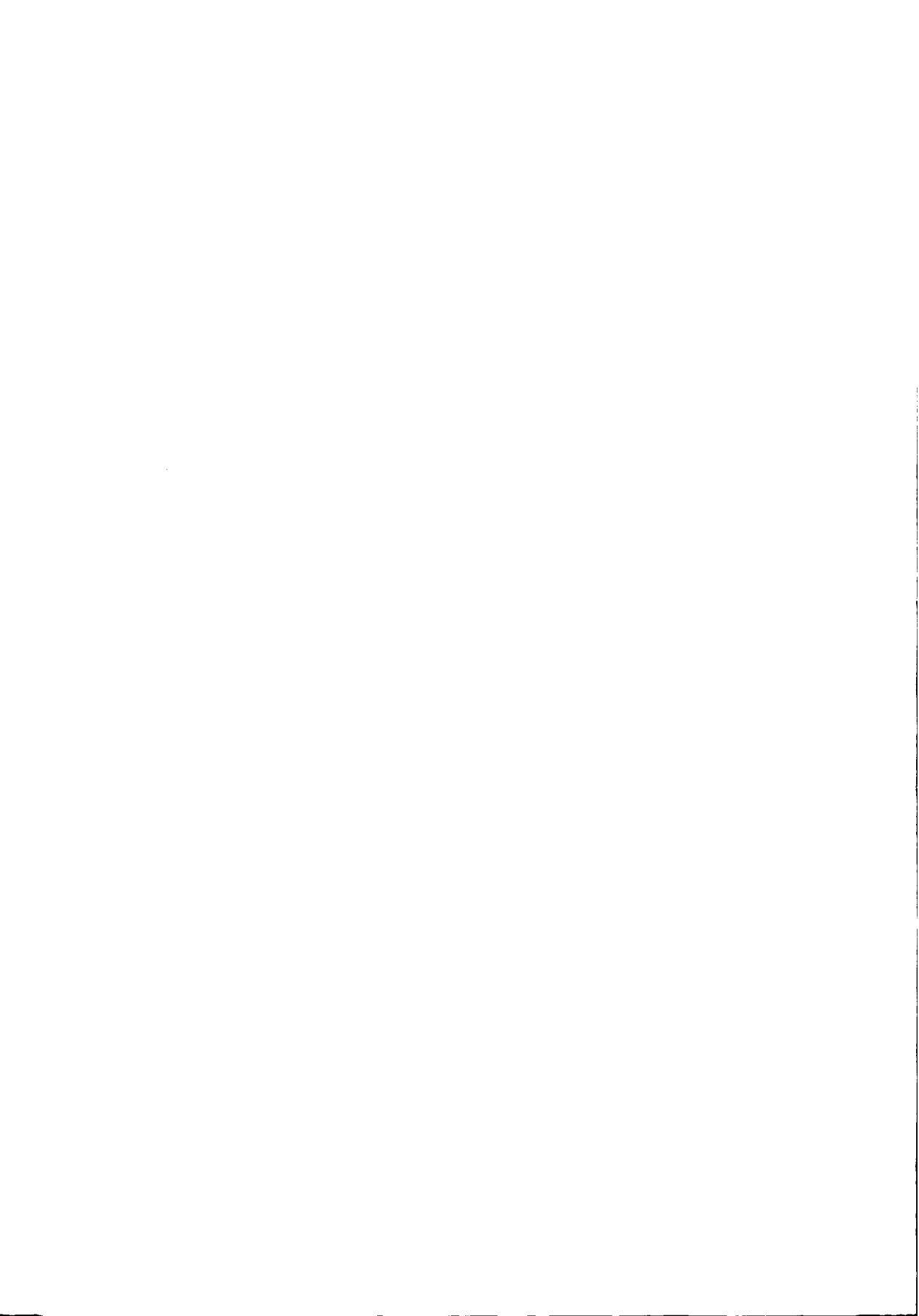
In deze studie zijn nieuwe inzichten verkregen in de ontwikkeling van de ondiepe menglaag en de grootschalige horizontale wervelstructuren. Snelle en eenvoudige methoden zijn ontwikkeld voor een ruwe schatting van de gemiddelde snelheid en de ontwikkeling van de structuren. Voor een meer gedetailleerde beschrijving van het stroomveld in een ondiepe menglaag wordt het numerieke model 2D-TRANS+ks aangeraden, waarbij de grootschalige wervels worden opgelost. Voorzichtigheid blijft echter geboden bij de toepassing van dit model in de prakijk der civiele techniek.

Contents

Chapter 1

Introduction

1.1   General

The shallow shear flows as addressed in this study are defined as turbulent, predominantly two-dimensional flows with transverse gradients in the streamwise velocity and a water depth that is small with respect to the horizontal dimensions of the flow. The clearly visible and often spectacular phenomena associated with these flows have made them of interest for many years. One of the first studies known on shallow shear flows was carried out by Leonardo da Vinci to regulate the River Arno (Italy) partly in order to make a navigable connection from the city Florence to the Mediterranean Sea. His idea was to regulate the river by means of spurdikes such that the water depth remains suitable for sailing. An example of such spurdikes is shown in Figure 1.1. The dams confine the flow and relatively high velocities are reached in the opening. Downstream of the largest dam a steady circulation is present. This gyre is fed by the momentum exchange in the mixing layer between the flow through the gap and the gyre. It can be seen from the details in the figure that in the mixing layer coherent structures develop. They are small just downstream of the dam and grow to sizes probably much larger than the water depth, and they eventually dissipate.

Figure 1.1: Drawing of the river regulation dams and the flow in the River Arno (Italy) by Leonardo Da Vinci (Barbera, 1983).

Nowadays, shallow flows as found in rivers, estuaries or coastal seas accommodate a variety of functions. The waters are for example used for navigation; the surrounding land has to be protected against floods; drinking water might be extracted; wastewater can be discharged; the waters might be used for swimming and the waters often have an important ecological function. These different functions are often conflicting. Interventions in the system require a careful approach. As the functions are strongly related to the dynamics of the flow, reliable models are required to predict the flow. Such a set of models should range from simple tools that can be used in the early stages of the design, to sophisticated numerical models for a detailed description of the flow in the final stage. In order to develop and interpret the results of such models, understanding of the physical processes in shallow shear flows is indispensable.

1.2 Basic flow types

Shallow shear flows can be considered as a combination of two archetypes of flow. On the one hand, they are plane free shear flows and on the other hand shallow shear flows fall in the category of open-channel flows.

1.2.1 Plane free shear flows

Wakes, jets and mixing layers are the three important types of plane free shear flows, see for example Pope (2000). 'Free' implies that there is no influence of a wall and that the turbulence arises from the mean-flow gradients. As we consider shallow flows, we restrict ourselves to the plane types of free shear flows, contrary to for example asymmetric shear flows. The flows are uni-directional and have a transverse gradient in the streamwise velocity. As an example, the velocity profile of a mixing layer is given in Figure 1.2a. Traveling with the flow in downstream direction, momentum is transferred from the high velocity side to the low velocity side resulting in a wider mixing region, and a smaller velocity gradient. This exchange is caused by the turbulent motion. The shape of the profile turns out to be maintained, such as an error- or tanh-profile in case of a mixing layer. The mean velocity field is thus determined by the velocity difference across the mixing layer and the width of the mixing layer. This concept of modeling is referred to as the self-similarity concept (Townsend, 1976). Plane wake flows and plane jets can be described similarly.

The transverse gradient in the streamwise velocity makes the flow unstable. According to Fjortofts theorem (Drazin & Reid, 1981), instability is reached in case of an inflection point in the transverse profile. Kelvin Helmholtz instabilities can therefore develop leading to the horizontal structures as visualized in Figure 1.1 and 1.3. One of the earliest experimental proofs of such vortices was the visualization by Flügel (1939) [1]. Vortical structures were presented with length scales in the order of magnitude of the mixing layer

---

[1]The development of the coherent structures is comparable to the more famous, but later published, visualizations of Brown&Roshko (1974)

(A) MIXING LAYER FLOW (TOP VIEW)

(B) WALL FLOW (SIDE VIEW)
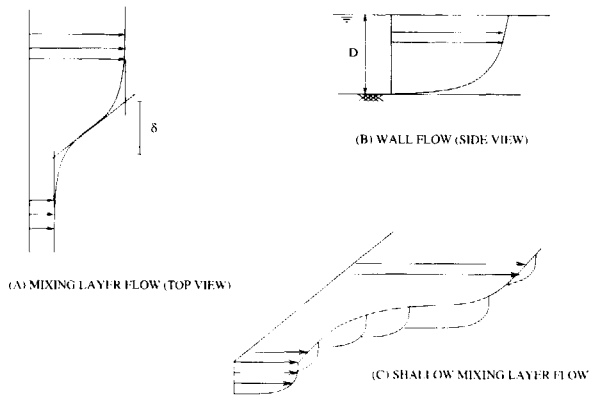
(C) SHALLOW MIXING LAYER FLOW

Figure 1.2: Profiles of the mean streamwise velocity.

width. With the use of linear stability analysis. parameters like the wavenumber of the most unstable mode and growth rates could be determined to some extent (Michalke, 1964; Michalke, 1965; Drazin & Reid, 1981).

Extensive numerical studies on plane shear flows (see for example Vreman (1995), Lesieur (1997), Balaras *et al.* (2001)) and experimental studies (see for example Brown&Roshko (1974), Winant&Browand (1974), Oster&Wygnanski (1982), Zhou&Wygnanski (2001)) have been carried out, resulting in more insights in the dynamics of the coherent structures.

1.2.2 Open-channel flow

Here we consider open-channel flows, i.e. turbulent wall flows with a free surface, extending over the full water depth. A review of open-channel flow can be found in Nezu&Nakagawa (1993). A typical vertical profile of the streamwise velocity is sketched in Figure 1.2b. Due to the no-slip condition at the bottom the flow is slowed down and a velocity gradient is created, resulting in the well known logarithmic profile for the streamwise velocity. The turbulent motion is characterized by ejection and sweep events and is typically three-dimensional. The dominant length scales are assumed not to exceed the water depth, although this is only justified for vertical motions. Motions with larger length scales can be found in the horizontal directions, see for example Kim&Adrian (1999) and Chapter 5.

The effect of the bottom on the flow is two-fold. On the one hand the shear stress acts as a drag force on the total water body and results in lower streamwise velocities. On the other hand the bottom turbulence evoked by the vertical shear gives rise to an effective eddy viscosity, enabling an increased lateral transfer of momentum in case of lateral variations of the streamwise velocity.

1.2.3   Shallow free shear flows

Shallow free shear flows are a combination of a plane free shear flow and an open channel flow (see Figure 1.2c), which makes them interesting from the fluid mechanical point of view and complicated when it comes to precise predictions. Depending on the flow parameters the free shear flow will dominate or the wall flow will dominate. In the class of shallow flows, which we discuss here, neither the horizontal shear nor the bottom turbulence can be neglected. The flow configuration will possess the following characteristics:

- $\mathcal{L}/D \gg 1$ The flow is predominantly two-dimensional, yielding horizontal length scales ($\mathcal{L}$), like the diameter of the vortices, far exceeding the water depth D.

- $\mathcal{U} \simeq \mathcal{O}(u_*)$. The typical velocity scales associated with the horizontal vortices ($\mathcal{U}$) are in the order of magnitude of the friction velocity (u_*).

The anisotropy caused by the large horizontal length scales and the small vertical length scales has considerable consequences for the development of the coherent structures. In case of such a predominantly two-dimensional domain vortices cannot be stretched in the direction of their vorticity axes. This mechanism of 'vortex stretching' is very effective in three-dimensional turbulence in transferring energy to eddies of smaller length scales. As this mechanism is suppressed, horizontal eddies as found in two-dimensional turbulence are relatively large and long living. This is in contrast with fully three-dimensional deep-water free-shear flows, where vortices may break up due to instabilities in the vertical dimension (Vreman, 1995; Lesieur, 1997).

Shallow shear flows can be categorized in accordance with three vortex generation mechanisms (Jirka, 2001). The strongest type of generation mechanisms is referred to as *topographical forcing*. Coherent structures develop on the lee side of an object and are shed regularly. The well known example of this type of generation mechanism is the Von Karman vortex street in the wake of an island (Cramp *et al.*, 1991). Another example is the flow downstream of a spurdike. A somewhat weaker generation mechanism is defined as *internal transverse shear instabilities*. Hydrodynamic instabilities gradually grow due to a transverse gradient of the streamwise velocity into large scale coherent structures. The term internal is used to emphasize that there is no external forcing, like in the first type. Examples are shallow jets, shallow mixing layers (Figure 1.3) or compound channel flows. The weakest mechanism as mentioned is defined as *secondary instabilities of base flow*. Through upcascading processes the three-dimensional bottom turbulence might develop to large scale motion.

As soon as coherent structures are generated they develop depending on the production and dissipation mechanisms. The coherent structures are fed by the transverse shear and decay under the influence of bottom turbulence, partly noticeable as a bottom shear stress and partly as an effective eddy viscosity. This balance between the dissipation and the production of turbulent kinetic energy of the large scale horizontal motion was expressed for shallow mixing layers by Chu&Babarutsi (1988) in the bottom friction parameter:

$$S = c_f \frac{\delta}{D} \frac{U_c}{\Delta U}$$

with the bottom friction coefficient c_f, the width of the mixing layer δ, the water depth D, the velocity difference over the mixing layer ΔU and the center velocity U_c. Only the effect of shear stress of the bottom turbulence is accounted for and the effect of the turbulence viscosity was neglected. From a linear stability analysis, it was concluded that the flow would be stable for a bottom friction parameter larger than the critical value $S_c \simeq \mathcal{O}(0.1)$ and unstable for smaller values. Similarly, a wake parameter was proposed by Chen&Jirka (1995), which could categorize different types of wake formation.

Although a bottom friction or wake parameter allows to some extent for a classification of the flow type, it does not provide information on the dimensions and intensities of the large scale horizontal coherent structures.

One of the basic types of shallow free shear flows is investigated: the shallow mixing layer over a horizontal uniform bottom. Regarding the generation mechanism of coherent structures, this flow type falls in the category *internal transverse shear instabilities* (Jirka, 2001). Vortical structures are not shed from an obstacle, but they are expected to be generated by the shear instabilities. The omnipresent bottom turbulence is expected to play a role not only in the dissipation of horizontal eddies, but also in their generation.

The emphasis is put on a developing mixing layer, as found at the confluence of two streams. Although this flow type is chosen for its relatively simple properties, examples are readily found in the natural environment. In Figure 1.3, a satellite image of the confluence of the Padma and the Meghna (Bangladesh) is shown. As the rivers differ in color, the entrainment effects of the horizontal eddies is visualized. In addition to the developing shallow mixing layer, attention is paid to the streamwise uniform mixing layer flow in a shallow compound channel. The velocity difference in such a compound channel is caused by a lateral variation in depth and/or roughness.

Figure 1.3: Vortical structures at the confluence of the Padma and the Meghna (Ashworth *et al.*, 1996).

1.3   Objective and outline

We aim at a better understanding of the genesis and development of horizontal coherent structures in shallow mixing layers. The insights to be obtained should be translated into a set of modeling tools for the prediction of shallow shear flows.

Three methodologies of investigation are followed: laboratory experiments, theoretical analysis and numerical simulations. In Chapter 2 we start with laboratory experiments. These are carried out to identify the physical mechanisms and to validate analytical and numerical models later on. Two different developing shallow mixing layers are studied in order to investigate the influence of the water depth. Particle Tracking Velocimetry (PTV) is used as a measurement tool. With this technique the spatial structure of the large coherent structures can be captured. The mean flow, turbulence intensities, power density spectra and conditionally averaged vortices are determined.

A theoretical analysis is performed in Chapter 3. First, the mean flow is modeled using an analytical approach with a profile function for the transverse distribution of the mean streamwise velocity. A quasi one-dimensional model for the mean streamwise velocity is obtained. Second the development of the coherent structures is predicted by linear stability analysis. The results obtained with the proposed linear analysis, demonstrate a dependency of the large coherent structures on the perturbations at the inflow boundary.

This dependency is further investigated in Chapter 4, with the aid of numerical simulations, in which the large scale depth-averaged motion is resolved. Additional laboratory experiments are performed in which the inflow perturbations are varied. The dependency of the inflow perturbations was confirmed. A closer look at the origin of the perturbations was thus required. It was hypothesized that in reality the large scale components of the bottom turbulence served as perturbations.

The bottom turbulence is investigated in greater detail in Chapter 5, making use of a full three-dimensional Large Eddy Simulation. The results of this three-dimensional simulation are used to build a model for the depth-averaged motion in which bottom turbulence is mimicked by means of kinematic simulation.

In Chapter 6, the proposed model is applied to the mixing layer flow over a horizontal bed with uniform roughness. Additionally, a compound channel flow with lateral roughness variation is simulated.

A spin-off of Chapter 2 and 3 is presented in Appendix A, where a new momentum exchange model for straight uniform compound channel flow is proposed. Such a compound channel, consisting of a relatively deep main channel and a relatively shallow flood plain, is representative for low-land rivers.

Finally, in Chapter 7, conclusions will be drawn and the new insights will be discussed. This includes the applicability of the developed models as well as recommendations for further research.

Chapter 2

Laboratory experiments

Three different methodologies for studying shallow water flows are followed in this thesis: laboratory experiments, analytical modeling and numerical modeling. This chapter deals with the experimental approach. Although a number of experiments on shallow mixing layers have already been performed (Chu & Babarutsi, 1988; Tukker, 1997; Uijttewaal & Booij, 2000), new experiments were set up in which the measurement technique Particle Tracking Velocimetry (PTV) was used to determine the spatial structure of the flow. The objective of the experiments is twofold. The experimental results will be used on the one hand for understanding of the mechanisms that govern the energy and momentum balances of shallow water flows and on the other hand for validation of analytical and numerical modeling.

This chapter describes the experimental setup, the data analysis and some selected results. Part of the results regarding the mean flow and the spectral distribution of the turbulent kinetic energy will be presented in Chapter 3, where they are compared with an analytical model. A further comparison of numerical simulations with the measurements will be presented in Chapter 6.

2.1   The flume and flow conditions

Experiments were conducted in a shallow flow facility with a total length of 20m and a width of 3m, see Figure 2.1. This flow facility in the Fluid Mechanics Laboratory at Delft University of Technology is dedicated to shallow water experiments. It has already been used for experiments as described by Tukker (1997) and Uijttewaal & Booij (2000). The facility was designed for experiments with a turbulent and sub-critical flow, as is the case in lowland rivers. The Reynolds numbers $Re \equiv UD/\nu$ are sufficiently large ($Re > 4000$) and the Froude numbers $Fr \equiv U/\sqrt{gD}$ are smaller than about 0.5 to meet these requirements.

The inlet section of the facility is divided into two parts, each with a separate water supply. It has a vertical contraction that connects to the horizontal bottom of the flume. Screens are placed between the contraction and the entrance of the horizontal part to obtain a homogeneous inflow. Foam boards are mounted, floating just downstream of the screens to suppress free surface waves. In order to have a fully developed wall flow at the confluence of the two streams, the flows are initially separated by a 3m long thin splitter
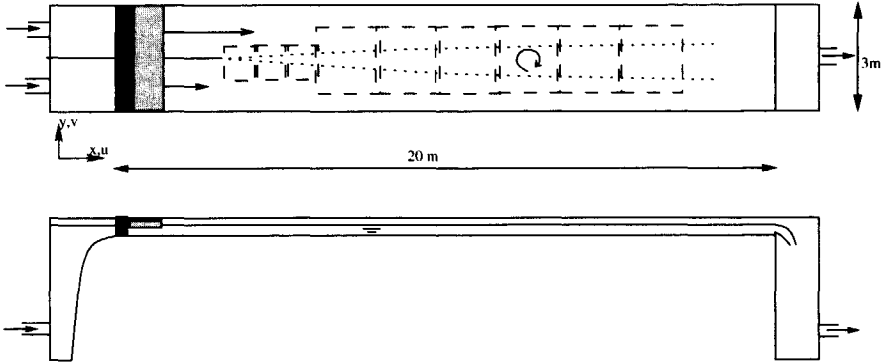
Figure 2.1: Top and side view of the shallow flow facility. The PTV measurements areas are indicated with the dashed squares.

Table 2.1: Flow conditions at the end of the splitter plate.

	D[mm]	U_1 [m/s]	U_2[m/s]	c_f[-]
Case 42	42	0.25	0.11	0.0032
Case 67	67	0.32	0.13	0.0027

plate. The horizontal bottom and the side walls of the flume consist of glass plates, assuring a smooth surface. A sharp crested weir regulates the outflow.

Two configurations are studied here, which are close to the cases studied by Uijttewaal & Booij (2000). The flow conditions at the end of the splitter plate are given in Table 2.1. These two configurations demonstrate the effect of the water depth on the evolution of coherent structures. Significant horizontal coherent structures were found in the case with the larger depth, whereas these were less dominant in the more shallow case, where bottom friction is supposed to play a more important role. The single point technique of Laser Doppler Anemometry (LDA) has been used by Uijttewaal & Booij (2000). In order to determine the spatial structure of the flow, Particle Tracking Velocimetry (PTV) is used in the present study, yielding time series of spatial velocity maps.

2.2 Experimental techniques

2.2.1 Flow visualization

In order to get a first impression of the flow in a developing shallow mixing layer, a bird's-eye view of a dye visualization is shown in Figure 2.2. Dye is injected downstream of the splitter plate and we look in downstream direction. Due to the continuous injection of dye, a dye band is created. This dye band rolls up, due to the large scale horizontal coherent

Figure 2.2: A bird's-eye view of a dye injection downstream of the splitter plate. The arrows indicate the magnitude and direction of the velocity.

structures. These coherent structures are predominantly horizontal and largely exceed the water depth. In addition to the rolling up of the dye-band, the dye is dispersed slightly, due to the effect of the small scale bottom turbulence.

2.2.2   Particle Tracking Velocimetry (PTV)

Particle Tracking Velocimetry is a straightforward and powerful measurement technique. The principle is based on tracking individual particles in the flow. The velocity of a particle is determined by recording its displacement during a certain time interval. With the increase of computational and storage capacity of computers, the paths of thousands of particles can be determined simultaneously, such that spatial information about the flow can be obtained with a high resolution.

In order to determine the flow field, floating polypropylene beads with a diameter of 2mm were distributed homogeneously on the water surface. As the particles are submerged for more than 90%, they are expected to follow the surface velocity. A distributor is used to spread the beads homogeneously on the water surface. This distributor was placed just upstream of the measurement area, so that the effect of particles moving out of vortex centers due to secondary circulations is reduced. A digital camera mounted on a bridge over the flume recorded the positions of the particles. The camera (Kodak ES1) has a resolution of 1008 × 1018 pixels with 256 gray levels and a frame rate of 30 Hz. Time series of images are stored directly on the hard disk of a PC to a maximum of 10,000 frames for a single continuous sequence. Measurements are performed for nine connected areas, covering the mixing layer over a length of 11m, as indicated in Figure 2.1. The first three
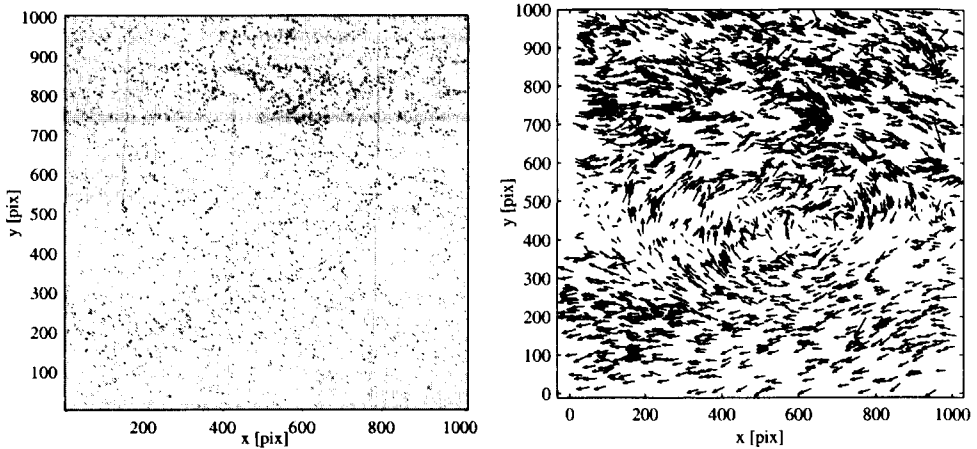
Figure 2.3: A typical image and an associated unstructured velocity map.

measurement planes have a dimension of 0.82m × 0.82m to obtain a sufficient resolution to resolve the relatively small coherent structures. The six areas further downstream have dimensions of 1.65m × 1.65m in order to capture the full mixing layer width.

The PTV-algorithm used here has been developed by Bastiaans *et al.* (2002) and consists of three steps. First, a sequence of images is recorded. Second, the particle positions are determined, based on the size, shape and contrast of the particles. Third, the trajectories of the particles are determined, which result in the velocities. The final result is a velocity field on an unstructured grid. Typically 2500 velocity vectors were detected per image. Figure 2.3 shows a typical image and an associated unstructured velocity field. For further analysis the vector fields are interpolated to a grid with 40 × 40 mesh points, using a cubic spline method. The mesh size is such that only the large scale motion is captured with this method. Turbulence with a typical length scale smaller than the water depth is not resolved.

2.3   Statistical analysis

The transverse profiles of the time-averaged streamwise velocity U are plotted in the figures 2.4a and 2.5a for the Cases 42 and 67. The profiles have a self-similar character, although there are some deviations on the high velocity side of the mixing layer. The characteristics of a shallow mixing layer as mentioned for example in Chu&Babarutsi (1988) are found in these profiles: (1) the velocity difference is decreasing; (2) the growth rate of the mixing layer width is decreasing; and (3) the center of the mixing layer is shifting to the low velocity side. These differences are discussed in detail in Chapter 3, in which an analytical model for the mean streamwise velocity is proposed.

In principle the turbulence intensities contain the contributions of the full frequency range of turbulent fluctuations. This range is limited on the low frequency side by the measurement duration and on the high frequency side by the sampling frequency. In this study emphasis is put on measuring the large scale fluctuations. The large scale surface velocity fluctuations are assumed to be similar to the large scale depth-averaged fluctuations. The fluctuations are split into a large scale part u' and a small scale part u''. The measured turbulent intensities can then be written as:

$$u(t) - U = u'(t) + u''(t)$$

The large scale motion can be resolved by the measurements. The small scale motion is not properly measured, since only the surface velocity is measured and the spatial resolution is limited by the distance between the particles. The small scale motion is effectively filtered out by applying a low pass cosine filter with a timescale τ, see Emery&Thomson (1997). Since it is not the aim to measure the three-dimensional bottom turbulence, coherent structures with a length scale smaller than two times the water depth are filtered out. The corresponding time scale is determined by using the mean streamwise velocity in the center of the mixing layer:

$$\tau = \frac{2D}{U_c}$$

The filtered turbulence intensities u', v' and the corresponding Reynolds stress $-\overline{u'v'}$ are plotted in the figures 2.4b-d and 2.5b-d. A clear peak develops in downstream direction with a width scaling with the width of the mixing layer. As a consequence of the transverse gradient of the streamwise velocity, instabilities can grow and form large-scale coherent flow structures. However, the instabilities will be dissipated due to the bottom shear stress and due to small scale turbulence, acting effectively as a turbulent viscosity. At a certain position downstream the dissipative influence of the bottom friction will be stronger than the production of kinetic energy by the transverse shear, such that the large scale turbulent kinetic energy decreases. The position where the dissipation becomes stronger than the production is reached at a location more upstream for Case 42 than for Case 67 as the bottom friction is more significant for Case 42. The peak values in the turbulence intensities are growing for almost the full length of the flume for Case 67, whereas the peak value decreases already after about one meter downstream of the splitter plate for Case 42. A detailed description and quantification of the balance between production and dissipation of kinetic energy will be given in Chapter 3. It should be noted that the low peak value close to the splitter plate is a result of the low-pass filtering. At this position, the horizontal motion has a length scale smaller than the water depth.

On the high velocity side of the mixing layer of Case 67, slight negative values are found for the Reynolds stresses. These are consistent with slightly negative transverse gradients of the mean streamwise velocity (Figure 2.5a). Slight negative values are also found in the mixing layer experiments of Uijttewaal&Booij (2000) and the compound channel experiments of Knight&Shiono (1990). No sound explanation has been found for this phenomenon.

Figure 2.4: Transverse profiles of the mean streamwise velocity U (a), the turbulence intensities u' (b), v' (c) and the Reynolds stress $-\overline{u'v'}$ (d) for Case 42.
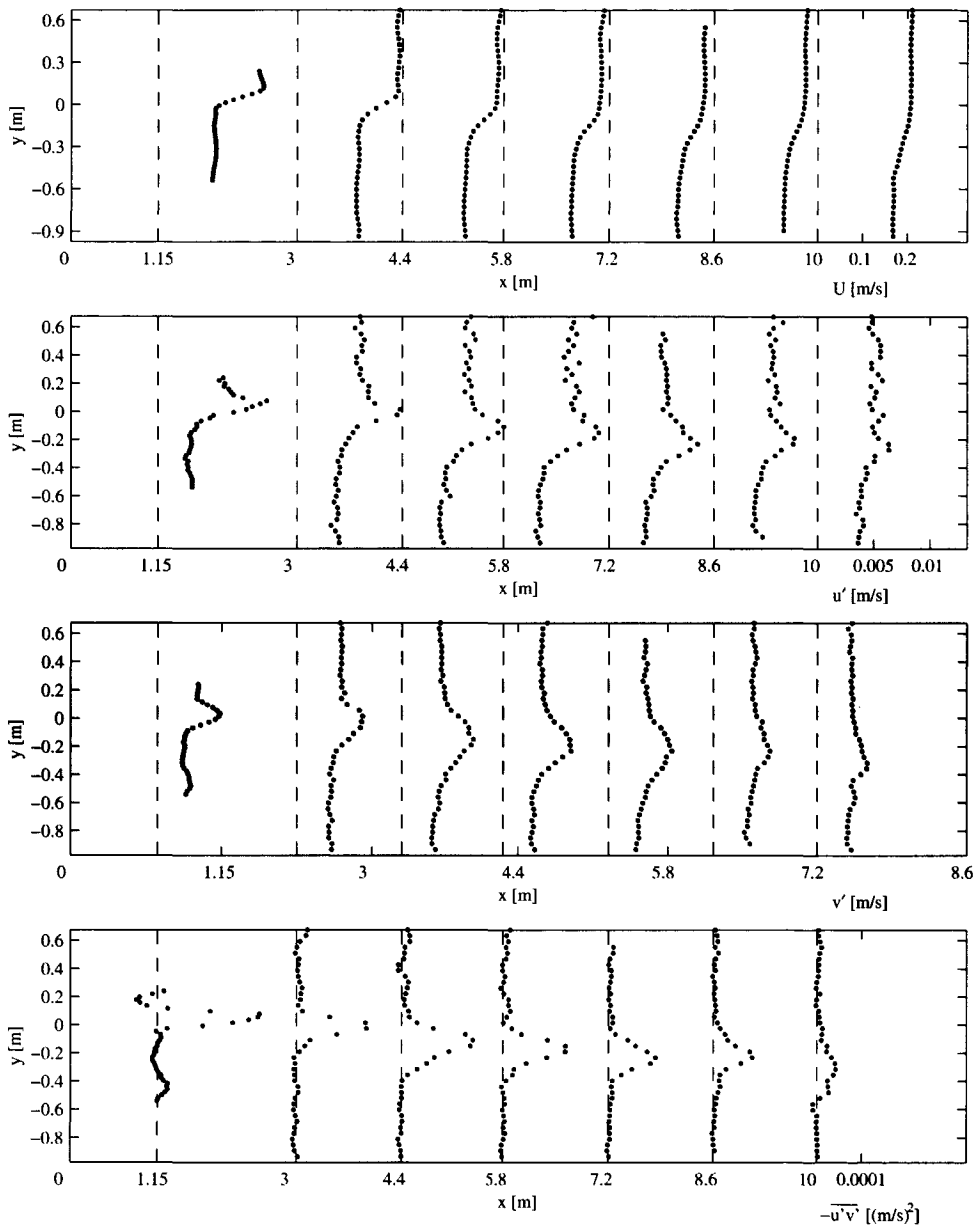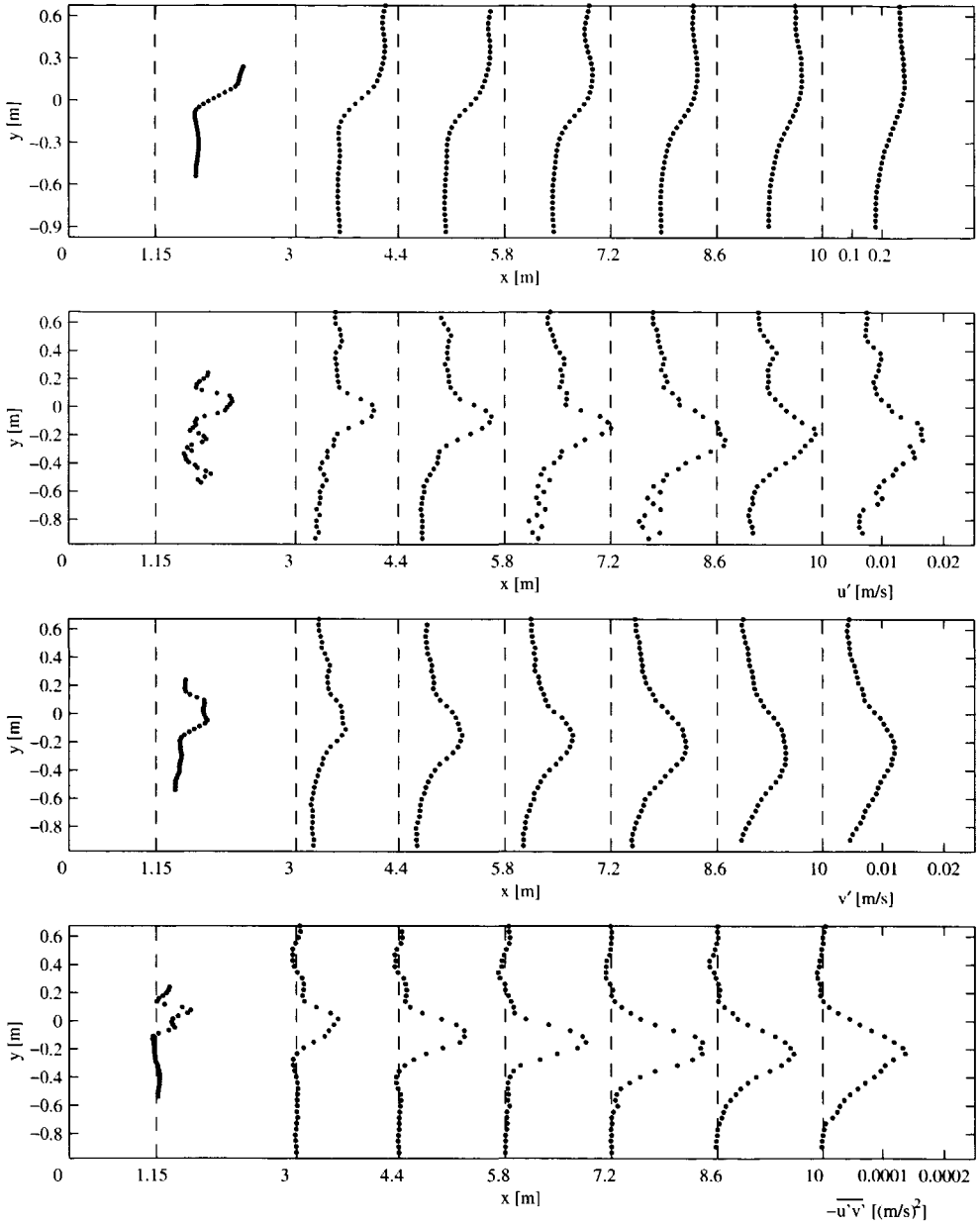
Figure 2.5: Transverse profiles of the mean streamwise velocity U (a), the turbulence intensities u' (b), v' (c) and the Reynolds stress $-\overline{u'v'}$ (d) for Case 67.

2.4   Spectral analysis

Power density spectra are determined to reveal the energy distribution over the different time scales. These spectra are obtained from timeseries in the center of the mixing layer. In order to smooth the spectra, the timeseries are divided in 15 half-overlapping segments, which are multiplied by a Kaiser filter. The Fast Fourier Transformation is carried out and the average of the 15 spectra determines the final spectrum. A detailed description of this method is given in Emery & Thomson (1997).

The energy density spectra for the transverse velocity fluctuations E_{vv} of Case 42 and Case 67 are plotted in Figure 2.6 for different positions downstream. In the spectra of Case 67, a profound peak is developing. This peak is associated with the presence of horizontal coherent structures. Moving in downstream direction, the frequency of the peak decreases, corresponding to an enlargement of the coherent structures. The magnitude of the peak increases, implying that the coherent structures grow in intensity. The energy density spectra of Case 42 show a different development in downstream direction. A peak is moving to the low frequency range. Coherent structures are present and grow in size. However, the magnitude of the peak is decreasing after about $x = 4$m. Apparently the coherent structures decay from this position on. The development of the coherent structures is supposed to be dependent on the production of large scale kinetic energy by the mean shear and the dissipation by the bottom friction and the small scale turbulence. In Case 67 the production dominates over the full length of the measured area. For Case 42 the production initially dominates, but due to the decrease of the velocity difference and the increase of the mixing layer width, the production reaches values smaller than the dissipation, leading to an effective dissipation. A quantitative analysis of the development of the energy density spectra is given in Chapter 3.

The slope on the high frequency side of the peak is close to -3. Such a slope is found in many shallow water flow experiments (Dracos *et al.*, 1992; Chen & Jirka, 1999; Uijttewaal & Booij, 2000) and is often associated with two-dimensional turbulence as derived by Batchelor (1969) and Kraichnan (1967). It is however questionable whether this derivation is valid for the flow considered here since it contains a strong horizontal velocity gradient and bottom turbulence.

The energy density spectra for the different components of the fluctuations are plotted in Figure 2.7. The peak is more pronounced in the E_{vv}-spectra than in the E_{uu}-spectra, although the peak value is larger for the streamwise velocity fluctuations. A smaller dominant peak frequency is found for the spectra of the streamwise fluctuations than for the spectra of the transverse fluctuations.

It is not unambiguous to translate the energy density spectra into characteristics of the coherent structures. However, these structures leave their footprints in the spectra, so that at least some characteristics of the coherent structures can be inferred. These footprints are discussed below.

A wider peak and lower peak frequencies are found for the spectra of the streamwise fluctuations than for the spectra of the transverse fluctuations. This can be explained by the the passing of vortices at different transverse positions. In order to explain this effect, a
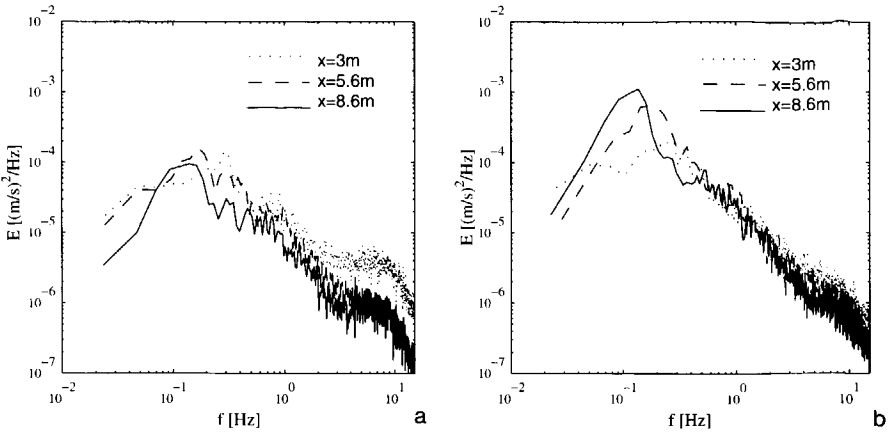
Figure 2.6: Energy density spectra of the transverse velocity at the positions x=3m, x=5.8m, x=8.6m for Case 42 (a) and Case 67 (b).
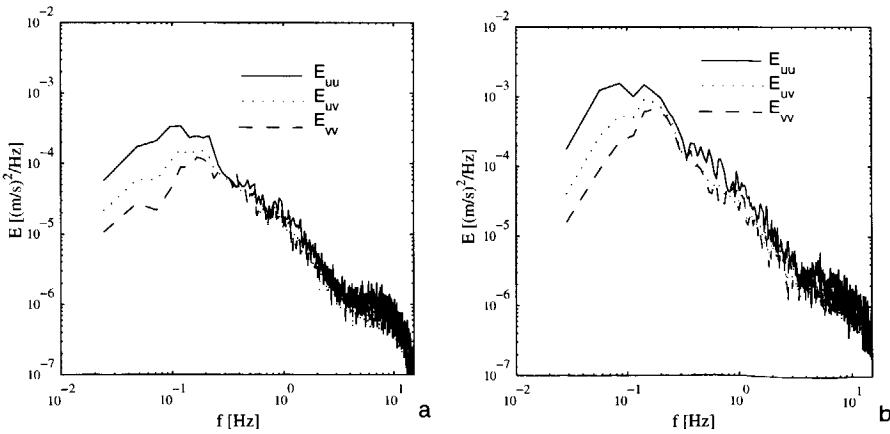
Figure 2.7: Energy density spectra of the streamwise velocity, the transverse velocity and the cross spectra at x=5.8m for Case 42 (a) and Case 67 (b).
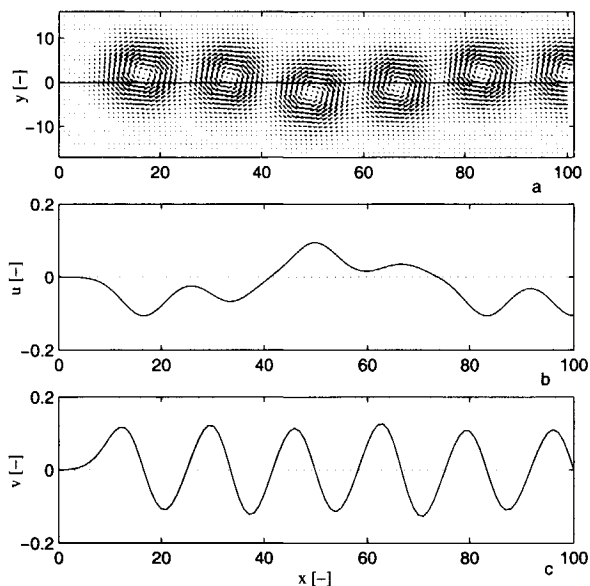
Figure 2.8: Artificial sequence of vortices with transverse displacements of the vortex centers. (a) velocity field, (b) streamwise velocity at $y = 0$, (c) transverse velocity at $y = 0$.

synthetic signal is created by a sequence of idealized vortices which are randomly displaced in transverse direction. Figure 2.8a shows the vector field of such a sequence of vortices. The minimum and the maximum values of the transverse velocity are found around $y = 0$ (see already Figure 2.10c for the contours of the transverse velocity of an idealized vortex). The streamwise gradients of the transverse velocity are significantly higher than the transverse gradients of the transverse velocity. A slight transverse displacement of the vortices results in only small effects on the transverse velocity signal, see Figure 2.8c. The minima and maxima of the streamwise velocity for each vortex have more or less the same downstream position (see already Figure 2.10b). The transverse gradient of the streamwise velocity is therefore higher than the streamwise gradient for this component. Slight transverse displacements of the vortex centers have great consequences for the timeseries at $y = 0$ (Figure 2.8b). From the timeseries, it obviously follows that the streamwise velocity fluctuations will have a lower dominant frequency than the transverse fluctuations. The regular oscillation of the transverse velocity will result in a narrower peak in the spectrum of the transverse fluctuations than in the spectrum of the streamwise velocity component.

The energy density level of the streamwise fluctuations is generally higher than the level of the transverse fluctuations. An explanation can be found in a possible elongation of the vortices. In Figure 2.9, a schematized representation of a vortex elongation is shown. In case of elongated vortices, the streamlines diverge in streamwise direction and converge in transverse direction. As continuity has to be obeyed, the intensity of the
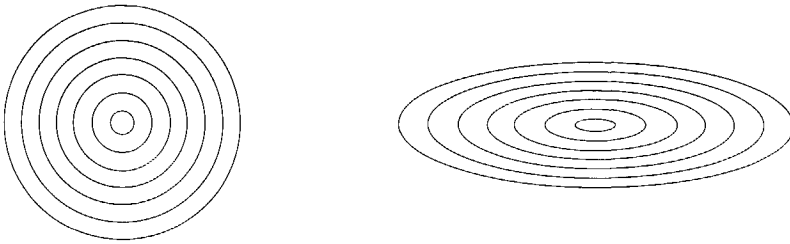
Figure 2.9: Streamlines of an idealized isotropic (left) and elongated (right) vortex.

streamwise fluctuations becomes higher and the intensity of the transverse fluctuations lower. A higher energy density level of the streamwise fluctuations could therefore be explained by elongation of the coherent structures in streamwise direction.

2.5 Coherent structures

The large coherent structures have their footprints in the power density spectra, but as discussed above, these spectra are insufficient for the determination of the characteristics of the coherent structures themselves. The instantaneous velocity maps obtained by PTV allow for the determination of the spatial distribution of the coherent motion. The eduction of coherent structures from velocity maps is a difficult task. Various methods for the identification of coherent structures are discussed in Bonnet *et al.* (1998). These are for example based on vorticity, a Weiss-function, wavelets, or pattern recognition techniques. Typical for applications to a mixing layer is the combination of a shear layer and coherent structures. This combination excludes the use of vorticity based methods, as the shear itself contains vorticity, regardless of the presence of eddy structures.

In order to identify coherent structures in a velocity map, we make use of a pattern recognition technique which is heavily based on the method of Scarano *et al.* (1999). This method has the advantage that the velocities are used instead of the velocity gradients as is the case in a method based on the Weiss function, for example. The pattern recognition method is based on the correlation between a predefined velocity pattern, a mask eddy, and the instantaneous velocity map at a certain time.

The method consists of the following iteration procedure. First, an initial velocity pattern, a mask eddy, centered at $x = 0$, $y = 0$ is chosen as

$$\hat{u} = \frac{y}{L} \exp(-\frac{x^2 + y^2}{L^2})$$

$$\hat{v} = -\frac{x}{L} \exp(-\frac{x^2 + y^2}{L^2})$$

with L the length scale of the eddy. The contours of the velocity fields are plotted in figure 2.10. The length scale L has to be chosen in the order of the size of the expected coherent
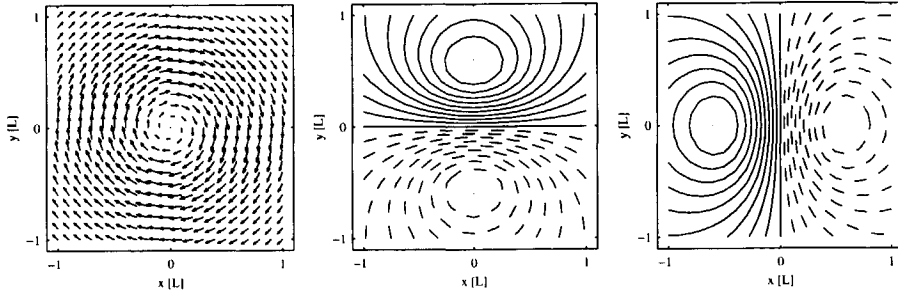
Figure 2.10: The velocity vectors (a), streamwise velocity contours (b) and transverse velocity contour (c) of the mask eddy.

structures. As will be shown below, the whole pattern recognition procedure contains a few iteration steps in which the mask eddy is redefined. The precise size and shape of the initial mask eddy therefore turned out to be of minor importance.

Second, the cross-covariance between the streamwise and transverse component of the mask eddy and the velocity map is determined at different transverse position for a downstream position x_i:

$$C_u(x_i, y_j, t) = \frac{1}{4L^2} \int_{x_i-L}^{x_i+L} \int_{y_j-L}^{y_j+L} \hat{u}(x,y) \cdot u(x,y,t) \mathrm{d}y \mathrm{d}x$$

$$C_v(x_i, y_j, t) = \frac{1}{4L^2} \int_{x_i-L}^{x_i+L} \int_{y_j-L}^{y_j+L} \hat{v}(x,y) \cdot v(x,y,t) \mathrm{d}y \mathrm{d}x$$

As an example, the cross-covariance functions obtained from a sequence at $x = 8.6$m are plotted in Figure 2.11a-b. The gradients in transverse direction are largest for the streamwise component and the gradients in streamwise direction are largest for the transverse component. Therefore, the transverse velocity covariance is most suitable for the determination of the streamwise position of an eddy and the streamwise co-variance for the transverse position. In the method of Scarano et al. (1999) not only the streamwise and transverse velocity components, but also the components at 45° and 135° are used. It turned out that these components were not needed here. Third, the cross-covariance functions of the streamwise and transverse correlations are multiplied:

$$C_u C_v(x, y, t) = C_u(x, y, t) \cdot C_v(x, y, t)$$

Here, the method differs again from the eduction method described by Scarano *et al.* (1999), in which the correlation functions are summed. Multiplication results in more significant peaks at the positions of the vortex centers. Additionally, the cross-covariance functions are used instead of the cross-correlation functions, in order to account for the intensity of the vortices, as we aim at identifying the energy containing vortices.
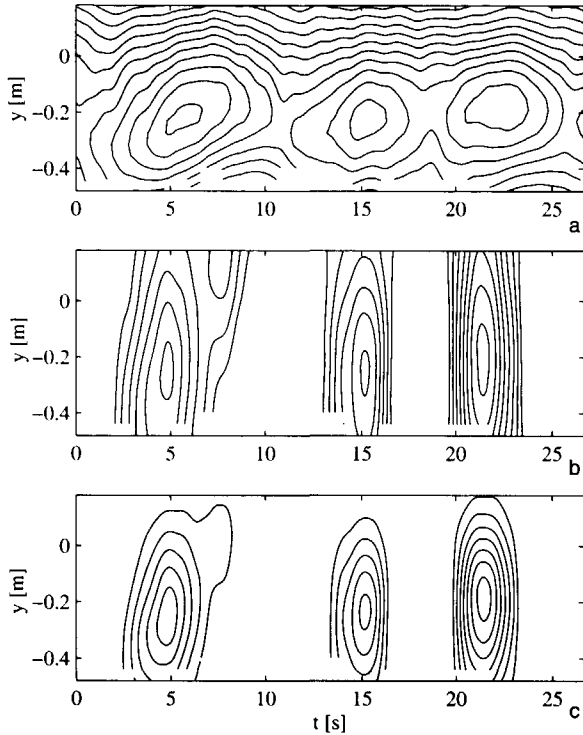
Figure 2.11: The contours of a part of the timeseries of the positive values of the covariance functions C_u (a), C_v (b) and the product C_uC_v (c) at $x = 8.6$m.

Contours of the covariance product $C_uC_v(x,y,t)$ at $x = 8.6$m as function of time t and transverse position y are plotted in figure 2.11c. A maximum in the covariance function $C_uC_v(x_i, y, t)$ indicates the transverse position of the center of an eddy at a certain time. In order to determine the conditionally averaged eddy, the times at which the covariance attains a maximum are selected. The velocity maps at these times are averaged, resulting in what is called here a conditionally averaged eddy. A correction is made for the transverse positions of the vortices. The vortices are aligned to the center of the mixing layer. Without this correction the conditionally averaged vortex would be smeared out. The averaged velocity map thus obtained is subsequently used as the new mask eddy, and the whole procedure is repeated a few times until the conditionally averaged velocity maps are not changing anymore. The conditionally averaged velocity field for a certain position downstream is then determined and can be used for the determination of the characteristics of the coherent structures.

The conditionally averaged vortices have been determined at two different positions downstream for Case 67 in accordance with the above described procedure. The coherent structures in Case 42 turned out to be too weak to apply the pattern recognition procedure. The vector fields (relative to the mean velocities), transverse velocity contours (relative to the mean transverse velocity), vorticity contours and the Weiss-function contours are shown in the figures 2.12 and 2.13. The Weiss function is defined as the difference between the squared shear and the squared vorticity:

$$Q = S^2 - \omega^2 = \left(\frac{\partial u}{\partial x} - \frac{\partial v}{\partial y}\right)^2 + \left(\frac{\partial v}{\partial x} + \frac{\partial u}{\partial y}\right)^2 - \left(\frac{\partial v}{\partial x} - \frac{\partial u}{\partial y}\right)^2$$

A negative value indicates dominance of rotation. A vortex can then be defined as the area within a zero contour of the Weiss function. The following properties of the coherent structures can be identified from the figures 2.12 and 2.13. The vortices are elongated in streamwise direction. This already follows from the vector fields, but it is better visible in the Weiss function and vorticity. The zero contour of the Weiss function indicates the edge of a vortical structure. In these cases the zero contour is however a bit contaminated due noise.

The length scale of the vortices can be determined proportional to the distance between the minimum and the maximum value in the transverse velocity map. Here we define the length scale L as twice this distance. This length scale can be compared with the length scale associated with the peak in the energy density spectra. The length scales found by the coherent structure eduction method $L_{eduction}(x = 3.0) = 0.9$m and $L_{eduction}(x = 8.6) = 1.8$m are in good agreement with the length scales are obtained from the spectra: $L_{spectra}(x = 3.0) = 0.8$m and $L_{spectra}(x = 8.6) = 1.7$m.

Figure 2.12c shows a strong mean shear at the position in the near field, $x = 3.0$m. The contribution to the total vorticity of the mean shear is much larger than the contribution of the vortex structures. For both cases, the maximum vorticity is not in the center of the eddy, but slightly upstream. This is explained by the decreasing mean shear in downstream direction, caused by the widening of the mixing layer and the decreasing velocity difference over the mixing layer. The maximum vorticity at the downstream position $x = 8.6$m is much higher than the background shear. This indicates that the coherent structures become relatively more important further downstream.

2.6   Summary and conclusions

The PTV measurements have resulted in an extensive dataset, containing spatial and temporal information. Various analysis methods are applied, showing the presence and the development of horizontal coherent structures. A significant difference is found between the two measured cases with different depths. Such a difference was also found by Uijttewaal&Booij (2000). This difference is ascribed to the stronger influence of the bottom turbulence in Case 42. The balance between the production and dissipation of the coherent structures needs further investigation, as will be done in the next chapter.

The advantage of the use of PTV is that spatial information is obtained. In contrast with single point measurements, coherent structures are measured directly. A disadvantage is that only the surface velocity is measured with a limited frequency of 30Hz and a finite duration of 5 minutes. However, this surface velocity is sufficient for the determination of the large scale horizontal motion. The detection of the vortices is done by the use of pattern recognition. Conditionally averaged vortices are determined, of which characteristics like the size, intensity and shape are determined. These characteristics will be used lateron in Chapter 6 for a comparison with numerical simulations.
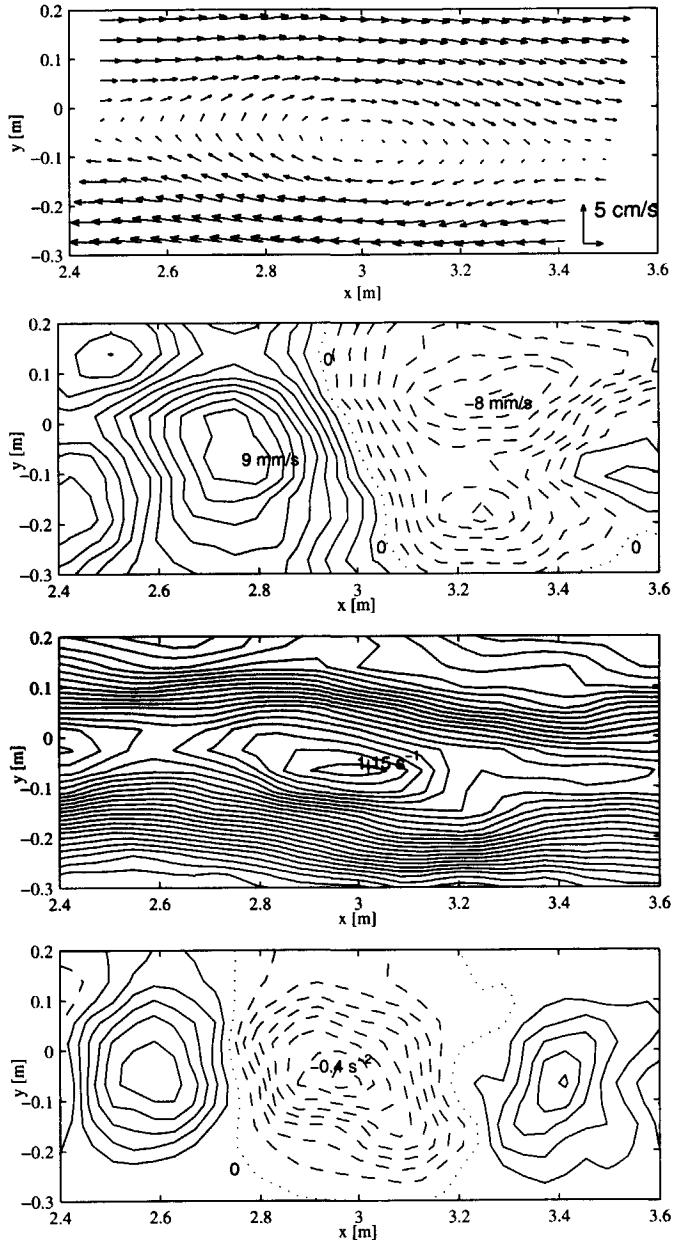
Figure 2.12: Properties of the measured conditionally averaged vortex centered at $x = 3.0$m. (a) velocity vectors relative to the mean advection velocities, (b) transverse velocity ($\Delta v = 1$mm/s), (c) vorticity ($\Delta \omega = 0.05$s^{-1}) and (d) Weiss-function ($\Delta Q = 0.05$s^{-2}). Negative values are indicated with a dashed line, positive values with a solid line and zero contours with a dotted line.

Figure 2.13: Properties of the measured conditionally averaged vortex centered at $x = 8.6$m. (a) velocity vectors relative to the mean advection velocities, (b) transverse velocity ($\Delta v = 1$mm/s), (c) vorticity ($\Delta \omega = 0.05$s^{-1}) and (d) Weiss-function ($\Delta Q = 0.03$s^{-2}). Negative values are indicated with a dashed line, positive values with a solid line and zero contours with a dotted line.
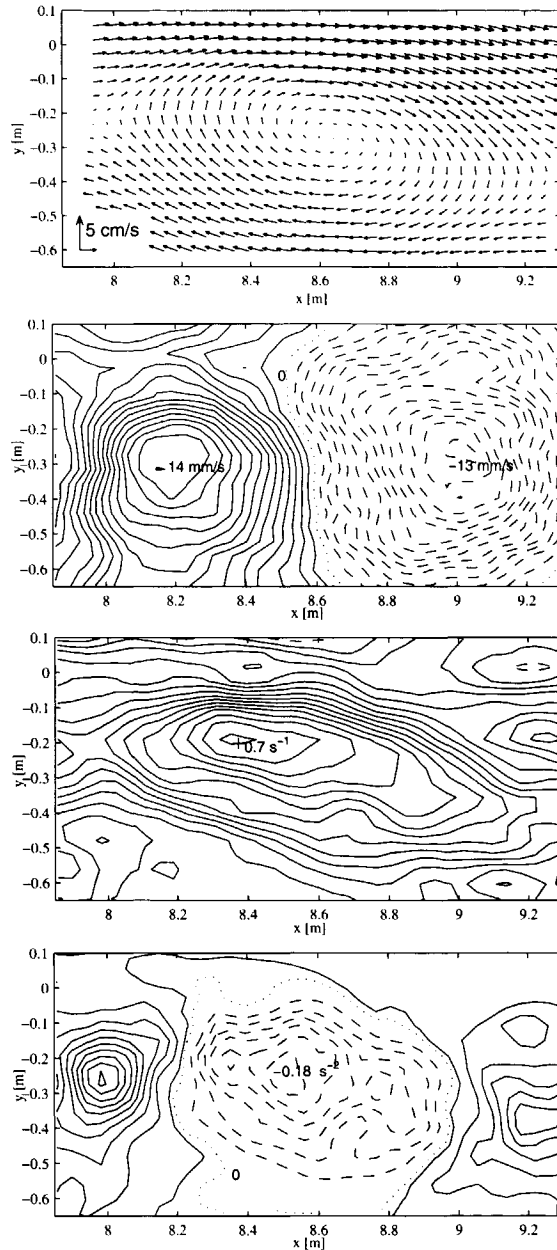
Chapter 3

Theoretical analysis

In this chapter, shallow mixing layers are investigated via an analytical approach. In such an approach the equations of motion are reduced to simple expressions. This has two advantages: (1) the dominant physical mechanisms determining the flow are made clear and (2) the model can be used for a quick prediction of idealized flow types. The disadvantage is however that complex flows cannot be investigated. First, the governing shallow water equations are given in Section 3.1. The development in downstream direction of the mean flow field of a developing mixing layer is described in Section 3.2 by a quasi one-dimensional model, based on self-similarity of the velocity profiles. In Section 3.3, the development of the properties of the large scale motion in this developing mixing layer is determined by linear stability analysis, using the calculated mean flow field as base flow. The results are validated by experimental data as described in the preceding chapter. The results are discussed and conclusions are drawn in Section 3.4. The analysis as described in this chapter is published in Van Prooijen&Uijttewaal (2002a).

3.1 Shallow water equations

The shallow water equations form the basis of the modeling of the mean flow field and the linear stability analysis. As the horizontal length scales are significantly larger than the water depth, the flow is described by the two-dimensional shallow water equations (De Saint Venant equations). As the Froude numbers are small, a rigid lid is imposed at the water surface (Ghidaoui & Kolyshkin, 1999). The continuity equation and the momentum equations in the horizontal plane are averaged over the water depth and averaged over a period larger than the time scale of the three-dimensional bottom turbulence, but smaller than the time scale of the large scale motion, resulting in:

$$\frac{\partial D\tilde{u}}{\partial x} + \frac{\partial D\tilde{v}}{\partial y} = 0 \tag{3.1}$$

$$\frac{\partial \tilde{u}}{\partial t} + \tilde{u}\frac{\partial \tilde{u}}{\partial x} + \tilde{v}\frac{\partial \tilde{u}}{\partial y} = -\frac{1}{\rho}\frac{\partial \tilde{p}}{\partial x} - \frac{c_f}{D}\tilde{u}\sqrt{\tilde{u}^2 + \tilde{v}^2} + \nu_t\nabla^2\tilde{u} \tag{3.2}$$

$$\frac{\partial \tilde{v}}{\partial t} + \tilde{u}\frac{\partial \tilde{v}}{\partial x} + \tilde{v}\frac{\partial \tilde{v}}{\partial y} = -\frac{1}{\rho}\frac{\partial \tilde{p}}{\partial y} - \frac{c_f}{D}\tilde{v}\sqrt{\tilde{u}^2 + \tilde{v}^2} + \nu_t\nabla^2\tilde{v} \tag{3.3}$$

where u is the velocity in streamwise direction x, v the velocity in lateral direction y of the horizontal plane and D the water depth. The depth-and-short-time-average operator is denoted by a tilde $\tilde{\ }$. Capitals will be used to denote the long-time-average operator. The bed friction coefficient c_f for turbulent flow over a smooth bottom is determined by the relation:

$$\frac{1}{\sqrt{c_f}} = \frac{1}{\kappa} \left[\ln \left(Re\sqrt{c_f} \right) + 1 \right] \tag{3.4}$$

in which $Re (= UD/\nu)$ denotes the depth-based Reynolds number. Since it is our aim to resolve the large scale coherent motion, the small scale turbulent fluctuations, produced in the bottom boundary layer, are to be modeled by an effective eddy viscosity ν_t, see also Chen&Jirka (1998). The small scale bottom turbulence is estimated here by using a simple expression for the turbulence eddy viscosity, see for example Fisher *et al.* (1979):

$$\nu_t = 0.15 D u_* = 0.15 D \sqrt{c_f} U \tag{3.5}$$

This definition differs from the approach of Alavian&Chu (1985) who used an eddy viscosity based on the large scale motion, using the mixing layer width and the velocity difference across the mixing layer, which resulted in a higher eddy viscosity.

3.2 Mean flow field

In order to determine the base flow for the stability analysis, an analytical model is formulated to predict the mean streamwise velocity field. This model is based on the assumption of self-similarity. An overview of the possibilities of the application of the self-similarity concept is given in Townsend (1976). In a self-similar flow the lateral profiles of the streamwise velocity and the Reynolds stress can be described by a shape function, which is made dimensional with a typical length scale and velocity scale which may vary in downstream direction. Self-similar profiles are found for unbounded mixing layers (Townsend, 1976; Lesieur, 1997), but also for shallow mixing layers, according to the experiments described in this thesis and the experiments of Chu&Babarutsi (1988) and Uijttewaal&Booij (2000). Characteristic properties of the shallow mixing layer are: the downstream decrease of the velocity difference, the decreasing growth rate of the mixing layer width and the shift of the center of the mixing layer to the low velocity side. A model for the mean flow field should be able to capture all these properties.

3.2.1 Self-similarity

The flow outside the mixing layer is not influenced by the mixing layer. The mean streamwise velocity on the high and low velocity side are denoted with U_1 and U_2, respectively. The flow outside the mixing layer defines the mean velocity difference over the mixing layer ($\Delta U = U_1 - U_2$) and the mean velocity in the center of the mixing layer ($U_c = (U_1 + U_2)/2$). The width of the mixing layer (δ) is defined here as the ratio of the velocity difference ΔU
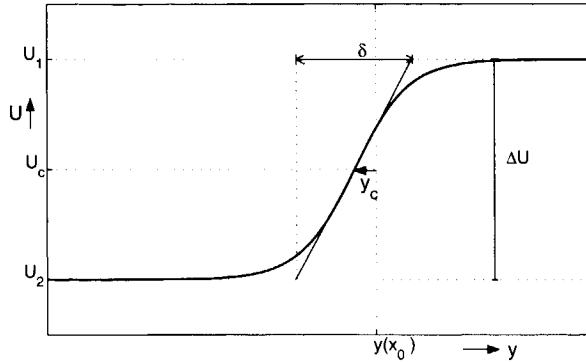
Figure 3.1: Sketch of the lateral profile of the streamwise velocity, according to Equation 3.7

to the lateral gradient of the velocity in the center $\left(\frac{\partial U}{\partial y}_c\right)$:

$$\delta = \frac{\Delta U}{\frac{\partial U}{\partial y}_c} \tag{3.6}$$

Self-similarity implies that the transverse profiles of the streamwise velocity can be described by a profile function. A variety of functions can be considered, e.g. the error function or the hyperbolic tangent. We use the hyperbolic tangent (tanh), because it fits the data well. The exact shape turned out to affect the results of this analysis only weakly. The mean flow field is then approximated by (see the sketch in figure 3.1):

$$U(x,y) = U_c(x) + \frac{\Delta U(x)}{2} \tanh\left(\frac{y - y_c(x)}{\frac{1}{2}\delta(x)}\right) \tag{3.7}$$

By using a profile function, the two-dimensional formulation is reduced to a formulation depending on the downstream position (x) only. The downstream development of the velocity difference ΔU, the velocity in the center of the mixing layer U_c, the transverse position of the center of the mixing layer y_c, and the mixing layer width δ will be specified below.

3.2.2 Mean velocity in the center of the mixing layer

The velocity in the center of the mixing layer is approximated by a constant, U_c. This assumption is justified by using the incompressibility condition. The discharge at the inlet section should be equal to the discharge far downstream:

$$U_1(x_0)\frac{DW}{2} + U_2(x_0)\frac{DW}{2} = U_\infty DW, \tag{3.8}$$

with W the width of the flow domain, D the constant water depth, $U_1(x_0)$ and $U_2(x_0)$ the initial streamwise velocities outside the mixing layer and U_∞ the uniform velocity far

downstream. This leads to $U_\infty = \frac{U_1(x_0) + U_2(x_0)}{2} = U_c$. In the experiments, U_c shows a slight increase ($< 3\%$) in downstream distance due to the free-surface slope as a result of bed friction and the horizontal bottom.

3.2.3 Velocity difference over the mixing layer

The velocities outside the mixing layer are not influenced by the mixing layer. These flows can be considered to be one-dimensional. The development of the velocity difference $\Delta U(x)$ is then determined by the momentum equation in streamwise direction (Equation 3.2) for the high velocity side, denoted by the index 1 and the low velocity side denoted by the index 2 (Chu & Babarutsi, 1988):

$$\frac{1}{2}\frac{dU_1^2}{dx} + \frac{c_{f_1}}{D}U_1^2 + \frac{1}{\rho}\frac{dP_1}{dx} = 0 \tag{3.9}$$

$$\frac{1}{2}\frac{dU_2^2}{dx} + \frac{c_{f_2}}{D}U_2^2 + \frac{1}{\rho}\frac{dP_2}{dx} = 0 \tag{3.10}$$

The streamwise gradient of the pressure is the same for both sides as demonstrated in previous experiments (Uijttewaal & Booij, 2000). After subtraction of 3.10 from 3.9 and using a constant U_c, the velocity difference $\Delta U(x)$ is expressed, following Chu&Babarutsi (1988), as:

$$\Delta U(x) = \Delta U_0 \exp\left(-\frac{2c_f}{D}x\right), \tag{3.11}$$

where ΔU_0 denotes the velocity difference at the inflow. The predicted exponential decrease of the velocity difference is in good agreement with the measurements as shown in figure 3.2.

3.2.4 Mixing layer width

The lateral distribution of the flow properties in plane shear flows is assumed to be self-similar (Townsend, 1976; Uijttewaal & Booij, 2000). This means that the flow quantities can be described by shape functions. The parameters of the shape functions are only dependent on the downstream position x. It was already mentioned that the mean velocity profile can be approximated by a hyperbolic tangent. Substituting the shape functions into the steady streamwise momentum equation gives:

$$(U_c + \Delta U f_1)\frac{d\Delta U f_1}{dx} = -\frac{1}{\rho}\frac{dP}{dx} - \frac{c_f}{D}(U_c + \Delta U f_1)^2 - \frac{1}{\delta}\frac{dq_0^2 f_2}{d\eta}$$

with

$$U = U_c + \frac{1}{2}\Delta U f_1(\eta)$$
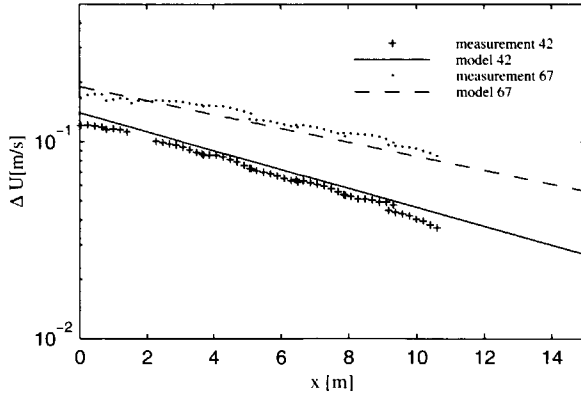
$$\overline{uv} = q_0^2 f_2(\eta)$$

Figure 3.2: Development of the velocity difference $\Delta U(x)$ in streamwise direction for the Cases 42 and 67 according to the measurements and the model, Equation 3.11.

with $\eta = \frac{y-y_c}{\delta}$ and shape functions f. The pressure gradient term equals the bottom friction term in the center of the mixing layer, so that the streamwise momentum can be rewritten into

$$\left(U_c + \frac{1}{2}\Delta U f_1 \right) \frac{\mathrm{d}\frac{1}{2}\Delta U f_1}{\mathrm{d}x} = -\frac{c_f}{D}\left(\left(\frac{1}{2}\Delta U f_1 \right)^2 + U_c \Delta U f_1 \right) - \frac{1}{\delta}\frac{\mathrm{d}q_0^2 f_2}{\mathrm{d}\eta}$$

A new length scale, the frictional length scale of the flow, is defined by $L = \frac{D}{c_f}$, which is much larger than the water depth and even the mixing layer width ($D \ll \delta \ll L$). As follows from Equation 3.11, the streamwise gradient of the velocity difference can be written as:

$$\frac{\mathrm{d}\Delta U}{\mathrm{d}x} = -\frac{2c_f}{D}\Delta U \tag{3.12}$$

Substitution of the length scale L and Equation 3.12 in the streamwise momentum equation leads to

$$\left(U_c + \frac{1}{2}\Delta U f_1 \right)\left(-\frac{1}{L}\Delta U f_1 + \frac{\Delta U}{2\delta}\frac{\mathrm{d}\delta}{\mathrm{d}x}f_1' \right) = -\frac{1}{L}\left(\left(\frac{1}{2}\Delta U f_1 \right)^2 + U_c \Delta U f_1 \right) - \frac{q_0^2}{\delta}f_2'$$

This equation is finally made dimensionless by multiplying it with $\frac{\delta}{\Delta U^2}$:

$$\frac{U_c}{2\Delta U}\frac{\mathrm{d}\delta}{\mathrm{d}x}f_1' - \frac{\delta}{2L}f_1^2 + \frac{1}{4}\frac{\mathrm{d}\delta}{\mathrm{d}x}f_1 f_1' + \frac{\delta}{4L}f_1 f_1 + \frac{q_0^2}{\Delta U^2}f_2' = 0 \tag{3.13}$$

The momentum equation now consists of a set of shape functions which are varying with the lateral coordinate η and quantities varying with the streamwise coordinate x. Equation

3.13 can therefore only be valid if the factors

$$\frac{U_c}{2\Delta U}\frac{\mathrm{d}\delta}{\mathrm{d}x} \qquad \frac{\delta}{2L} \qquad \frac{1}{4}\frac{\mathrm{d}\delta}{\mathrm{d}x} \qquad \frac{\delta}{4L} \qquad \frac{q_0^2}{\Delta U^2} \tag{3.14}$$

are constant or negligible. As mentioned above, the mixing layer width is generally an order of magnitude smaller than the development length of the flow, $\frac{\delta}{L} \ll 1$, so that the second and fourth terms can be neglected. The last term refers to the mixing and is not zero and should therefore be constant. Two conditions remain which can imply self similarity: $\frac{U_c}{\Delta U} =$constant and/or $\frac{2U_c}{\Delta U} \gg 1$. If these conditions are fulfilled, the flow is self-similar. However, the first condition nor the second condition is automatically fulfilled for a shallow mixing layer. Generally $\frac{2U_c}{\Delta U} > 1$, especially in the far field, so that we continue with the assumption of self-similarity, based on $\frac{2U_c}{\Delta U} \gg 1$ and $\frac{U_c}{2\Delta U}\frac{\mathrm{d}\delta}{\mathrm{d}x} =$ constant. From the latter condition, the development of the mixing layer width can be derived:

$$\frac{\mathrm{d}\delta}{\mathrm{d}x} = \alpha\frac{\Delta U(x)}{U_c} \tag{3.15}$$

The entrainment coefficient α has an empirically determined value of $\alpha \simeq 0.085$ for undisturbed unbounded mixing layers, based on numerous independent experiments (Lesieur, 1997). Substitution of the velocity difference ΔU from Equation 3.11 and integration with respect to x leads to

$$\delta(x) = \alpha\frac{\Delta U_0}{U_c}\frac{D}{2c_f}\left(1 - \exp\left(-\frac{2c_f}{D}x\right)\right) + \delta_0 \tag{3.16}$$

The initial width δ_0 is imposed by the thickness of the boundary layers that have developed on both sides of the splitter plate and is approximately $\delta_0 \simeq D$. The virtual origin of the mixing layer is located upstream of the splitter plate apex. This expression differs in two respects from the expression proposed by Chu&Babarutsi (1988). First twice as high an entrainment coefficient was used by Chu&Babarutsi (1988). As discussed by Uijttewaal&Booij (2000), the need for this can be ascribed to a too short an inflow section in their experiments. Second, the extra empirical critical bottom friction parameter used by Chu&Babarutsi (1988) turned out not to be necessary.

Figure 3.3 shows the development of the width of the mixing layer as obtained from the measurements and the development as obtained by Equation 3.16. Some scatter is found in the measured mixing layer widths, which is ascribed to the sensitivity to errors of the determination of the mixing layer width due to the presence of the velocity gradient in the definition of the mixing layer width. The different measurement segments can also be distinguished by a kind of block behavior in the mixing layer width, but this is hardly noticeable in the velocity differences of Figure 3.2. No clear explanation was however found for this phenomenon. In any case, the modeled mixing layer width development is in fair agreement with the trend in the measurements.
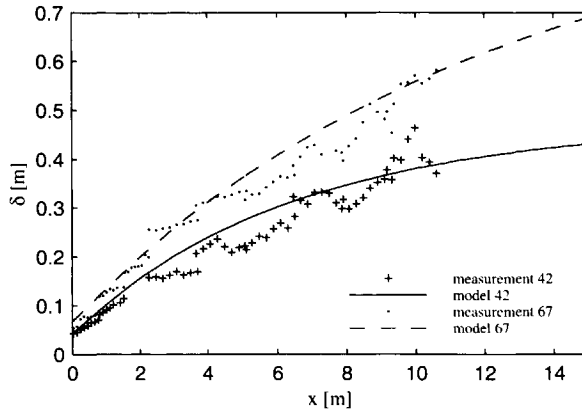
Figure 3.3: The measured and modeled (Equation 3.16) development of the mixing layer width for the Cases 42 and 67.

3.2.5 Lateral shift of the mixing layer

Due to the deceleration of the flow on the high velocity side and the acceleration at the low velocity side, the center of the mixing layer is displaced in the lateral direction to the low velocity side. To estimate this lateral shift, the center of the mixing layer is assumed to be a streamline of the mean flow field. An integral mass balance can then be derived for, for example, the high velocity side:

$$\int_0^{y_c(x)} DU(x,y)\mathrm{d}y = D\frac{W}{2}U_1(x_0) \tag{3.17}$$

from which y_c can be solved. The predicted shift of the center of the mixing layer is compared with the measurements in figure 3.4. The trend of the measurements is reproduced, although also for the lateral shift of the mixing layer some scatter is found in the measurements.

3.2.6 Total velocity field

The mean flow field is now completely determined by the Equation 3.7, 3.8, 3.11, 3.16 and 3.17 and the boundary conditions, i.e. the two inflow velocities and the water depth. The only empirical parameter used is the entrainment coefficient α, for which a value determined from unbounded mixing layers is used, which is correct since the mixing layer considered here is initially effectively unbounded. The value of c_f is well defined for fully developed flows over smooth surfaces. Figure 3.5 shows an overview of the measured and modeled mean streamwise velocity for Case 67. The model predicts the measured flow field rather well and the results are considered suitable as input for the stability analysis.
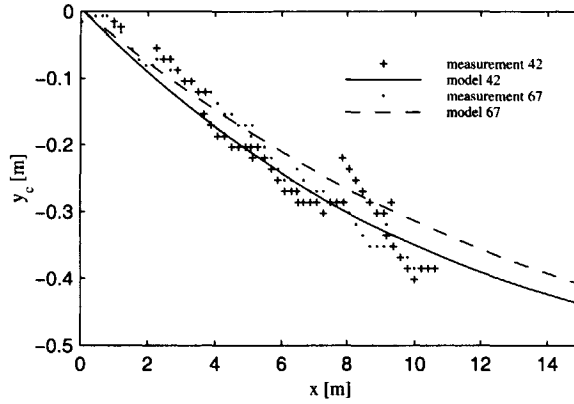
Figure 3.4: Development of the measured and modeled transverse position of the center of the mixing layer for the Cases 42 and 67.

It is noted that both experiments could be well described by the simple integral model, despite differences found between the coherent structures in the two cases. These differences therefore seem to be of limited importance for the widening of the mixing layer. This apparent contradiction is discussed in Chapter 4.
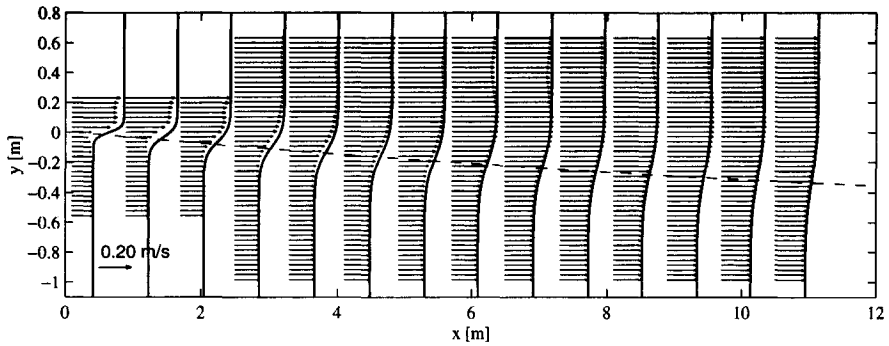
Figure 3.5: Velocity vectors (measurements) and profiles (model) of the mean velocity field of the Case 67. The dashed line indicates the position of the center of the mixing layer.

3.3 Stability analysis

3.3.1 Model description

A linear stability analysis of shallow water flows has been carried out by various authors (Alavian & Chu, 1985; Tamai *et al.*, 1986; Chu *et al.*, 1989; Chen & Jirka, 1998; Ghidaoui & Kolyshkin, 1999). The equations for the stability analysis used here are equal to the ones of Alavian&Chu (1985), but differ slightly from the analysis of Chu *et al.* (1989) and Chen&Jirka (1998; 1997). A short description of the model is given below.

The shallow water equations (Equation 3.1-3.3) are used as starting point. In contrast with the analysis by Chu *et al.* (1989) the viscosity term is maintained here. Chen&Jirka (1998) have demonstrated the importance of the turbulence viscosity since it affects the stability of the flow.

Following the common approach in linear stability analysis, small perturbations are superposed on the mean velocity and pressure:

$$\tilde{u} = U(x, y) + u(x, y, t) \quad \tilde{v} = v(x, y, t) \quad \tilde{p} = P + p(x, y, t) \tag{3.18}$$

Reynolds decomposition of the shallow water equations (Equation 3.1-3.3) results in equations for the perturbations. Dropping the higher order terms, this leads to:

$$\frac{\partial u}{\partial x} + \frac{\partial v}{\partial y} = 0 \tag{3.19}$$

$$\frac{\partial u}{\partial t} + U\frac{\partial u}{\partial x} + v\frac{\partial U}{\partial y} = -\frac{\partial p}{\partial x} - \frac{2c_f U}{D}u + \nu_t \left(\frac{\partial^2 u}{\partial x^2} + \frac{\partial^2 u}{\partial y^2} \right) \tag{3.20}$$

$$\frac{\partial v}{\partial t} + U\frac{\partial v}{\partial x} = -\frac{\partial p}{\partial y} - \frac{c_f U}{D}v + \nu_t \left(\frac{\partial^2 v}{\partial x^2} + \frac{\partial^2 v}{\partial y^2} \right) \tag{3.21}$$

The second term on the right-hand-side of Equation 3.20 and 3.21 is obtained from a first order Taylor expansion of the bottom friction contribution. It should be noted here that the bottom friction term used by Chen&Jirka (1997; 1998) is a factor 2 larger than the one in equation 3.21.

A normal mode solution of the form $[u, v, p] = [\hat{u}(y), \hat{v}(y), \hat{p}(y)] \exp(i(kx - \omega t))$ is assumed, in which k and ω are the complex wave number and frequency, respectively. Substitution of the normal mode solution into 3.19-3.21 results in:

$$ik\hat{u} + \hat{v}' = 0 \tag{3.22}$$

$$-i\omega\hat{u} + ikU\hat{u} + \hat{v}U' = -ik\hat{p} - \frac{2c_f U}{D}\hat{u} + \nu_t \left(\hat{u}'' - k^2\hat{u} \right) \tag{3.23}$$

$$-i\omega\hat{v} + ikU\hat{v} = -\hat{p}' - \frac{c_f U}{D}\hat{v} + \nu_t \left(\hat{v}'' - k^2\hat{v} \right) \tag{3.24}$$

The prime denotes the differentiation with respect to the lateral coordinate y. Eliminating $\hat{u}$ and $\hat{p}$, the set of equations (Equation 3.22- 3.24) can be reduced to:

$$(U - \frac{\omega}{k})(\hat{v}'' - k^2\hat{v}) - \hat{v}U'' = D_{bf} + D_{vis} \tag{3.25}$$

with

$$D_{bf} = i\frac{c_f U}{kD}(-k^2\hat{v} + 2\frac{U'}{U}\hat{v}' + 2\hat{v}'')$$

$$D_{vis} = i\frac{\nu_t}{k}(\hat{v}'''' - 2k^2\hat{v}'' + k^4\hat{v})$$

Equation 3.25 is similar to the Orr-Sommerfeld equation (Drazin & Reid, 1981). The terms on the right hand side are however different. The first term denotes the stabilizing influence of the bottom shear stress and the second term the stabilizing influence of the turbulence viscosity. The viscosity term differs from the viscosity term in the Orr-Sommerfeld equation in the use of an eddy viscosity, representing the small scale turbulence, instead of the molecular viscosity. The bottom friction term is a consequence of the depth-and-short-time averaged vertical shear, and is always stabilizing as follows directly from Equation 3.23 and 3.24.

The following boundary conditions are valid for unbounded shear flow:

$$\hat{v}(-\infty) = \hat{v}'(-\infty) = \hat{v}(\infty) = \hat{v}'(\infty) = 0,$$

The eigenvalue problem (Equation 3.25) can now be solved following a spatial approach or a temporal approach. The spatial approach assumes an exponential growth of the perturbations in downstream direction x. In that case the frequency of the disturbance ω is real, and k is complex, with k_r representing the wave number and k_i the spatial growth rate. The temporal approach assumes the disturbances to grow exponentially in time. In that case k is real and ω complex, with ω_i representing the temporal growth rate:

$$[u, v, p] = [\hat{u}(y), \hat{v}(y), \hat{p}(y)] \exp(i(kx - (\omega_r + i\omega_i)t))$$

As shown by Michalke (1965) the spatial approach covers the physical phenomenon of a spatial mixing layer slightly more precisely than the temporal approach. The eigenvalue problem of the spatial approach is however more complicated to solve than the eigenvalue problem of the temporal approach, due to the nonlinearity in k. For this study we have chosen to solve the temporal eigenvalue problem instead of the spatial one. The wave number is therefore real and will be denoted without a subscript $k = k_r$, unless defined differently. The temporal approach is allowed since the length scale over which the growth takes place is much larger than the length scale of the perturbations. A comparison of the temporal method with the spatial method (Chen & Jirka, 1998) will be made below. According to Gaster (1962), the spatial growth rate k_i^S can be determined from the temporal growth rate ω_i^T by $k_i^S = \omega_i^T/c^T$ with $c^T = \omega_r^T/k^T$ as the propagation velocity.

The eigenvalue problem of Equation 3.25 is solved for given wave numbers yielding the growth rate ω_i and frequency ω_r, by using a finite difference technique. The stability of the flow follows from the stability curves $(k, \omega_i(k))$. Perturbations with wave number k
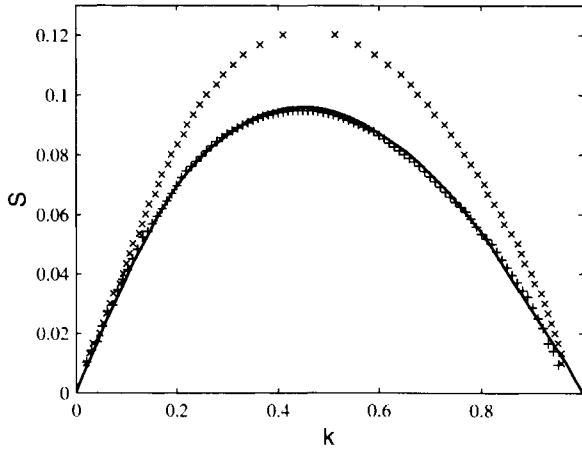
Figure 3.6: Neutral stability curves of an inviscid flow obtained with Equation 3.25 with the correct (x) and erroneous (+) bottom friction term and the result by Chen&Jirka (1998) (drawn line).

are growing if $\omega_i(k) > 0$. In order to validate the proposed temporal method for the linear stability analysis, a comparison is made with the inviscid calculations of Chen & Jirka (1998), who solved the eigenvalue problem with the spatial method. Stability curves are therefore calculated for a range of profiles, determined by the bed friction number defined by Alavian&Chu (1985) as:

$$ S = c_f \frac{\delta}{D} \frac{U_c}{\Delta U} $$

The zero-crossings of these curves determine the neutral stability curve, which is chosen as the criterion for comparison. The neutral stability curves determine the critical wave numbers where $\omega_i(k) = 0$. Figure 3.6 shows three different neutral stability curves. The first is the neutral stability curve according to the above described model, and the second is obtained from Chen&Jirka (1998). The difference between these curves is ascribed to the incorrect expression for the bottom friction term in the eigenvalue problem of Chen&Jirka (1998). Implementation of the erroneous bottom friction term into the current model results in the third curve, which coincides with the original curve of Chen&Jirka (1998). With this comparison the use of the temporal approach instead of the spatial approach is justified. In the following section the linear stability analysis model described above is used. We refer to Chen&Jirka (1998) for sensitivity analyses regarding the effects of bottom friction and eddy viscosity.
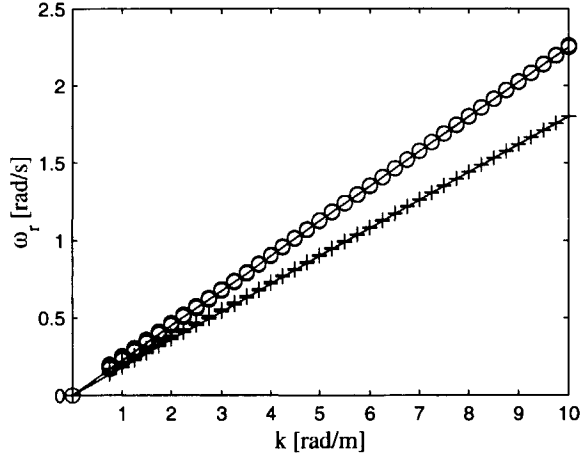
Figure 3.7: Dispersion relation for the Cases 42 (+) and 67 (o). The solid lines represent kU_c.

3.3.2   Experimental validation

The above described stability analysis is applied to the experiments described in chapter 2. The validated velocity profiles, computed with the 1d-model of Equation 3.7, are used as base flow. Stability curves are determined for a number of positions downstream of the splitter plate up to a length of 15m. The frequencies ω_r so determined are shown versus k in figure 3.7. The frequencies are linearly proportional to the wave numbers with a proportionality constant equal to the velocity at the center of the mixing layer, again justifying the use of the temporal method

Figure 3.8 shows the growth rates at three positions downstream of the splitter plate for both mixing layers. A positive value of the growth rate indicates growth of the perturbation of the particular wave number and a negative value indicates decay of that mode. For each position downstream, a maximum growth rate is found, determining the locally most unstable mode. The wave number of this unstable mode is close to $k \simeq 0.445/(0.5\delta)$ as found by Michalke (1964). The size of the most unstable mode is therefore proportional to the mixing layer width. The wave number of this most unstable mode decreases in downstream direction as reflected in the broadening of the mixing layer width.

The wavenumber of the most unstable mode is decreasing more rapidly for the Case 67 than for Case 42 as the mixing layer width is growing faster for the Case 67. The magnitude of the growth rate also decreases in downstream direction. This decrease in magnitude is stronger for Case 42 than for Case 67. The dissipative influence of the bottom friction is the same for each wave number, as directly follows from Equation 3.23 and 3.24. Note that the influence of the bottom friction is also implicitly present in the decrease of the mean velocity difference. The dissipation due to the turbulence viscosity is proportional to k^2, thus affecting the modes with large wave numbers more strongly than the modes with
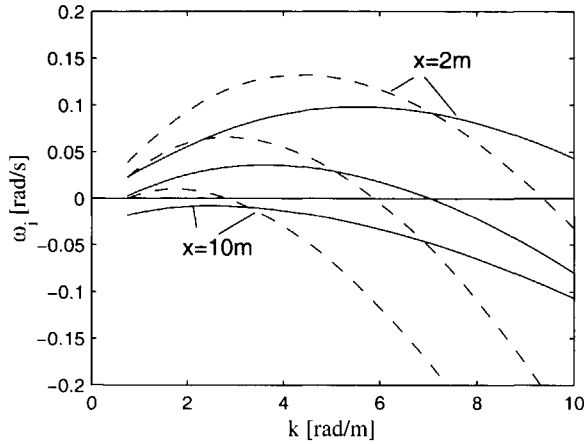
Figure 3.8: Stability curves for the Case 42 ( ) and Case 67 (- -) for different positions downstream (x=2, 4.5 and 10m).

small wave numbers.

Comparing the two cases shows that the growth rates of the modes with small wave numbers are larger for Case 67 than for the Case 42, because the influence of the bottom friction is smaller for the deeper Case 67. The growth rates of the modes for the large wave numbers are more strongly influenced by the eddy viscosity, resulting in smaller growth rates for Case 67 than for Case 42 in the high wave number range. In the case with bottom friction and/or viscosity, the dissipative terms can become larger than the production terms, resulting in a negative growth rate. For these cases existing disturbances are being dissipated and a stable situation is reached, as for example for Case 42 at $x = 10$m.

The stability curves of figure 3.8 represent the growth rate for various wave numbers at a given downstream position, but they do not predict the energy density of the wave numbers at that particular position. In order to find this energy density, the history of the development of the structures has to be taken into account. Integrating the growth rates over the streamwise coordinate yields an amplification factor for the initial perturbation. The energy density spectrum of the lateral velocity component for a certain position downstream x_1 can then determined by:

$$E(k, x_1) = E(k, x_0) \exp\left(2\frac{k}{\omega_r(k)} \int_{x_0}^{x_1} \omega_i(k, x)\mathrm{d}x \right) \qquad (3.26)$$

The initial spectrum denoted by $E(k, x_0)$ is assumed flat for small wave numbers, as found in the experiments. The initial energy density level is taken such that it equals the measured energy density at a position just downstream of the splitter plate, figure 3.9. The resulting spectra at several positions, which are obtained from Equation 3.26 by numerical evaluation of the integral, are plotted in figure 3.9a and b for Case 42 and Case 67 respectively. The
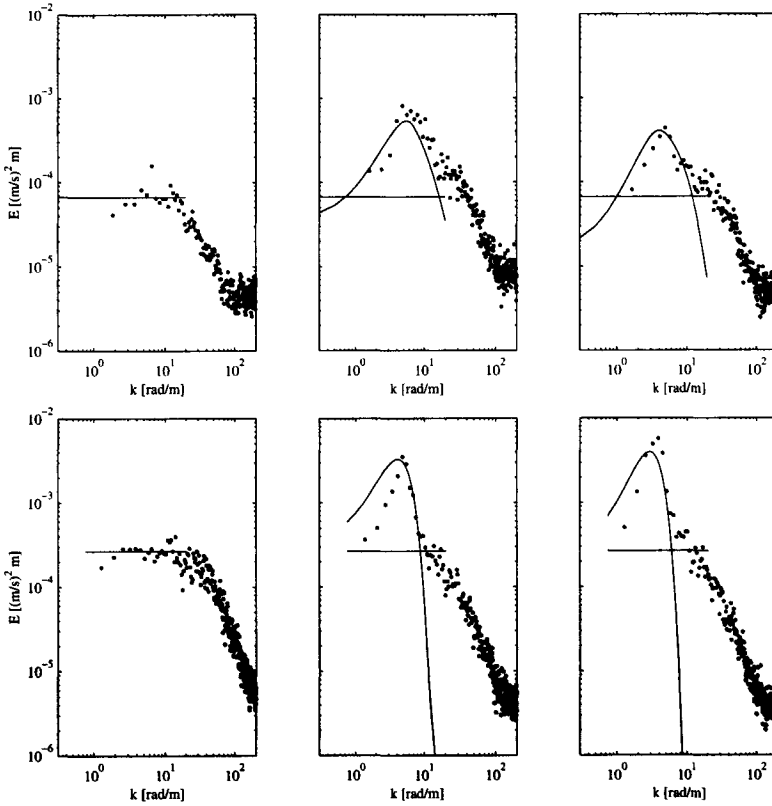
Figure 3.9: Measured ($\cdots$) and modeled ($-$) energy density spectra of the lateral velocity component v for Case 42 (top panels) and Case 67 (bottom panels) in the center of the mixing layer at the downstream positions x=0m (left), 4.5m (middle) and 10m (right).

measured energy density spectra of the lateral velocity obtained in the center of the mixing layer are plotted in the same figure, showing a remarkably good agreement. Since the measured spectra are obtained from time series, the frequency axes are converted to wave numbers by using the advection velocity (U_c).

The presence of large coherent structures is reflected in a significant peak in the spectra. Moving in downstream direction, the wave number of the peak shifts to the low wave number side, corresponding to an enlargement of the structures. The energy density of the peak is growing for the Case 67 over the full stretch, yielding more intense vortices. The peak in the spectrum of Case 42 at $x = 10$m is lower than the one at $x = 4.5$m, indicating a decrease in strength for the large coherent structures.

Figure 3.10: Development of the growth rates of the most unstable modes and the dominant modes for the Cases 42 and 67. The three different growth regimes are indicated for Case 67.

Although the linear stability analysis is used here beyond its limits of small perturbations, and the growth rates are integrated over a stretch several times the length scale of the perturbations, the analysis gives a good prediction of the energy density and the typical wave number of the coherent structures. The energy density in the high wave number range of the spectrum, which is influenced b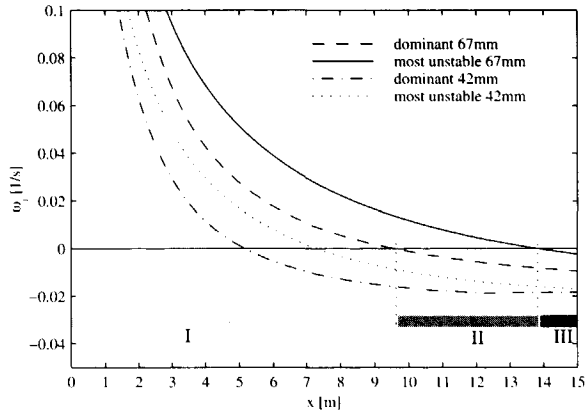y the dissipative small scale motion, is underestimated. Obviously Equation 3.5 does not fully apply to this range of the spectrum, because the small-scale three-dimensional motion in this range is not resolved in this analysis.

The successful prediction using a linear analysis suggests that the coherent structures are hardly influencing each other and that the energy density spectrum at a certain position downstream is governed by the spectral distribution of the turbulent kinetic energy at the inflow boundary.

In order to track the development of the large coherent structures, the dominant mode is followed. The dominant mode is defined as the wave number associated with the maximum energy density and is therefore representing the large coherent structures at a given downstream position. As mentioned earlier, the most unstable mode is the wave number for which the energy is growing fastest at that location.

The growth in intensity of the coherent structures in downstream direction is determined by following the growth of the dominant mode. The growth rates ω_i of the dominant modes are plotted as function of the downstream position x in figure 3.10. At a certain position downstream, the growth rate of the dominant mode becomes zero, indicating that from that position on the coherent structures are losing energy. The coherent structures are still present, but decaying. An unstable mode with positive growth rate can however still be found up to the downstream position where the most unstable mode has a growth rate equal to zero. From that position on the flow is stable and all perturbations will
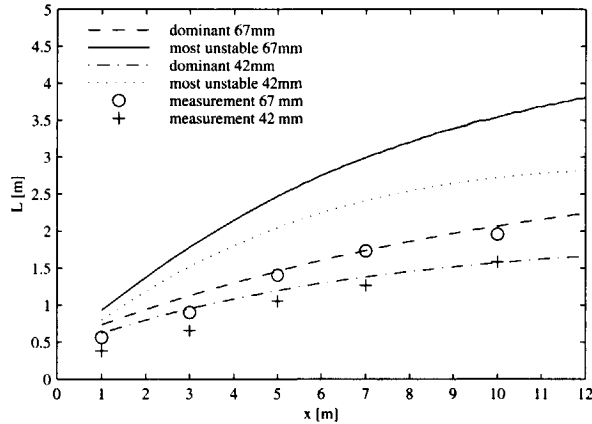
Figure 3.11: Development of the length scale of the most unstable mode, the dominant mode and the measured dominant mode for the Cases 42 and 67.

decay. At this position the bottom friction parameter has reached its critical value $S = S_c$ (Alavian & Chu, 1985).

Three different regimes can now be distinguished. These are indicated in figure 3.10 for Case 67. The first regime (I) is characterized by a positive growth rate of the dominant mode. In the second regime (II) the growth rate of the dominant mode is negative (the coherent structures are decaying), while some other modes still have positive growth rates. The flow is therefore not fully stable yet. The third regime (III) is the stable regime, in which all modes have negative growth rates. Although the flow is stable, coherent structures still might exist in this stable regime. As these large perturbations have a small wave number k, they are hardly influenced by the turbulence viscosity. The bottom friction is expected to be the dominating dissipation mechanism.

The development in downstream direction of the characteristic length scale associated with the coherent structures is related to the wave number of the dominant mode and can be determined from the modeled and measured spectra. The time scale of the dominant mode is determined by the frequency of the peak in the spectrum. Multiplying this time scale by the advection velocity results in the length scale of the dominant mode. The development of these measured and modeled length scales is plotted in figure 3.11 together with the development of the length scales of the most unstable modes. As demonstrated in figure 3.9, the modeled and measured length scales of the dominant modes are in good agreement. As figure 3.11 shows, the length scale of the most unstable mode is much larger than the length scale of the dominant mode. This is because the coherent structures generated upstream have had the opportunity to grow in strength while being advected downstream. The effect of the advection is made more clear in figure 3.12 by the dimensionless wave number $k^* = k\delta/2$ as also used by Michalke (1964). This normalized wave number of the most unstable mode is almost constant and close to the value of $k^* \simeq 0.445$ reported
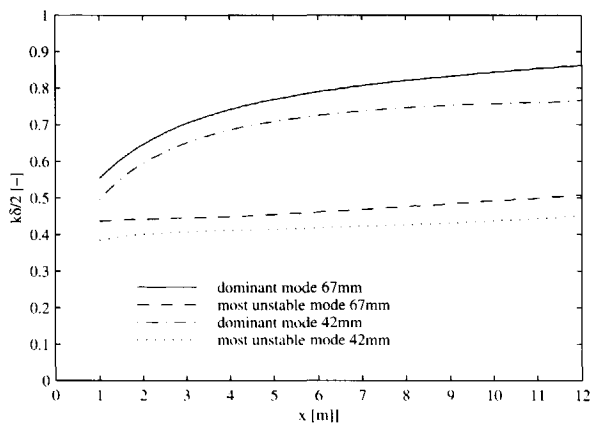
Figure 3.12: Development of the dimensionless wave number $k^* = k\delta/2$ of the most unstable mode and the dominant mode for the Cases 42 and 67.

by Michalke (1964) and Chu *et al.* (1989). The wave number of the dominant mode is not constant, but changes in downstream direction. The higher values found for the wave numbers of the dominant mode compared to the ones for the most unstable mode are a result of the development of the mixing layer width. The coherent structures generated upstream have larger wave numbers than the wavenumbers for the local most unstable mode. The wave number found far downstream is about twice as large as the wave number of the most unstable mode.

The most unstable mode is therefore not a suitable property for the characterisation of the large scale motion. It highly overestimates the size of the coherent structures. The accumulated energy of the coherent structures has to be taken into account for the determination of the typical length scale using the dominant mode instead of the most unstable mode.

3.4 Discussion and conclusions

In this chapter it has been demonstrated that with relatively simple techniques and means a detailed view can be obtained of the shallow mixing layer and its large scale structures.

The quasi-1D-model predicts a mean flow field in accordance with the measured flow field. The validity of the model suggests that the effects of shallowness on the mean flow field are mainly governed by the decrease of the velocity difference over the mixing layer as a result of bottom friction. The contribution of small scale three-dimensional turbulence to the growth rate of the mixing layer and the associated entrainment appears to be negligible. Only at downstream locations where Reynolds stresses in the horizontal plane have become of the same order of magnitude as those in the vertical plane, can a change

in the entrainment coefficient α be expected.

The use of a mean flow field as a base flow gives an extension to the use of linear stability analysis. In contrast with the classical analysis based on a single velocity profile for which the growth rates and the most unstable mode are determined at a single location, the use of a flow field here allows for the determination of the spatial evolution of the energy densities and the characteristic length scales. The development of the growth rate of the dominant mode shows that the flow 'stabilizes' (i.e. the dominant mode decays) well before the critical bottom friction number is reached $S = S_c$, where all modes decay. The critical bottom friction number, as proposed in Chu&Babarutsi (1988), is therefore not a useful number to characterize the large scale motion. Although the linear stability analysis is used here beyond its limits, the characteristics of the large scale motion are well predicted. This implies that the different modes hardly influence each other. A non-linear analysis is expected to yield a more strict criterion as to the extent in which the linear approach is justified.

A consequence of the validity of the linear stability analysis is that perturbations at the inflow determine the downstream development of the coherent structures, see Equation 3.26. This means that increasing the perturbation level at the inflow results in stronger coherent structures downstream. This hypothesis will be tested in the next chapter with a non-linear analysis.

Chapter 4

Effects of upstream large scale perturbations

4.1 Background

In Chapter 3, it was hypothesized that perturbations at the inflow boundary affect the downstream development of the coherent structures. This phenomenon will be investigated further in this chapter by means of numerical simulations and laboratory experiments.

The influence of imposed perturbations on the development of unbounded temporal and spatial mixing layers and the associated coherent structures has been investigated already by a number of authors, experimentally and numerically. Hussain&Zedan (1978a; 1978b) concluded from experiments that tripping the boundary layer along the splitter plate has significant influences on the downstream development of the mean profile and turbulence intensities. Experiments performed by Slessor *et al.* (1998) showed that tripping the boundary layers at the high speed side resulted in a decrease of the 2D organization of the large scale vortices. Another method for varying the inflow condition is to use an oscillating flap at the end of the splitter plate. Oscillations of various frequencies and amplitudes could be produced with such a flap, so different inflow conditions could be imposed. Single frequency forcing was imposed by Oster&Wygnanski (1982). The influence of double frequency forcing was investigated by Zhou&Wygnanski (2001). It was concluded from these experiments that excitation of the mixing layer with a single frequency results in higher turbulence intensities and a wider mixing region downstream than without excitations. A double frequency resulted in even higher turbulence intensities downstream.

High resolution numerical simulations of temporal mixing layers have for example been carried out by Balaras *et al.* (2001). They found that the initial perturbations had a considerable influence on the temporal development of the mixing layer. Different self-similar states were found for different initial perturbations.

From the above mentioned experiments and numerical simulations it is concluded that the development of coherent structures in mixing layers is affected by the turbulence at the inflow condition.

The shallow mixing layers considered in this study are different from unbounded mixing layers, as indicated above. The shallowness and the no-slip condition at the bottom result in bottom turbulence. Shallow mixing layers are therefore always perturbed to a certain extent by three-dimensional velocity fluctuations.

In this chapter the sensitivity of the development of the shallow mixing layer to three-dimensional perturbations is investigated.

First, numerical simulations are described. The large scale depth-averaged motion is resolved in these simulations and the small scale turbulence is modeled. As this kind of simulations is not unambiguous for relatively coarse grids, a classification of the different possible concepts for this kind of simulations is given first. Perturbations with different spectra are imposed at the inflow condition in order to investigate the downstream development of the coherent structures. It is not the aim to exactly reproduce the experimental results, but rather to analyze the influence of imposed perturbations on the development of the mixing layer and the coherent structures.

Second, laboratory experiments are carried out in which the turbulence level at the inflow is enhanced by covering the inflow segment with a bed of stones, generating three-dimensional turbulence. Point measurements are performed with a Laser Doppler Anemometer.

The numerical part of this chapter is partly published in Van Prooijen&Uijttewaal (2002b) and the experimental part in Van Prooijen *et al.* (2003) and De Nijs (2003).

4.2   Numerical simulations

4.2.1   Classification of modeling concepts

Turbulent flows can be simulated at different levels of detail, by making a difference between the resolved part and a modeled part. In this section the lowest, the highest and several intermediate levels of detail are discussed. The main difference between the approaches lies in the separation of the resolved part and the modeled part and in the associated model for the modeled part. The distinction between the levels of resolution is made clear by Spalart (2000) for a wake flow, Figure 4.1. The simulation at the lowest level of detail, Figure 4.1(left), does not show any coherent motion. Only the mean flow is resolved, the turbulent motion is entirely modeled. The simulation at the intermediate level of detail, Figure 4.1(middle), shows the Von Karman vortex street as a smooth large scale motion. The large scale motion is resolved, and the small scale motion is modeled. The simulation at the highest level of detail, Figure 4.1(right), shows in addition to the Von Karman vortex shedding also small scale instabilities. Most of the energy containing turbulent motion is resolved. The simulation at the highest level of detail is closest to reality, but the price for the detailed result is the high computational cost.

The lowest level of 'simulating' the turbulent flow is the Reynolds Averaged Navier Stokes (RANS) approach. The flow quantities are decomposed in a time mean and a fluctuation. The fluctuations include all the turbulent motions. Substitution of such a decomposition in the Navier Stokes equations leads to the well-known Reynolds equations, in which the effects of turbulent motion appears as the Reynolds stress. With these stresses the closure problem arises, which can be solved, in analogy with the viscous stresses in laminar flow, by using the eddy viscosity concept. The closure problem is now shifted to
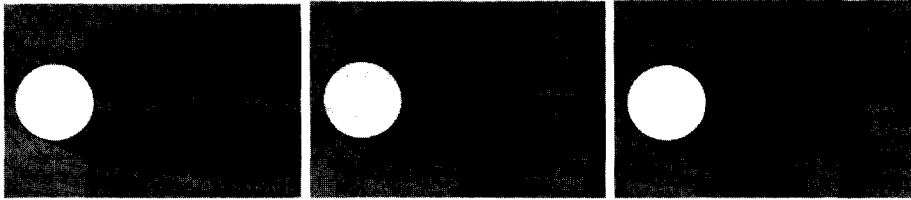
Figure 4.1: Simulations of a wake flow with a low (left), intermediate (middle) and high (right) level of detail (Spalart, 2000).

the determination of an effective eddy viscosity. The eddy viscosity is the product of a typical length and velocity scale $\nu_t = \mathcal{L}\mathcal{U}$. Different turbulence models can be used to determine these length and velocity scales. The most simple model for channel flows is the Elder formulation, $\nu_t = \alpha u_* D$, where the typical velocity scales with the friction velocity $\mathcal{U} \sim u_*$ and the length with the water depth $\mathcal{L} \sim D$.

In the case of multi-layered simulations more advanced models like the $k - \varepsilon$ model and its variants can be used. These models are however still based on a single length scale and cannot take into account the anisotropy of shallow shear flows. To this end, Bijvelds *et al.* (1999) developed a two-length scale model. The eddy viscosity is split into a two-dimensional and a three-dimensional part. This method has shown to be an improvement with respect to the single length-scale models. The advantage of the RANS-models is that relatively coarse grids can be used: mesh sizes depending on the length scales of the mean flow, which are generally larger than the water depth. The disadvantage is that the dynamics of the horizontal structures is poorly or not simulated.

The highest level of detail in resolving shallow water flow is based on the Large Eddy Simulation (LES) approach[1]. Overviews of LES can be found in textbooks (Sagaut, 1998; Pope, 2000). In the LES-approach the bottom turbulence is resolved and the very small scale isotropic motion is modeled. The separation between the resolved and modeled motion is visualized for LES in the spectral representation of Figure 4.2a. Implementing the decomposition in the Navier Stokes equations leads to the equations for the filtered motion. The closure problem in this equation remains for the filtered motion in the form of a subgrid shear stress. Again, the eddy viscosity concept is used. Often used subgrid models are the classical Smagorinsky model and the more sophisticated dynamic model (Germano *et al.*, 1991). The mesh size should be chosen in such a way that the cut-off wavenumber lies in the inertial subrange. At least 80% of the turbulent motion has to be resolved (Pope, 2000). This requirement disqualifies LES as an engineering tool for environmental flows in the next decades since the mesh size should then be at least an order of magnitude smaller than the water depth. A computationally less demanding simulation method is therefore desirable.

The approaches described above are widely accepted and used as tools in scientific re-

---

[1]Direct Numerical Simulation is not considered as it is far from feasible for our applications.
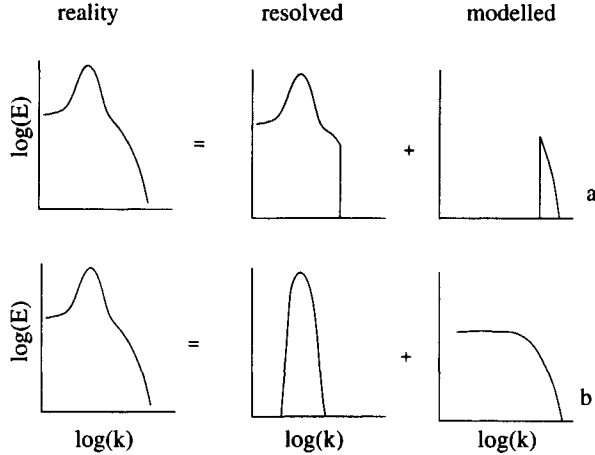
Figure 4.2: Sketches of the separation of the turbulent motion in a resolved and a modeled part according to the (V)LES-approach (top) and the TRANS-approach (bottom) (Sagaut, 1998).

search (RANS and LES) and in the engineering practice (RANS). A variety of approaches exists for simulations at intermediate levels of detail, like Transient RANS (TRANS) (Hanjalic, 2002), Unsteady RANS (URANS) (Spalart, 2000), sub-depth scale modeling (SDS-2DH) (Nadaoka & Yagi, 1998), Horizontal Large Eddy Simulation (HLES) (Kernkamp & Uittenbogaard, 2001), Very Large Eddy Simulation (VLES) (Pope, 2000). As the number of different names already suggests, none of the approaches is widely accepted. The intermediate approaches can be separated in two groups. The first group (VLES, HLES) is based on the same principle as Large Eddy Simulation. The turbulent motion is filtered like in LES, but the filter width is much larger. Just the horizontal large eddies are resolved. An aspect of discussion is the subgrid model which is more important than in a three-dimensional LES as a larger part of the turbulent motion has to be modeled. The cut-off wave number does not lie in the range where the turbulence can be considered isotropic and where the self-similar energy cascading takes place. Dedicated subgrid models are therefore needed as for example developed at Delft Hydraulics by Uittenbogaard (Kernkamp & Uittenbogaard, 2001). It is noted that this specific subgrid model only accounts for the depth-averaged fluctuations with length scales roughly smaller than the mesh size. The three-dimensional bottom turbulence is modeled with an Elder formulation (a RANS-approach).

The second group (TRANS, URANS, SDS-2DH) is related to the RANS approach. The turbulent motion is split in a very-large-scale coherent part and a non-coherent part over the full spectral range, see figure 4.2b (according to Sagout (1998)). The very-large-scale coherent part is to be resolved and the non-coherent part is to be modeled by a turbulence model as used in the RANS-approach. Consequently, the turbulence model is not a function of the mesh size. Different RANS-models are used in TRANS simulations of shallow water

flows, varying from the Elder formulation to for example non-linear $k - \varepsilon$ models (Kimura et al., 2002). A disputable aspect of this method is the separation between the very large scale coherent part and the non-coherent part and consequently the interpretation of the large scale coherent motion. It should be noted that strictly spoken all turbulent motions can be considered as coherent. Here we consider fully three-dimensional small-scale turbulence as non-coherent.

To the author's knowledge, no unambiguous method is known to split the non-coherent motion from the coherent one. In case of regular vortex shedding, as for example in wake flows (Von Carmer et al. (2001)), phase-averaging might be a possible method to split the coherent motion from the non-coherent one. A good illustration of the difficulty of interpreting the separation between coherent and non-coherent motion is given by Spalart (2000): "As an analogy, this type of averaging (phase averaging) would amount to averaging a number of human beings that walk by and do not have the same height. The average is not a human body." The results of a RANS-related-approach are therefore difficult to interpret.

In the case of shallow shear flows, a clear distinction can often be made between the typical length scales of the large-scale horizontal coherent motion and those related to the bottom turbulence (Nadaoka & Yagi, 1998). Although bottom turbulence contains some large scale components, as for example shown by Kim&Adrian (1999) and in Chapter 5, the energy content of this large scale bottom turbulence is much less than the energy content of the large-scale horizontal coherent motion. This implies that the phase averaged motion is almost equal to the low-pass filtered motion. Therefore the following procedure is proposed: the separation between the resolved motion and the modeled motion is made by low-pass filtering and the turbulence model is based on a RANS approach, 'independent' of the mesh size. A classical RANS model, like an Elder formulation, can be used. The mesh size then has to be in the order of the water depth as only the turbulent motions with length scales larger than the water depth need to be resolved.

It is noted that this assumption of interpreting the large scale coherent motion by the large scale motion is made implicitly in most of the studies on shallow water flows using a RANS-type turbulence model (Nadaoka & Yagi, 1998; Kimura et al., 2002; Hinterberger et al., 2002; Bousmar, 2002).

For convenience the term 2D-TRANS (two-dimensional Transient Reynolds Averaged Navier-Stokes) is used for the applied procedure from now on.

4.2.2 Model description

As described in the former subsection the only method to simulate shallow water flows in which the large scale coherent structures are resolved, without too high a computational effort, is a simulation at the intermediate level of detail, a 2D-TRANS simulation. The details of this model will be described here for application to a shallow mixing layer.

Governing equations

The short-time depth-averaged shallow water equations with rigid lid are used:

$$\frac{\partial \tilde{u}}{\partial x} + \frac{\partial \tilde{v}}{\partial y} = 0 \tag{4.1}$$

$$\frac{\partial \tilde{u}}{\partial t} + \tilde{u}\frac{\partial \tilde{u}}{\partial x} + \tilde{v}\frac{\partial \tilde{u}}{\partial y} = -\frac{1}{\rho}\frac{\partial \tilde{p}}{\partial x} - \frac{c_f}{D}\tilde{u}\sqrt{\tilde{u}^2 + \tilde{v}^2} + \nu_t \nabla^2 \tilde{u} \tag{4.2}$$

$$\frac{\partial \tilde{v}}{\partial t} + \tilde{u}\frac{\partial \tilde{v}}{\partial x} + \tilde{v}\frac{\partial \tilde{v}}{\partial y} = -\frac{1}{\rho}\frac{\partial \tilde{p}}{\partial y} - \frac{c_f}{D}\tilde{v}\sqrt{\tilde{u}^2 + \tilde{v}^2} + \nu_t \nabla^2 \tilde{v} \tag{4.3}$$

with the constant water depth D, pressure p, the velocities u and v in the streamwise and transverse directions x and y, the bottom friction parameter c_f, the turbulence viscosity ν_t. The tilde ~ denotes the short-time-depth-averaging operator. As the Froude number is small for the studied cases the rigid lid assumption for the free surface is justified.

The turbulence viscosity is an important parameter as already discussed in the former section because it reflects the closure problem. A turbulence viscosity based on the friction velocity u_* and the water depth D (Elder formulation) is chosen:

$$\nu_t = \alpha u_* D \tag{4.4}$$

with the empirical constant $\alpha = 0.05 - 0.2$ (see Fisher (1979)). Here a value of $\alpha = 0.15$ is used, comparable to the value used in Chapter 3.

Numerics

A finite volume method based on the model of Eggels (1994) is used to perform the 2D-TRANS simulations. For spatial discretization of the governing equations, a simple second order accurate central differencing scheme is used on a staggered equidistant orthogonal grid. The coupling of the pressure to the momentum equations is done with the pressure-correction method. The second order explicit Adams-Bashfort scheme is used for time discretization. Since an explicit method for the time discretization is used, the Courant-Friedrich-Lewy number is set to $CFL = 0.35$ to assure stability. The tridiagonal matrix is solved with Gauss elimination. Tests were carried that confirmed the negligible influence of numerical dissipation, but these are not discussed here.

Flow conditions and numerical parameters

The flow conditions are chosen in accordance with experiment Case 67 as described in Chapter 2. The computational domain starts just downstream the splitter plate and represents a length $L = 17$m, a width $W = 3$m and a depth $D = 0.067$m. As the flow is assumed to be two-dimensional, length scales smaller than the water depth are not resolved, but modeled. In order to represent motion with a length scale of the order of two times the water depth, a mesh size of $\Delta x = \Delta y = 0.3D = 0.02$m is used. This results in a

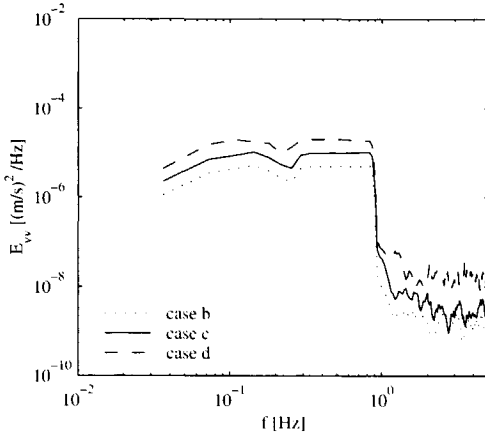|	$E(k)\,[c_f U(y)^2 D]$
Case a	0
Case b	0.05
Case c	0.1
Case d	0.2

Figure 4.3: (left) The energy density spectra of the transverse velocity fluctuations realized just downstream the splitter plate. (right) Energy density values for the low-frequency range.

grid with 850×150 cells. The time step is set to $\Delta t = 0.02$s, assuring $CFL < 0.35$. Free-slip conditions are imposed at the side boundaries. At the outflow an advective boundary condition is imposed.

Special attention is paid to the inflow boundary condition. It follows from the linear stability analysis of Section 3.3, that existing perturbations are amplified in the mixing layer. The imposed perturbations are therefore expected to play a significant role in the further development of the mixing layer and the large scale coherent structures. The inflow boundary condition is prescribed as a mean flow profile with perturbations superposed on it. The transverse profile of the mean streamwise velocity is prescribed by a hyperbolic tangent, with a mixing layer width of $\delta(x_0) = D$ and velocities outside the mixing layer $U_1 = 0.32$m/s and 0.13m/s.

The inflow boundary is perturbed by making use of a kinematic simulation. A 'turbulent' flow field is generated by a number of Fourier modes. The modes are chosen such that the flow field approximately satisfies continuity and obeys a uniform energy density spectrum. The flow field thus obtained is advected into the domain with the local mean velocity, making use of the frozen turbulence hypothesis. The velocity fluctuations at the inflow boundary are prescribed by means of a kinematic simulation (see for example Fung *et al.* (1992)):

$$u(x,y) = \sum_{n=1}^{N} \sqrt{\frac{k \cdot N}{N} E(k^n)} \frac{k_y^n}{k^n} \sin\left(2\pi(k_x^n U(y)t + k_y^n y) + \phi^n\right) \tag{4.5}$$

$$v(x,y) = -\sum_{n=1}^{N} \sqrt{\frac{k \cdot N}{N} E(k^n)} \frac{k_x^n}{k^n} \sin\left(2\pi(k_x^n U(y)t + k_y^n y) +^n\right) \tag{4.6}$$

$$k_x^n = \cos(\theta^n)k^n, \quad k_y^n = \sin(\theta^n)k^n, \quad k^n = \sqrt{k_x^{n2} + k_y^{n2}} \tag{4.7}$$

with k^n the wave number of mode n, N the number of Fourier modes, k^N the cut-off wave number, $E(k^n)$ the power density spectrum, ϕ^n a random phase shift and θ^n a random angle. The number of Fourier modes is set to $N = 200$, with the wavenumbers equally distributed from k^N/N to k^N. The cut-off wavenumber has to be at least smaller than the wavenumbers that cannot be resolved, $k < \frac{2\pi}{D}$. Measured 1D-velocity-spectra of open channel flow turn out to have a more or less constant energy density level for the low frequency range. A homogeneous spectral density is therefore assumed for the wavenumbers $k^n < k^N$ with different magnitudes of E, given in Figure 4.3(right). The energy density spectra of the transverse velocity fluctuations as realized just downstream from the inflow boundary are given in figure 4.3, showing an almost flat spectrum up to the imposed cut-off frequency.

4.2.3 Statistical analysis

The influence of the perturbation amplitudes on the mean flow field is reflected in the development of the mixing layer width, defined by the ratio between the velocity difference and the transverse gradient of the streamwise velocity in the center of the mixing layer, Equation 3.6. Figure 4.4 shows the downstream development of the mixing layer width for the different flow conditions. The growth of the mixing layer for Case a is significantly smaller than for the other cases. The relatively slow widening of the mixing layer width for Case a is associated with the absence of coherent structures. The widening is governed by small scale three-dimensional turbulence modeled by the eddy viscosity. Note that a completely undisturbed inflow condition can principally not be reached as there are always discretization errors. The intensity of these perturbations is however too small to cause
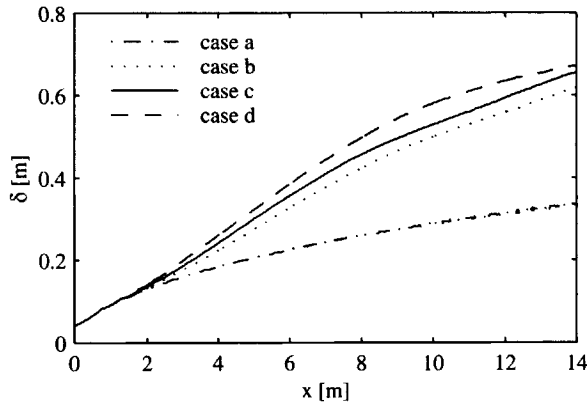
Figure 4.4: The development of the mixing layer width.
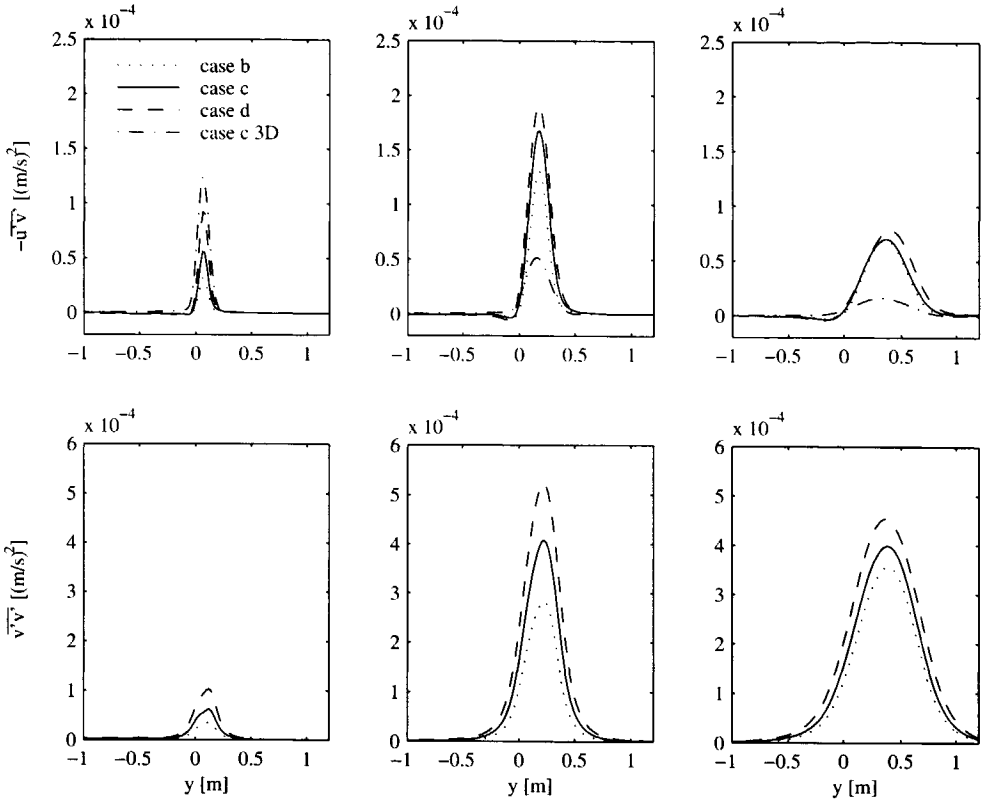
Figure 4.5: Transverse profiles of the Reynolds stress (top) and transverse normal stress (bottom) for the positions $x = 2$m (left), $x = 5$m (middle) and $x = 10$m (right).

significant effects in the computational domain.

The development of the mixing layer width is almost similar for the Cases b, c and d. The width increases slightly with increasing level of upstream perturbations. In the presence of coherent structures, the mixing layer grows faster as momentum is exchanged in transverse direction by the coherent structures. However, the effects on the mean flow of the inflow perturbations for the Cases b, c and d differ mutually not much compared to the difference with Case a.

Reynolds stress profiles are plotted at the top of figure 4.5 for different positions downstream: $x = 2$m, $x = 5$m and $x = 10$m for the Cases b, c and d. For Case a, Reynolds stresses could not be calculated due to the absence of coherent structures. For the other cases, a peak is found in the center of the mixing layer. Initially the peak grows in downstream direction, until it reaches its maximum value. From this position on, the peak value

decreases again. This development is associated with the growth and decay of the coherent structures, as described in Chapter 2. Initially, at $x = 2$m, a significant difference is found between the Cases b, c and d. The ratio between the maximum stresses for the Cases b and d is $\overline{u'v'}_{\text{max,d}}/\overline{u'v'}_{\text{max,b}} = 3.1$. The ratio is smaller at $x = 5$m: $\overline{u'v'}_{\text{max d}}/\overline{u'v'}_{\text{max b}} = 1.5$. In the far field, $x = 10$m, the difference has almost vanished: $u_{\text{max d}}/u_{\text{maxb}} = 1.1$. In addition to the Reynolds stress profiles of the large scale motion, the Reynolds stress profiles of the small scale turbulence, as modeled by the Elder formulation, are plotted for Case c (labeled as Case c 3D). The modeled shear stresses for the Cases b and d are very similar. However, the shear stresses for Case b are slightly higher and for Case d slightly smaller. The differences between the total shear stresses are therefore smaller than the differences between the resolved shear stresses suggest. The widening of the mixing layer is initially dominated by small-scale three-dimensional motion, which is not resolved. Further downstream the resolved Reynolds stresses dominate.

The transverse normal stresses are plotted at the bottom of figure 4.5. Significant differences are found at $x = 2$m: $\overline{v'v'}_{\text{max d}}/\overline{v'v'}_{\text{max b}} = 3.8$ and $x = 5$m: $\overline{v'v'}_{\text{max d}}/\overline{v'v'}_{\text{max b}} = 1.9$. At $x = 10$m the differences are small, although still present: $\overline{v'v'}_{\text{max d}}/\overline{v'v'}_{\text{max b}} = 1.3$. The differences between transverse normal stresses of the different cases appear larger than the differences between the Reynolds shear stresses.

It is concluded that the formation of coherent structures plays a role in the widening of the mixing region. In Case a, in which the coherent structures were absent, a significantly smaller growth of the mixing layer width was found compared to the Cases b, c and d, in which coherent structures were present. The influence of a difference in upstream perturbations on the width of the mixing layer is however limited. Increasing the intensity of the inflow perturbations results in a slightly wider mixing layer. Higher turbulence levels at the inflow result in higher turbulent stresses downstream. The differences are more pronounced in the transverse stresses than in the Reynolds stresses. Far downstream the influence of the inflow perturbations vanishes.

4.2.4   Spectral analysis

Figure 4.6 shows power density spectra of the transverse velocity fluctuations for Case c in the center of the mixing layer, at different positions downstream. The peak in the spectrum is associated with the coherent structures. Going in downstream direction, the peak grows in intensity up to a maximum as energy is picked up from the mean shear. Further downstream the peak intensity decreases. The frequency of the peak shifts to the low frequency range as the mixing layer broadens. A growth of the intensity and the shift of the peak to the lower frequency range reflects the same trend as found in the measurements of Chapter 2.

Figure 4.7 shows normalized power density spectra of the transverse velocity fluctuations for the Cases b, c and d at the downstream positions $x = 2$m, $x = 5$m and $x = 10$m. These spectra have been made dimensionless with the spectra at the inflow:

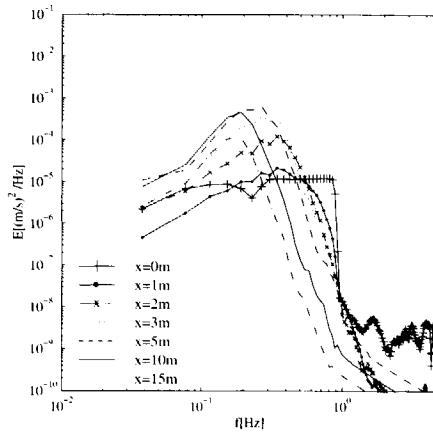$$F(f) = \frac{E(f, x_1)}{E(f, x_0)}$$

Figure 4.6: Power density spectra of the transverse velocity for Case c.

These dimensionless power density spectra can be interpreted as amplification functions. They represent the amplification of the energy density of each mode over a certain reach.

According to the linear stability analysis proposed in Chapter 3, perturbations will grow as a function of the transverse variation of the mean streamwise velocity. In figure 4.4 it was shown that the differences in mixing layer width between the Cases b, c and d were small. Based on the linear stability analysis, similar amplification functions are therefore expected.

At $x = 2m$ the amplification spectra are virtually equal. The inflow perturbations develop in a similar way in downstream direction. At $x = 5m \simeq 75D$, small deviations are found, which are largest for the higher frequency modes, which can be explained by the influence of the turbulence eddy viscosity. The difference in peak energy density is small ($F_{max,c}/F_{max,b} = 1.2$). At $x = 10m$ more significant differences are found, with a peak ratio of $F_{max,c}/F_{max,d} = 1.6$. The ratio between the peak values of Case c and Case b is however still quite small ($F_{max,c}/F_{max,b} = 1.2$). Especially the amplification function of Case d deviates from the other two. The explanation for the differences can be found partly in the differences in development of the mixing layer width. More intense coherent structures lead to a higher growth rate of the mixing layer and therefore a wider mixing layer. This wider mixing layer results in less production of kinetic energy and therefore in relatively lower energy density levels. The highest amplification functions are therefore found for the case with the weakest coherent structures, Case b. Another explanation for the differences in amplification levels are non-linear effects, like the merging of two vortices to a larger one. This was observed for Case d. The larger shift of the peak to the low frequency range in this Case d, is another indication of the merging process. Obviously, these non-linear effects are strongest for intense vortices.

It is concluded from the spectral analysis that inflow perturbations have an important influence on the downstream development of the energy density spectra. Almost similar dimensionless power density spectra are found for the Cases b, c and d indicating linear behavior. However, relatively far downstream $(x > 100D)$, non-linear effects become important especially in the case of intense vortices.
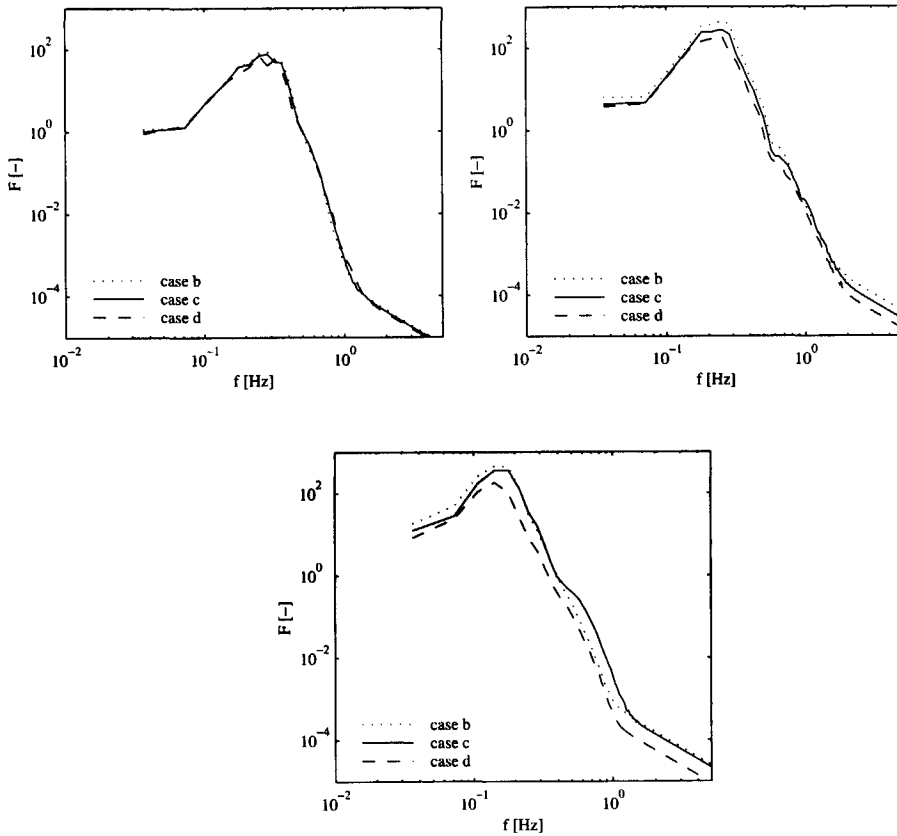

Figure 4.7: Amplification spectra at $x = 2$m (top left), $x = 5$m (top right) and $x = 10$m (bottom).

4.3   Experiments

In the preceding section the influence of perturbations at the inflow on the development of large coherent structures was investigated by means of numerical simulations. In this section laboratory experiments are discussed in which the inflow perturbation level is varied.

4.3.1   Experimental set-up

Two cases are studied in the shallow flow facility that has been described in Chapter 2. The distinction between both experiments was determined by the energy density level of the perturbations generated at the inflow boundary. In experiment 1, turbulence is generated by the flow over a smooth bottom. In experiment 2 additional perturbations are evoked by means of a bed of submerged stones (Figure 4.8). The stones have a mean diameter of approximately $D = 3$cm and are placed in a staggered pattern on a grid with a meshsize of 0.04m. For both cases the discharge is kept the same. The flow conditions, the water depth and velocities, are chosen in such a way that the flow is turbulent and subcritical.

Laser Doppler Anemometry (LDA) data are presented here; see Uijttewaal&Booij (2000) for details about the LDA-system used. The glass bottom allows for optical access from below. For each position about 10^5 bursts were detected in a period of about ten minutes. This data rate allowed for a sampling rate of 100 Hz, which is sufficient for the investigation of the large scale horizontal structures with typical time scales larger than one second. Measurements have been performed at two different positions downstream of the splitter plate, at $x = 0.4$m and in the far field at $x = 5.0$m. For each position the streamwise and transverse velocity is measured simultaneously at $z = 0.6D$.

4.3.2   Statistical analysis

The mean velocity profiles for both experiments are shown in Figure 4.9 for $x = 0.4$m and in figure 4.10 for $x = 5.0$m. At the position closest to the inflow section (figure 4.9), differences between the two profiles are found. The center of the mixing layer lies at $y = 0$ for experiment 1, while it is shifted to the high velocity side in experiment 2. The mixing layer is wider for experiment 2 than for experiment 1 and a strong spatial oscillation is found on the high velocity side of the mixing layer of experiment 2. A number of three-dimensional effects play a role in this region, what makes it too speculative to address the different mechanisms causing these differences.

Figure 4.10 shows that at $x = 5.0$m the differences between the mean velocities in the two experiments are small. Therefore, the higher turbulence intensity at the inflow has no significant effect on these mean velocity profiles. It is noted here that also in the numerical simulations described earlier in this chapter just a slight difference was found between the cases with differing inflow conditions.

The turbulent normal and shear stresses $\overline{u'u'}$, $\overline{v'v'}$ and $\overline{u'v'}$ are also plotted in the figures 4.9 and 4.10 for the two downstream positions. At $x = 0.4$m a distinct peak is found for all stresses in the center of the mixing layer for experiment 1. The peak values

of the stresses are of the same order of magnitude. The peak is therefore associated with the presence of turbulent structures developing in the mixing region. No such peak is found at $x = 0.4$m for experiment 2. With the small mixing layer width here, turbulent motion appears to be dominated by the three-dimensional turbulence generated in the wake of the stones. The stresses $\overline{u'u'}$, $\overline{v'v'}$ scale with the mean velocity squared. The shear stress $\overline{u'v'}$ shows a different behavior. A peak is found in the center of the mixing layer. Outside the mixing layer the shear stress is relatively small compared to the normal stresses. Outside the mixing layer both positive and negative values are found, because positive and negative gradients of the mean streamwise velocity exist as a result of the inhomogeneities introduced by the bed of stones. The distance between the maxima is comparable with the distance between the stones. A much stronger spatial oscillation is found on the high velocity side than on the low velocity side.

At the downstream position $x = 5.0$m all stress profiles have a peak in the center of the mixing layer. The turbulent motion in the mixing layer is dominated by the large coherent structures in both experiments. A significantly higher peak value for the normal stresses and the shear stress is found for experiment 2 than for experiment 1. The peak values
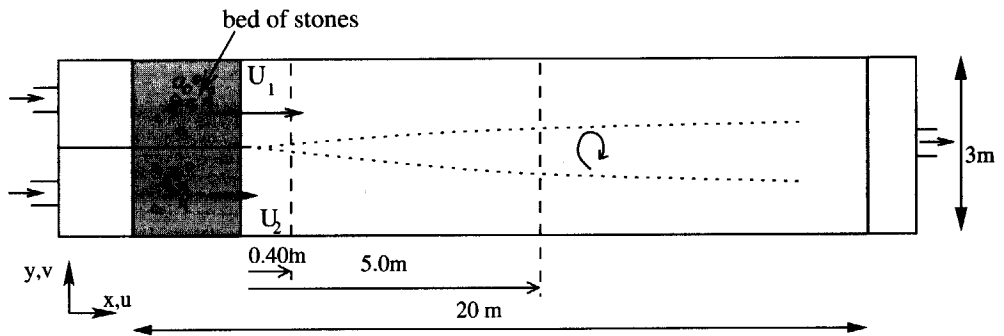
D [mm]	U_1 [m/s]	U_2 [m/s]
85	0.33	0.11

Figure 4.8: Sketch of the top view of the measurement set up (top), a picture of the inflow section covered with stones (bottom left), and the flow parameters at the inflow boundary (bottom right).
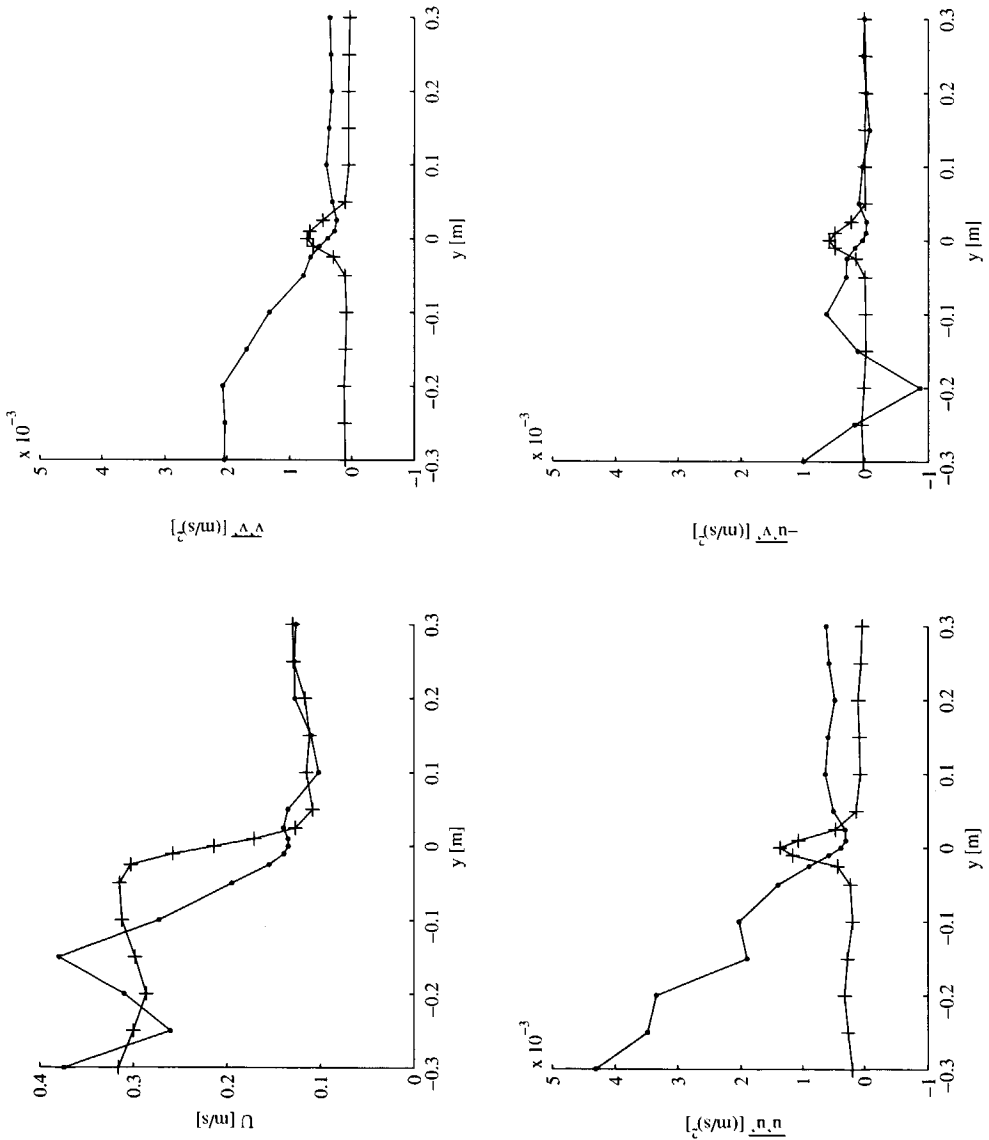
Figure 4.9: Transverse profiles of the mean streamwise velocity and the turbulence stresses at $x = 0.40$m for experiment 1 (+) and experiment 2 (·).
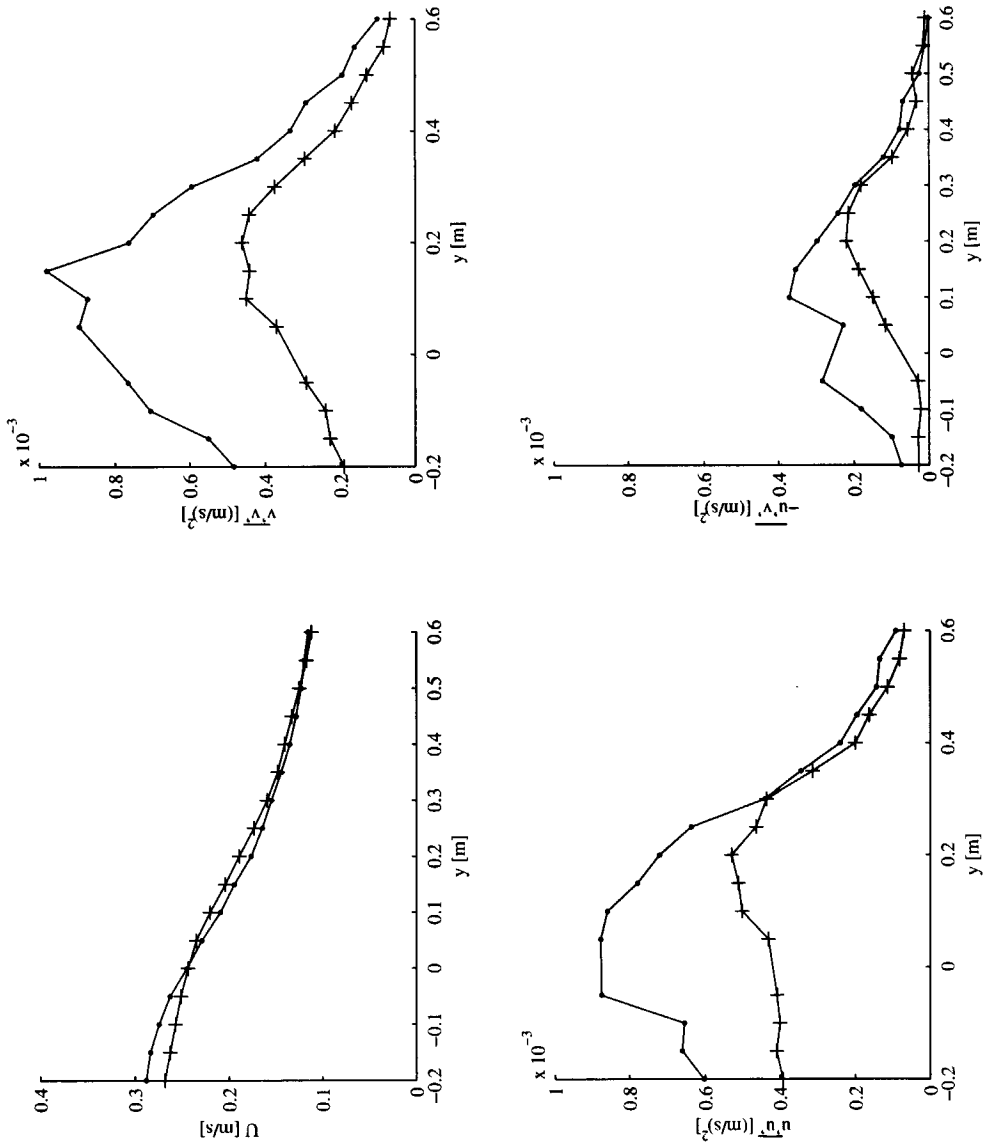
Figure 4.10: Transverse profiles of the mean streamwise velocity and the turbulence stresses at $x = 5$m for experiment 1 (+) and experiment 2 (·).
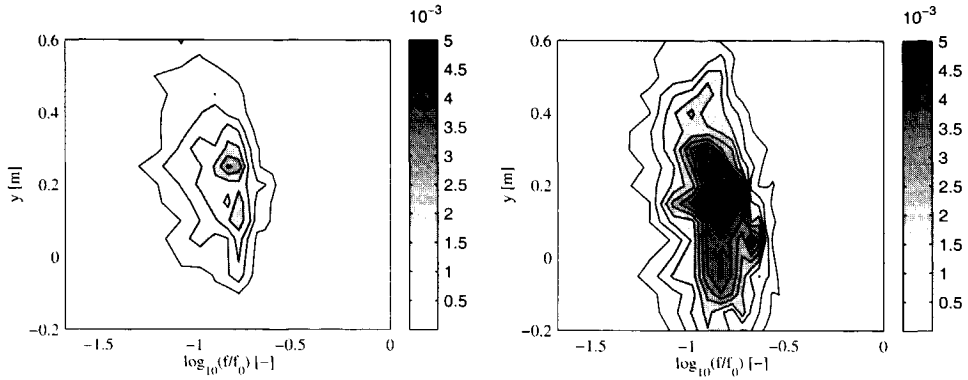
Figure 4.11: Power density contour values ($E_{vv}[(\mathrm{m/s})^2/\mathrm{Hz}]$) at $x = 5.0\mathrm{m}$ for experiment 1 (left) and experiment 2 (right). The frequency is made dimensionless with $f_0 = 1\mathrm{Hz}$. The contour interval is set to $\Delta E_{vv} = 0.0004(\mathrm{m/s})^2/\mathrm{Hz}$

differ a factor 1.8 for $\overline{u'u'}$ and $\overline{u'v'}$ and a factor 2.0 for $\overline{v'v'}$.

Enhancement of the turbulence intensities by the bed of stones has resulted in higher turbulence stress levels downstream, but not in a wider mixing layer.

4.3.3   Spectral analysis

A difference between the two experiments was found with respect to the turbulent stresses. However, it cannot be concluded from these stresses whether the turbulent kinetic energy can be associated with the horizontal coherent structures. To investigate this, energy density spectra are used.

Contours of the energy density of the transverse fluctuations at $x = 5.0\mathrm{m}$ are plotted against the frequency and the transverse position in figure 4.11. The coherent structures are represented by a bulge in the spectra that are measured in the mixing region, see also Chapter 2. In both experiments a maximum is found in the center of the mixing layer at a frequency of $f \simeq 0.15\mathrm{Hz}$. There is some scatter in the contours, but the bulge as found for experiment 2 is substantially higher than the one for experiment 1.

The spectra E_{vv}, E_{uu} and E_{uv} in the centers of the mixing layers at the positions $x = 0.4\mathrm{m}$ and $x = 5.0\mathrm{m}$ are plotted in figure 4.12. In the near field, a higher energy density level in the high frequency range is found for experiment 2. A peak is found at about $f = 0.8\mathrm{Hz}$, indicating the presence of turbulence structures.

At the downstream position $x = 5.0$ m, significant peaks are found in E_{vv} and E_{uv}. Such a peak is less profound in the spectra E_{uu}, as these spectra are contaminated by the varying transverse locations where the coherent structures pass. A much higher peak value is found for experiment 2. These data suggest that the large scale coherent structures are more intense for experiment 2. This confirms the hypothesis of the linear theory, in the

sense that perturbations at the inflow affect the development of the coherent structures downstream.

According to the linear stability analysis, perturbations will grow as function of the transverse profile of the mean streamwise velocity. The mean velocity profiles of the two experiments are almost the same. The inflow perturbations are then expected to be amplified in the same way. The ratios of the spectral densities of the modes at the two positions, the amplification functions as formulated in Equation 4.2.4, therefore are expected to be the same. Figure 4.13 shows the amplification functions for both experiments. Despite some scatter, they are quite similar in the low frequency range, indicating the validity of the proposed linear behavior.

4.4   Discussion

The simulations of a shallow mixing layer presented in this chapter show the dependency on the imposed perturbations at the inflow boundary. If no perturbations are imposed, no large scale structures are found on the downstream reach of the domain. Imposing perturbations on the inflow boundary does result in the development of large coherent structures. From the numerical simulations and the experiments the following is observed:

- From the numerical simulations it followed that higher turbulence levels at the inflow result in slightly wider mixing layers. No measurable differences were found in the widths of the mixing layers for the two experiments.

- Higher normal and shear stresses $\overline{u'u'}$, $\overline{v'v'}$ and $\overline{u'v'}$ are found for cases with higher inflow turbulence levels, in the experiments as well as in the numerical simulations.

- In the experiments and in the numerical simulations, higher energy density levels are found for cases with higher inflow turbulence levels.

There seems to be a contradiction between the first and the second item. On the one hand higher turbulence levels at the inflow result in stronger vortices, but on the other hand no significant differences are found in the mean profiles. This behavior is also found for the experiments of Chapter 2. Significant coherent vortices were found for Case 67, which were growing over the full domain, whereas weak vortices were found in Case 42, which were dissipating soon after the splitter plate. Despite these differences in coherent structures, the mean velocity field could be described well by a simple quasi one-dimensional model, which did not take into account the development of coherent vortices. Similar behavior is found by Dracos *et al.* (1992). In these shallow jet experiments significant differences were found in the development of the intensity of the coherent structures, but the spreading rate of the jet turned out to be the same. No explanation was given for this contradiction.

Apparently the intensity of the coherent structures has no direct influence on the broadening of the mixing layer, although this was expected, as stronger vortices should result in an increase in momentum exchange.

In Chapter 3, it was concluded that the large scale motion behaves mainly linearly. This implies that inflow perturbations are amplified mainly depending on the mean velocity
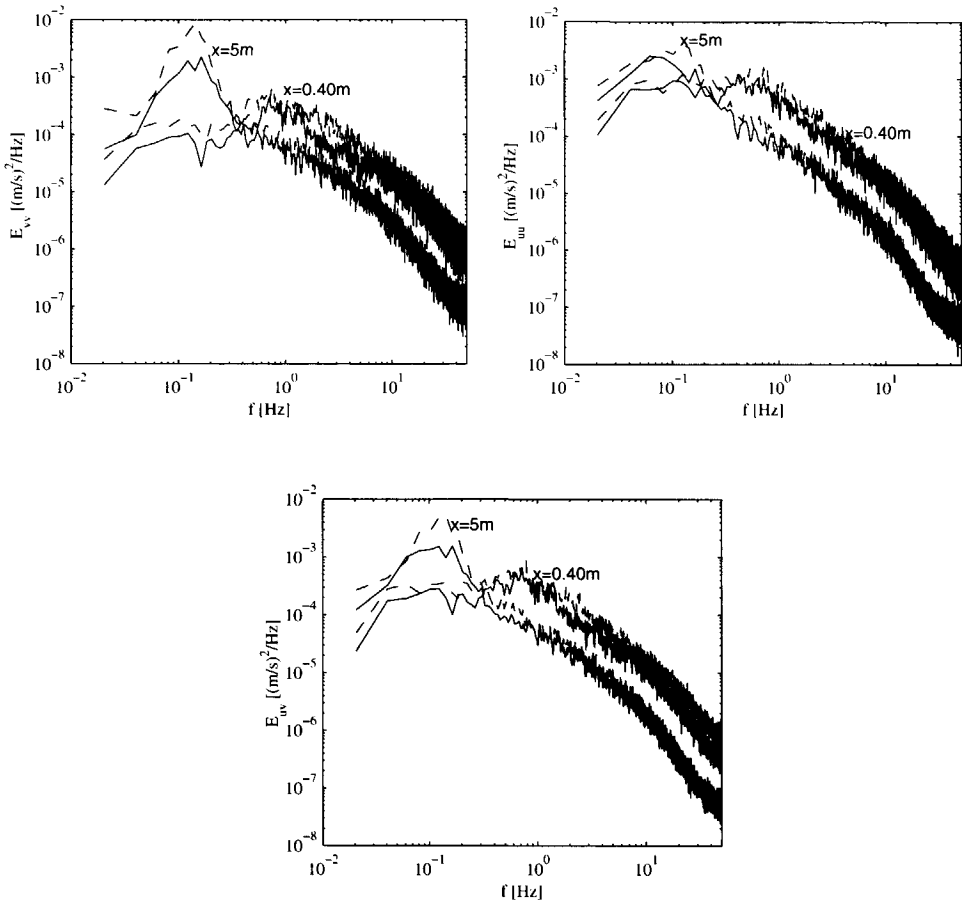
Figure 4.12: Transverse velocity power density spectra E_{vv} (top left), E_{uu} (top right) and E_{uv} (bottom) for the positions $x = 0.4$m and $x = 5.0$m for experiment 1 (–) and experiment 2 (- -).
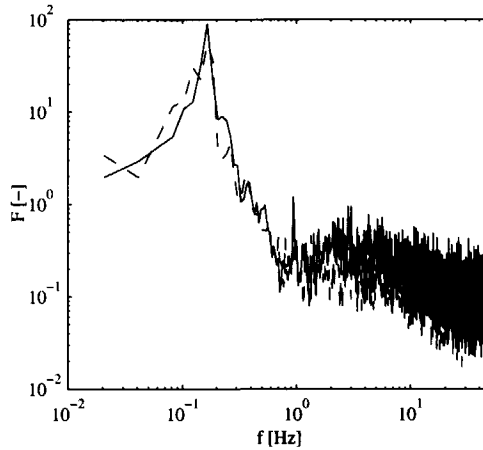
Figure 4.13: Spectral amplification function for experiment 1 (–) and experiment 2 (- -).

profile and only slightly on the turbulence levels themselves. This behavior is also found in the numerical simulations as well as in the experiments. However, non-linear effects played a role in the simulation with the highest level of inflow perturbations. Merging of vortices took place, resulting in a lower energy density levels and a lower peak frequency. A sensitivity study on the influence of these non-linear effects would be desirable to investigate the limitations of the linear approach.

This chapter was devoted to the influence of perturbations of the inflow on the development of the mixing layer and the coherent structures. It turned out that the mean flow was only slightly affected, but the intensity of the coherent structures were sensitive to amplitude differences of perturbations at the inflow. No attention was paid however to the origin of these perturbations and how these perturbations can be quantified. As it turned out that the development of the coherent structures is sensitive to these inflow perturbations, the depth-averaged motions have to be quantified beforehand in order to be able to model the development of the coherent structures in shallow shear flows properly. For that purpose, a three-dimensional simulation of a wide uniform channel flow is performed in Chapter 5. From these results, the depth-averaged motion can be extracted in order to quantify the large scale depth-averaged motion that has to be imposed in depth-averaged simulations.

Chapter 5

Simulation of large scale bottom turbulence

5.1 Introduction

In the previous chapter, it was concluded that perturbations have to be imposed in a depth-averaged simulation of a shallow mixing layer. Without perturbing the flow, no coherent structures are initiated and the spreading rate of the mixing layer is strongly underestimated.

The perturbations that have to be imposed, are expected to be the large scale components of the bottom turbulence. Although the bottom turbulence has a dominant length scale smaller than the water depth, motions with larger length scales may be present. Since these large scale motions are a result of the shear at the bottom, they should also be present in uniform channel flow. As input for the two-dimensional simulations the depth-averaged large scale bottom turbulence is required. Such data is however not available. Measurements on channel flows are generally performed in relatively narrow flumes and additionally it is difficult to measure such large scale motion as the energy content is small and the large scale motion as measured by point measurements will be contaminated by the aliasing effect (Tennekes & Lumley, 1972). Kim&Adrian (1999) showed that large scale motion is present in uniform channel flow. However, the data we need for determination of the imposed perturbations could not be extracted. Numerical simulations are generally performed for too small a flow domain, so that the large scale motion cannot develop due to the side boundaries, see for example Moser *et al.* (1999).

In this chapter the large scale bottom turbulence in a wide uniform channel flow is therefore studied with respect to amplitude and spectral distribution in order to quantify the perturbations that have to be imposed. To this end a fully three-dimensional Large Eddy Simulation is performed.

This chapter is built up as follows. In section 5.2 a fully three-dimensional Large Eddy Simulation (3D-LES) is described in which the bottom turbulence is resolved. The results of the 3D-LES are validated with results from a Direct Numerical Simulation (DNS) of a channel flow (Moser *et al.*, 1999). The computational domain of the 3D-LES was chosen large enough to quantify the large scale bottom turbulence. Two-dimensional power density spectra are used to determine the characteristics of the large scale bottom turbulence. In section 5.3 a kinematic simulation is used to mimic the large scale bottom turbulence, by its characteristics as obtained from the 3D-LES. This kinematic simulation is subsequently

implemented not only at the inflow condition but also as a perturbation term over the
full domain in the depth-averaged shallow water equations. The depth-averaged Transient
Reynolds Averaged Navier Stokes model with kinematic simulation (2D-TRANS+ks) thus
obtained, is used to simulate a uniform channel flow. Finally, conclusions are drawn in
section, 5.4.

5.2   Three-dimensional Large Eddy Simulation (3D-LES)

Large eddy simulation is used here as a research tool and is considered to be suitable
without modifications of the numerical scheme or subgrid model. Conventional numerical
procedures and subgrid scale models are therefore used which have been proved to be
applicable in channel flows. Details of various LES methods are described in textbooks by
for example Sagaut (1998) and Pope (2000).

5.2.1   Model description

The Navier-Stokes equations (NSe) form the basis of a large eddy simulation:

$$\frac{\partial u_i}{\partial x_i} = 0$$

$$\frac{\partial u_i}{\partial t} + u_i \frac{\partial u_j}{\partial x_i} = -\frac{1}{\rho}\frac{\partial p}{\partial x_i} + \nu \frac{\partial^2 u_j}{\partial x_i \partial x_j}$$

with $i = 1, 2, 3$ and $j = 1, 2, 3$. In LES the large scale motion is separated from the residual
motion by a spatial filter:

$$\tilde{u}_i(x_j, t) = \int G(r_j, x_j) u_i(x_j - r_j, t) \mathrm{d}r$$

Different filters G can be applied. In this thesis the top hat filter is used, which results in
the filtered NSe:

$$\frac{\partial \tilde{u}_i}{\partial x_i} = 0 \tag{5.1}$$

$$\frac{\partial \tilde{u}_i}{\partial t} + \tilde{u}_i \frac{\partial \tilde{u}_j}{\partial x_i} = -\frac{1}{\rho}\frac{\partial \tilde{p}}{\partial x_i} + \nu \frac{\partial^2 \tilde{u}_j}{\partial x_i \partial x_j} - \frac{\partial \tilde{\tau}_{ij}^{SGS}}{\partial x_j} \tag{5.2}$$

The influence of the residual motion on the filtered motion is expressed in the subgrid scale
(SGS) stress tensor τ_{ij}^{SGS}. Note the similarity with the Reynolds Averaged Navier Stokes
(RANS) equations (Equation 4.2 and 4.3). The SGS stress only represents the stress on the
subgrid scale, whereas the turbulence stresses in RANS represent all turbulent motions.
LES can now be carried out by integrating Equation 5.1 and 5.2 using a model for τ_{ij}^{SGS},
the subgrid model.

Often used subgrid models are the Smagorinsky model, the dynamic model and the mixed model (see for example Pope (2000), Sagaut (1998) and Germano (1991)). Good results are obtained for channel flow with the simple Smagorinsky model, which is therefore used. The Smagorinsky model is determined as:

$$\tau_{ij}^{SGS} = -\nu^{SGS}\tilde{S}_{ij}$$

with

$$\nu^{SGS} = (C_s\Delta)^2\,\tilde{S}$$

with $\tilde{S} = (2\tilde{S}_{ij}\tilde{S}_{ij})^{1/2}$ the rate of strain, C_s the Smagorinsky coefficient, and Δ the mesh size. A value of $C_s = 0.065$ gave optimal results for channel flow (Moin & Kim, 1982) and is used here.

In order to reduce the number of grid cells a wall function is applied to model the viscous sublayer. Therefore an extra shear stress τ_w is added to the momentum balance of the first cell counting from the bottom. Different models have been developed to represent the shear stress at the wall τ_w (Pope, 2000; Sagaut, 1998; Piomelli *et al.*, 1989). Here the Schumann-Grötzbach model (Schumann, 1975) is used:

$$\tau_{w_{uu}} = \frac{u(x,y,z_1)}{\langle u(x,y,z_1)\rangle}\langle\tau_w\rangle \tag{5.3}$$

$$\tau_{w_{vw}} = \frac{v(x,y,z_1)}{\langle u(x,y,z_1)\rangle}\langle\tau_w\rangle \tag{5.4}$$

with z_1 being the first grid point from the wall. The brackets denote the long time averaging. The ratio between the instantaneous velocity and stress is assumed to be equal to the ratio of the time mean velocity and stress. The stress and velocity are assumed to be in phase. The mean velocity $\langle u\rangle$ is calculated and the stress τ_w is determined using the log law:

$$\frac{\overline{u}(z_1)}{u_*} = \left(\frac{1}{\kappa}\ln\frac{z_1 u_*}{\nu} + 5.5\right)$$

$$\tau_w = \rho u_*^2 \tag{5.5}$$

The above described set of equations is solved with a large eddy simulation model developed at the Laboratory for Aero and Hydrodynamics at Delft University of Technology. Details of the numerics can be found in Eggels (1994).

5.2.2   Flow conditions

In order to check the proper performance of the code with the above described bottom boundary condition, the flow conditions of the channel flow of Moser, Kim and Mansour (1999)[1] (MKM) are adopted. MKM performed a direct numerical simulation (DNS) for a

---

[1]An extensive data set of the MKM simulations can be found at www.tam.uiuc.edu/Faculty/Moser/channel.

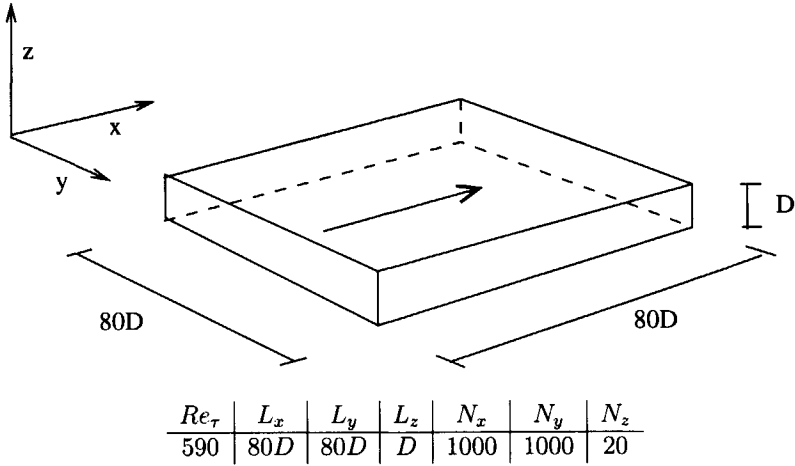| Re_τ	L_x	L_y	L_z	N_x	N_y	N_z
590	$80D$	$80D$	D	1000	1000	20

Figure 5.1: Sketch of the computational domain (top), and parameter settings (bottom).

relatively high Reynolds number, resulting in a large number of grid points on a small domain. However, the length and the width of the domain in this study are strongly increased in order to be able to reveal the large scale depth-averaged motion. As a consequence the resolution of the grid is decreased. A sketch of the domain and the coordinates used is given in figure 5.1.

A uniform channel flow is characterized by the Reynolds number $Re_* = u_* D/\nu$, where u_* is the friction velocity, D the depth of the flow and ν the viscosity. All velocities are made dimensionless with the friction velocity. The simulation for $Re_* = 590$ is chosen for comparison with MKM. The number of cells in the direction perpendicular to the bottom (z) is set at $N_z = 20$, yielding acceptable results with a relatively coarse grid. The grid size in streamwise direction and transverse direction are stretched by a factor 1.6 with respect to the vertical grid size. A grid of $20 \ 10^6$ cells could be implemented on a computer cluster with 20 active nodes, allowing a domain size of $L_x \times L_y = 80D \times 80D$.

Periodic boundary conditions were imposed on the inflow, outflow and side walls. Where MKM simulated a closed channel with a no-slip rigid lid upper boundary condition, an open channel with a free-slip rigid lid upper boundary condition is simulated here. A proper comparison is still possible when comparing the open channel with only half the closed channel.

The initial conditions were created by perturbing the log profile with random fluctuations with an intensity of $\sqrt{u'^2(t_0)} = u_*$. This initial condition is needed to start up the generation of coherent structures. The data presented are gathered from the moment a stationary flow is obtained and the wall shear stress balances the mean pressure gradient.
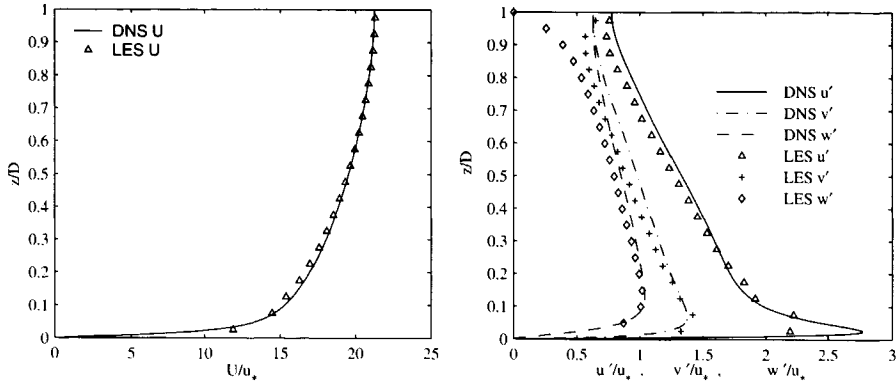
Figure 5.2: Profiles of the mean velocities (left) and the turbulence intensities (right), relative to the friction velocity. The DNS results are obtained from Moser et al. (1999)

5.2.3 Validation with MKM

The mean velocity profile calculated with 3D-LES is plotted in figure 5.2 together with the results obtained with the DNS by MKM. The differences between the LES and DNS are very small. As can be expected from a simulation with insufficient resolution, a small deviation from the DNS is found close to the bottom. The turbulence intensities are also plotted in figure 5.2. The maximum intensities near the bottom are fairly well represented, despite the low resolution. The low intensities of the vertical fluctuations in the LES-results close to the water surface are a consequence of the rigid lid at the surface, whereas this elevation from the bottom equals the center of the channel in the DNS, allowing vertical velocity fluctuations.

In view of our application it should also be established how the turbulent motions are distributed over the wavenumber range. The power density spectra of the LES and the DNS are therefore compared. The range in which the results can be compared is however restricted. On the one hand, the horizontal dimensions of the domain of the DNS are limiting. The minimum wavenumber should be at least larger than the value related to the domain size $kD_{min,DNS} = 0.16$. On the other hand the maximum wavenumber is limited by the resolution of the LES. The maximum value should be at least smaller than the Nyquist wavenumber related to the gridsize $kD_{max,LES} = 6.1$. The power density spectra obtained from the streamwise and the transverse velocity at middepth are plotted in Figure 5.3. The velocities were made dimensionless with the friction velocity and the wavenumbers with the water depth. The normalized spectra of the 3D-LES and the DNS collapse in the range $0.3 < kD < 3$. Domain-size effects play a role on the low wavenumber side and numerical effects on the high wavenumber side, reducing the range where the data should collaps. The overall agreement with the DNS is concluded to be sufficient. The resolution and the wall function used in the 3D-LES model are therefore concluded to be suitable for
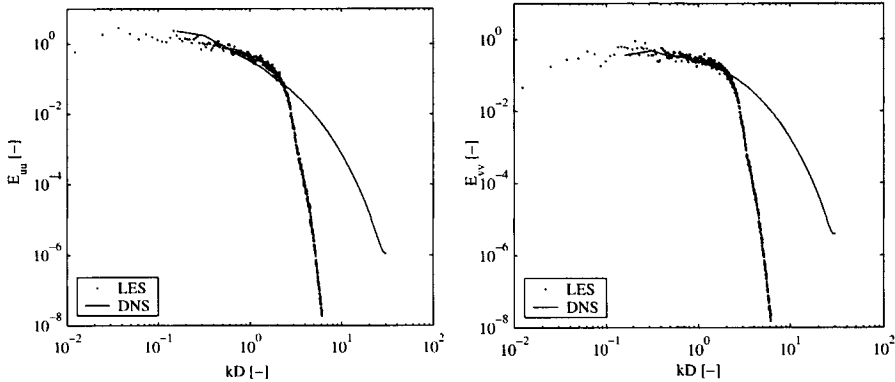
Figure 5.3: Dimensionless power density spectra of the streamwise (left) and transverse velocity (right) at $z = 0.5D$. The DNS results are obtained from Moser et al. (1999).

the determination of the large scale depth-averaged motion.

5.2.4 Large scale motion

In the wavenumber range where a comparison of the DNS and the 3D-LES is meaningful, the LES results are in fairly good agreement with the DNS results. The validated 3D-LES results can now be used for the determination of the characteristics of the large scale depth-averaged motion. The perturbations that are to be imposed in the depth-averaged TRANS simulations should have the same characteristics. These characteristics are evaluated by means of the two-dimensional energy density spectra.

In order to determine the two-dimensional velocity spectra, instantaneous velocity maps are first averaged over the depth. Two-dimensional energy density spectra are subsequently determined, providing the energy distribution over the wave number field k_x, k_y. Spectra are obtained from 100 statistically independent velocity maps. Contour plots of the averaged energy density spectra are presented for the streamwise and the transverse velocity in the figures 5.4a and b. The maximum value for the spectrum of the streamwise fluctuations is found for $k_x D \simeq 0$ and $k_y D = 0.35$. Such a spectrum is associated with streamwise elongated patches of low and high streamwise velocities. (An instantaneous velocity map is shown in figure 5.6, further in this chapter.) The energy density levels in the spectrum of the transverse fluctuations are significantly lower than those in the spectrum of the streamwise fluctuations. A ridge is found about the line $k_x D = k_y D$ with a maximum at $k_x D = k_y D \simeq 0.15$. The symmetry along the line $k_x D = k_y D$ indicates that the pattern of transverse fluctuations is not elongated in streamwise direction as it is the case for the streamwise flow pattern, see Figure 5.6.
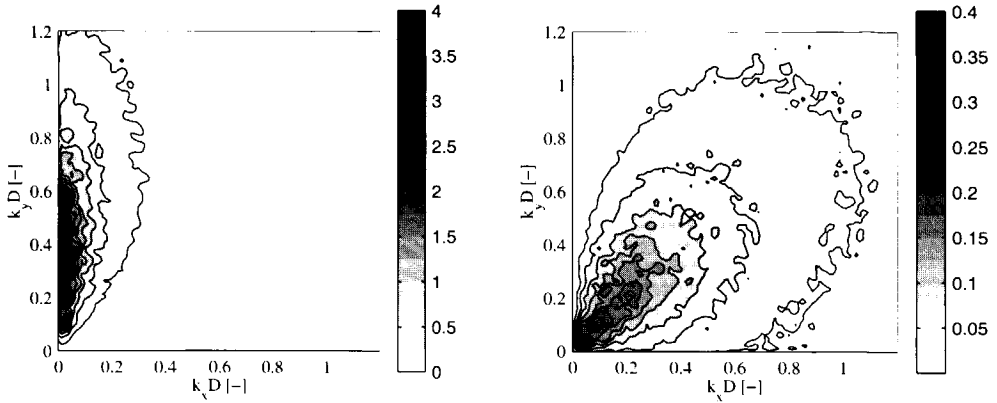
Figure 5.4: Two-dimensional energy density spectra of the depth-averaged streamwise (left) and transverse (right) velocity fluctuations .

5.3 Kinematic simulation

In the previous section the distribution of the depth-averaged turbulent kinetic energy over the wavenumber field has been determined. In this section, it is attempted to mimic this depth-averaged large scale motion by means of kinematic simulation. Mimicking turbulent motion by means of kinematic simulation is for example described by Fung et al. (1992). In such a simulation, the instantaneous turbulent velocity field is simulated by the summation of Fourier modes:

$$u_{ks}(x, y) = \frac{1}{N} \sum_{n=1}^{n=N} \hat{u}^n \sin \left(k_x^n x + k_y^n y + \phi^n \right) \qquad (5.6)$$

$$v_{ks}(x, y) = \frac{1}{N} \sum_{n=1}^{n=N} \hat{v}^n \sin \left(k_x^n x + k_y^n y + \phi^n \right) \qquad (5.7)$$

with a random phase ϕ. The amplitudes $\hat{u}$ and $\hat{v}$ have to be prescribed such that the corresponding energy density distribution mimicks the spectra of the three-dimensional LES. Four different properties are distinguished in this respect. The first property of the large scale motion is *continuity*. This demand couples the spectra of the streamwise and transverse fluctuations. The continuity equation should be fulfilled by the imposed velocity fluctuations. The second property is *anisotropy* of the streamwise velocity. The elongation of the streamwise velocity in the streamwise direction has to be reproduced, see figure 5.4 (left). However, this elongation should not be reflected in the transverse velocity, see figure 5.4 (right). As a consequence of the anisotropy and the continuity, the energy density of the streamwise velocity is higher than that of the transverse velocity. The anisotropy term not only reflects the energy distribution, but also the ratio between the energy of the streamwise and transverse fluctuations. The factor representing the anisotropy is proposed

to scale with k_y and is made dimensionless with k. Elongated vortices $(k_y > k_x)$ will therefore have higher energy density levels. The third property is *velocity scaling*. The fluctuations are related to the friction velocity. Higher energy density levels should be found for rougher bottoms and/or higher mean streamwise velocities. The fourth property is *length scaling*. The wavenumbers are made dimensionless with the depth. The associated factor is chosen such that the spectra fit the data well. Appropriate expressions have been postulated reflecting these four properties, leading to the following total expressions for the amplitudes:

$$\hat{u}(k_x^n, k_y^n) = \underbrace{\alpha u_*}_{\text{velocity scaling}} \underbrace{\lambda |k^n| D \exp\left(-\lambda |k^n| D\right)}_{\text{length scaling}} \underbrace{\left(\frac{k_y^n}{|k^n|}\right)^\beta}_{\text{anisotropy}} \underbrace{\frac{k_y}{|k^n|}}_{\text{continuity}} \tag{5.8}$$

$$\hat{v}(k_x^n, k_y^n) = - \underbrace{\alpha u_*}_{\text{velocity scaling}} \underbrace{\lambda |k^n| D \exp\left(-\lambda |k^n| D\right)}_{\text{length scaling}} \underbrace{\left(\frac{k_y^n}{|k^n|}\right)^\beta}_{\text{anisotropy}} \underbrace{\frac{k_x}{|k^n|}}_{\text{continuity}} \tag{5.9}$$

$$|k| = \sqrt{k_x^2 + k_y^2}$$

in which α, β and λ have to be determined from the three-dimensional LES. Fitting Equation 5.8 and 5.9 to the results of the depth-averaged LES resulted in optimum values $\alpha = 1.3$, $\beta = 3.0$ and $\lambda = 0.3$. The corresponding two-dimensional power density spectra for the streamwise and transverse fluctuations are plotted in figure 5.5. The main features of the parameterized spectra are in fair agreement with those of the depth-averaged three-dimensional LES (Figure 5.4), except that the spectrum E_{vv} does not have its ridge along
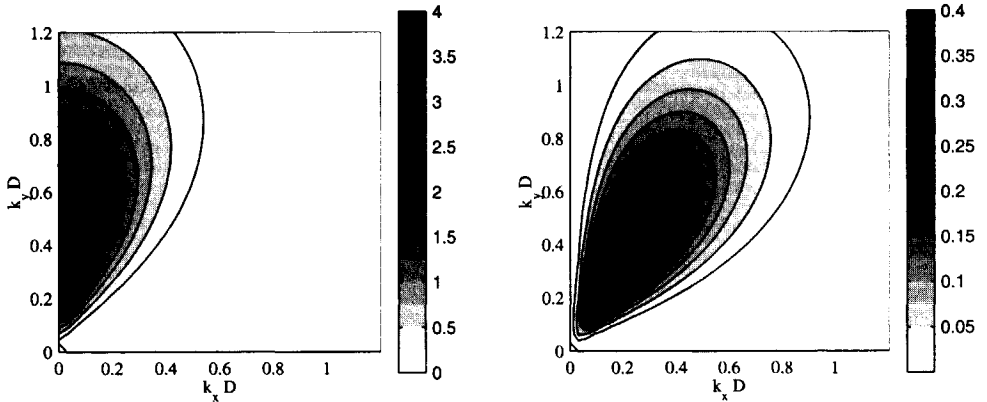

Figure 5.5: Two-dimensional energy density spectra of the depth-averaged streamwise (left) and transverse (right) velocity fluctuations, as described by Equation 5.8 and 5.9.

the line $k_y = k_x$ but on the line $k_y = 1.4k_x$. The anisotropy parameter β is however chosen such that the ratio between the energy of the streamwise and transverse fluctuations is correctly reproduced. More sophisticated expressions for the spectra would possibly lead to a better approximation. However, as will be shown below, good results are obtained with the here proposed expression.

Substitution of the so obtained amplitudes in the kinematic simulation, Equation 5.6 and 5.7, results in the perturbations that will be imposed in the two-dimensional simulations.

5.4 Transient RANS with kinematic simulation (2D-TRANS+ks)

5.4.1 Implementation of kinematic simulation in the TRANS model

After defining the large scale (non-resolved) motion using a kinematic simulation, it is implemented in the depth-averaged model (2D-TRANS). In Chapter 4, the perturbations were imposed only at the inflow boundary. For a uniform channel flow, this would lead to the dissipation of these inflow perturbations. As there is no source like a transverse gradient of the streamwise velocity to sustain the perturbations, all energy is dissipated due to the bottom friction and the eddy viscosity. Naturally, this is not the case for a three-dimensional large eddy simulation of a uniform channel flow due to the vertical velocity gradient. This channel flow turbulence is typically three-dimensional with length scales in the order of the water depth, but it appears to have also larger scale components, resulting in residual turbulent fluctuations after depth-averaging. Such turbulent motions can principally not be reproduced by a depth-averaged model, as the vertical gradient of the streamwise velocity is absent. In order to account for these depth-averaged motions, extra force terms have to be inserted in the shallow water equations over the entire domain. Such terms are for example implemented by Chasnov (1991) and Leith (1990) for three-dimensional Large Eddy Simulations. They aimed to mimic the effects of the non-linear interactions of the small scale non-resolved motion on the large scale resolved motion by adding random fluctuations. In the case of shallow water flow, we aim to mimic the depth-averaged large scale motions that were filtered out by the depth-averaging operator.

The additional terms should be implemented in the momentum equations. For a fully developed uniform channel flow, the fluctuating force should compensate for the dissipative influence of the bottom friction and the eddy viscosity.

To determine the force representing the large scale bottom turbulence we start with the shallow water equations for the velocity fluctuations in a uniform channel flow, see also 3.20 and 3.21:

$$\frac{\partial u}{\partial t} + U\frac{\partial u}{\partial x} = -\frac{\partial p}{\partial x} - \frac{2c_f U}{D}u + \nu_t\left(\frac{\partial^2 u}{\partial x^2} + \frac{\partial^2 u}{\partial y^2}\right) \tag{5.10}$$

$$\frac{\partial v}{\partial t} + U\frac{\partial v}{\partial x} = -\frac{\partial p}{\partial y} - \frac{c_f U}{D}v + \nu_t\left(\frac{\partial^2 v}{\partial x^2} + \frac{\partial^2 v}{\partial y^2}\right) \tag{5.11}$$

On the r.h.s of the equations, the dissipative bottom friction and viscosity terms can be recognized. They consist of a fluctuating component and a mean component. The proposed perturbation force is defined here in the same form as the bottom friction and the viscosity term, with opposite sign. The velocity fluctuations in these terms are replaced by the fluctuations obtained from the kinematic simulation. The perturbation forcing terms to be inserted into the r.h.s of Equation 5.10 and 5.11 are then:

$$F_x = +\frac{2c_f U}{D}u_{ks} - \nu_t\left(\frac{\partial^2 u_{ks}}{\partial x^2} + \frac{\partial^2 u_{ks}}{\partial y^2}\right)$$

$$F_y = +\frac{c_f U}{D}v_{ks} - \nu_t\left(\frac{\partial^2 v_{ks}}{\partial x^2} + \frac{\partial^2 v_{ks}}{\partial y^2}\right)$$

These perturbation forces are implemented in the depth-averaged shallow water equations, leading to

$$\frac{\partial u}{\partial t} + u\frac{\partial u}{\partial x} + v\frac{\partial u}{\partial y} = -\frac{1}{\rho}\frac{\partial \tilde{p}}{\partial x} - \frac{c_f}{D}u\sqrt{u^2 + v^2} + \nu_t\nabla^2 u + \underbrace{\frac{2c_f U}{D}u_{ks} - \nu_t\nabla^2 u_{ks}}_{\text{kinematic simulation}} \tag{5.12}$$

$$\frac{\partial v}{\partial t} + u\frac{\partial v}{\partial x} + v\frac{\partial v}{\partial y} = -\frac{1}{\rho}\frac{\partial \tilde{p}}{\partial y} - \frac{c_f}{D}v\sqrt{u^2 + v^2} + \nu_t\nabla^2 v + \underbrace{\frac{c_f U}{D}v_{ks} - \nu_t\nabla^2 v_{ks}}_{\text{kinematic simulation}} \tag{5.13}$$

In section 5.3 the kinematic simulation has only been described as a spatial velocity field. For the proposed implementation time dependency is needed. The classical way of implementation of the time dependency is by replacing the coordinates x and y by $x - \int_0^t u\,\mathrm{d}t$ and $y - \int_0^t v\,\mathrm{d}t$. This can be interpreted as a turbulent flow field that is entering the domain from the inflow boundary and that is advected mainly with the mean streamwise velocity. As the fluctuations are small, the influence of the fluctuations on the celerity is small. Such an implementation implies however that perturbations are only generated at the inflow, but the perturbations we intend to mimic are generated locally. A physically more sound method would be to make the amplitude of the perturbations time dependent. The transient kinematic simulation then becomes:

$$u_{ks}(x, y, t) = \frac{1}{N}\sum_{n=1}^{n=N}\sqrt{2}\sin(\int_0^t (k_x U + k_y V)\mathrm{d}t + \theta^n)\hat{u}^n\sin\left(k_x^n x + k_y^n y + \phi^n\right) \tag{5.14}$$

$$v_{ks}(x, y, t) = \frac{1}{N}\sum_{n=1}^{n=N}\sqrt{2}\sin(\int_0^t (k_x U + k_y V)\mathrm{d}t + \theta^n)\hat{v}^n\sin\left(k_x^n x + k_y^n y + \phi^n\right) \tag{5.15}$$

The amplitude varies depending on the local mean velocities and the wavelengths of the mode. The factor $\sqrt{2}$ is needed to keep the total kinetic energy correct.

The term 2D-TRANS+ks is used from here on to refer to the depth-averaged TRANS model with kinematic simulation.

5.4.2   Comparison with 3D-LES

The channel flow as simulated with 3D-LES in the first part of this chapter is simulated with the two-dimensional model 2D-TRANS+ks as described above. The mesh sizes are chosen as $\Delta x = \Delta y = D/3$, as it is aimed to resolve the scales larger than about two times the water depth. The computational domain then consists of $N_x \times N_y = 240 \times 240$ grid points. In order to compare the velocities obtained from the 2D-TRANS+ks with the depth-averaged velocities of the 3D-LES a low-pass spatial filter is applied. A cut-off $k_c\Delta = 2D$ is used as the larger scales are intended to be simulated. Instantaneous filtered streamwise velocity fields are plotted in Figure 5.6 as obtained from the 3D-LES (a) and from the 2D-TRANS+ks (b). As shown the elongated patches of streamwise velocity are fairly well reproduced. Also the instantaneous filtered transverse velocity fields are plotted as obtained from the 3D-LES (c) and from the 2D-TRANS+ks (d). The isotropic pattern is simulated. The fair agreement between the 3D-LES and the 2D-TRANS+ks is partly a result of the imposed spectrum.

5.5   Summary and conclusions

The large scale motion in a wide uniform channel flow is simulated. First a three-dimensional large eddy simulation is performed, in which the bottom induced turbulence is resolved. The vertical profiles of the mean streamwise velocity and the turbulence intensities are in good agreement in overlapping wavenumbers with the results obtained from a DNS (Moser *et al.*, 1999). Also the power density spectra of the fluctuations at half the depth showed good agreement. Two-dimensional spectra of the depth-averaged motion are determined representing the energy distribution in wave number space. These spectra are parameterized and implemented in a kinematic simulation representing the large scale bottom turbulence. The perturbations obtained via kinematic simulation are implemented in the inflow condition and as perturbation forces in the shallow water momentum equations, leading to the 2D-TRANS+ks model (Transient Reynolds averaged Navier Stokes with kinematic simulation). This 2D-TRANS+ks model is applied to a uniform channel flow. The main features of the large scale depth-averaged bottom turbulence could be reproduced properly.
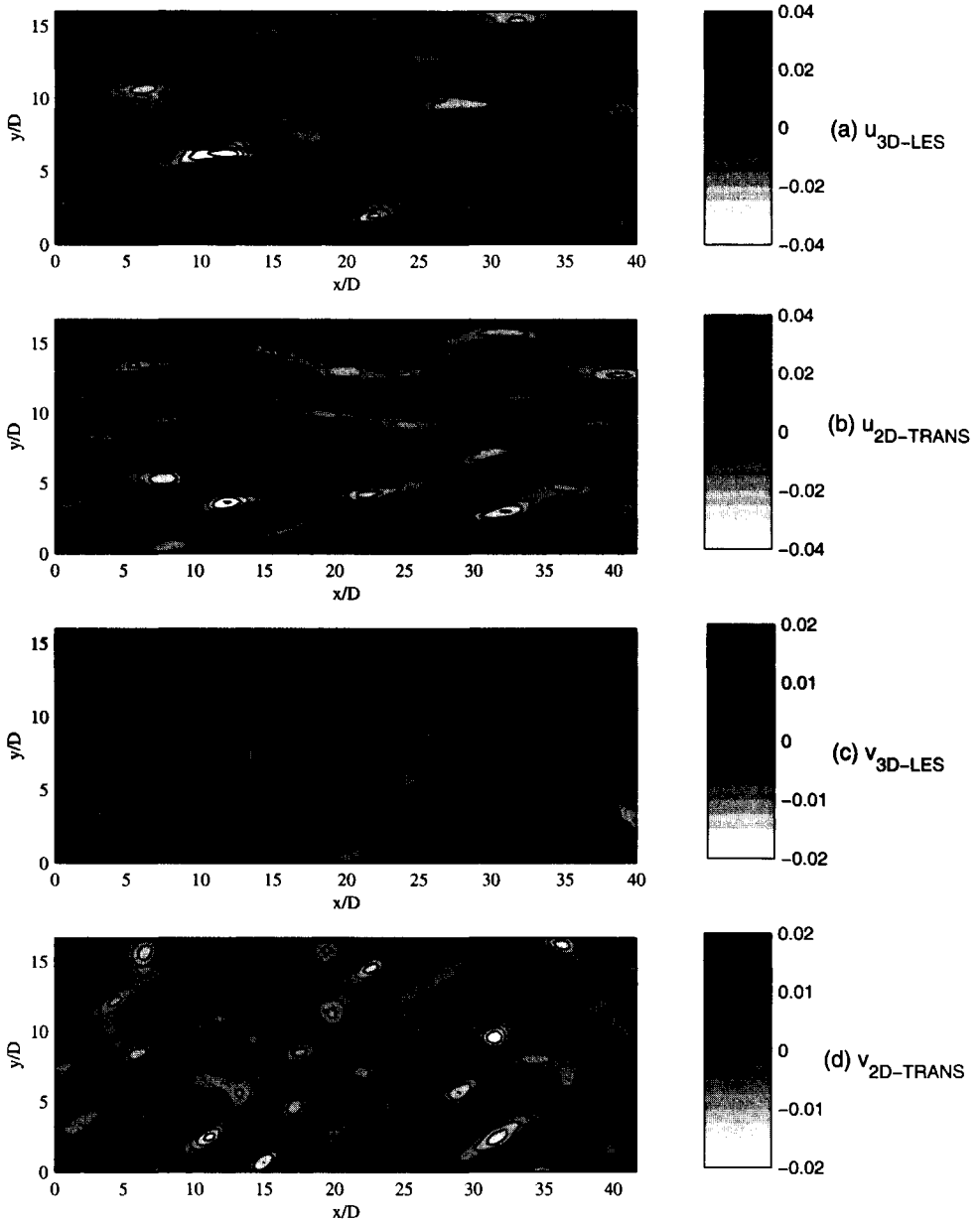
Figure 5.6: Contours of the instantaneous depth-averaged streamwise (first and second) and transverse velocity fluctuations (third and fourth) obtained from 3D-LES (first and third) and 2D-TRANS+ks (second and fourth). The velocities are scaled with the mean streamwise velocity. Only a part of the total flow domain is plotted.

Chapter 6

Application of 2D-TRANS+ks

In this chapter the model 2D-TRANS+ks is applied to shallow shear flows. The model was tested in the former chapter for a uniform channel flow, without streamwise and lateral velocity gradients. These gradients are however present in shear flows. The performance of the kinematic simulation is therefore first tested for flows with velocity gradients. After a slight modification of the 2D-TRANS+ks model, two different shear flow configurations are simulated. First, the shallow mixing layers, Case 42 and Case 67 as described in Chapter 2 are computed. A comparison between the simulations and the measurements is made, based on the statistical properties, the spectral distribution of the energy and the conditionally averaged vortices. Second, a compound channel flow with lateral roughness variation is simulated. This configuration is chosen to emphasize the need of imposing perturbations over the full domain.

Finally, the applicability of the 2D-TRANS+ks model for engineering purposes is discussed.

6.1 Temporal dependency of kinematic simulation

The shallow shear flows discussed in this chapter differ from a uniform flow with respect to the presence of streamwise and transverse velocity gradients. From testing the model for flows with velocity gradients, it turned out that these gradients have distorting effects on the time evolution of the kinematic simulation. This can be understood as follows. The base structure of the kinematic simulation equation (Equation 5.8) can be simplified to:

$$u_{ks}(x,t) = \hat{u}\sin(kU(x)t)\sin(kx) \tag{6.1}$$

The first sine term denotes the temporal variation of the amplitude and is affected by the local advection velocity. The second sine term denotes the spatial variation. In case of a spatially varying velocity $U(x)$, the first sine term becomes spatially dependent as well as the second sine term. This can cause spurious beat effects, resulting in an unacceptable distortion of the acceleration field that is to be imposed.

In order to avoid the beat effects, a constant mean streamwise velocity is chosen in the expression for the temporal evolution of the amplitude. It is noted that the amplitude $\hat{u}$ remains dependent on the local velocity, which varies in time and space. The perturbations

are then defined as:

$$u_{ks}(x,y,t) = \frac{1}{N}\sum_{n=1}^{n=N}\sqrt{2}\sin(\int_0^t (k_x\mathcal{U}+k_y\mathcal{V})\mathrm{d}t + \theta^n)\hat{u}^n \sin\left(k_x^n x + k_y^n y + \phi^n\right) \qquad (6.2)$$

$$v_{ks}(x,y,t) = \frac{1}{N}\sum_{n=1}^{n=N}\sqrt{2}\sin(\int_0^t (k_x\mathcal{U}+k_y\mathcal{V})\mathrm{d}t + \theta^n)\hat{v}^n \sin\left(k_x^n x + k_y^n y + \phi^n\right) \qquad (6.3)$$

with constant velocities $\mathcal{U}$ and $\mathcal{V}$. This modified expression for the kinematic simulation has the advantage that beat effects are excluded, but the disadvantage is that the description is less generally applicable and physically realistic.

6.2 Shallow mixing layer

6.2.1 Simulation set-up

Computations are performed to simulate the shallow mixing layer flows of Case 42 and Case 67, see Chapter 2. Following the arguments as used in Chapter 4, the mesh size is chosen to approximately one third of the water depth: $\Delta x = 1.5$cm for Case 42 and $\Delta x = 2$cm for Case 67. As measurements are available up to the downstream position $x = 10$m, the length of the flow domain is set to $L = 12$m. The duration of the simulations is set to $T = 15$ minutes for Case 42 and $T = 20$ minutes for Case 67. This is three respectively four times the duration of the measurements.

The parameter settings for the kinematic simulation are taken from Chapter 5: $\alpha = 1.3$, $\beta = 3.0$ and $\lambda = 0.3$. As described above, the velocities $\mathcal{U}$ and $\mathcal{V}$ have to be set as well. These are set to $\mathcal{U} = U_c = (U_1 + U_2)/2$ and $\mathcal{V} = 0$.

6.2.2 Statistical analysis

The transverse profiles of the mean streamwise velocity at different downstream positions are plotted in figure 6.1a for Case 42 and in figure 6.2a for Case 67. There is a good agreement between the simulations and the measurements for both cases. The mean features of the downstream development of the mixing layer are captured, like the decreasing velocity difference, the growth of the mixing layer width and the shift of the mixing layer to the low velocity side.

The turbulence intensities u' and v' and the Reynolds stresses of the numerical simulations and the measurements are filtered in time for a proper comparison, see Section 2.3. The turbulence intensities u' are plotted in Figure 6.1b and Figure 6.2b. The simulated values are generally smaller than the measured values, not only outside the mixing region, but also in the mixing zone. The significant peak as found in the measurements is much less pronounced in the simulations. The transverse turbulence intensities v' are plotted in Figure 6.1c and Figure 6.2c. Outside the mixing region, the simulated results are smaller than the measured ones. In the mixing region the transverse intensities are overestimated.

Figure 6.1: Profiles of the mean velocity U, the intensity of the streamwise fluctuations u', the intensity of the transverse fluctuations v' and the Reynolds stress $\overline{u'v'}$ for Case 42. The dots represent the measurements and the solid line the simulation.
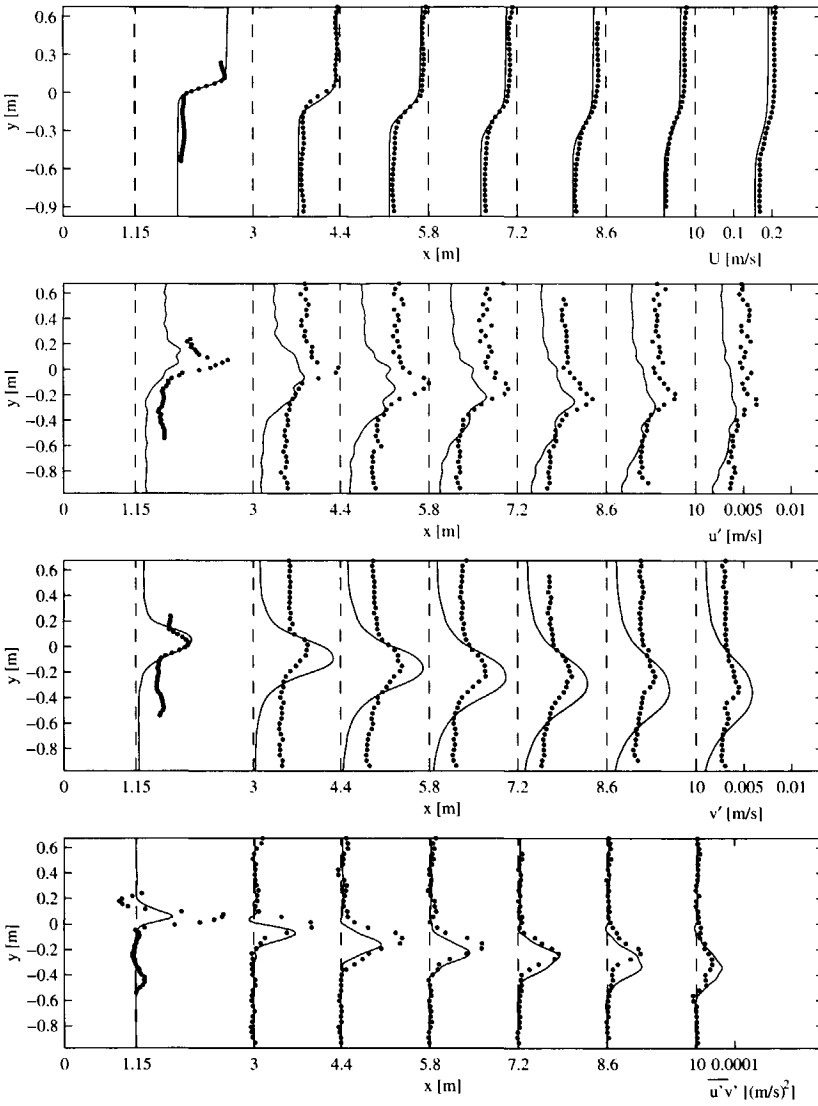
Figure 6.2: Profiles of the mean velocity U, the intensity of the streamwise fluctuations u', the intensity of the transverse fluctuations v' and the Reynolds stress $\overline{u'v'}$ for Case 67. The dots represent the measurements and the solid line the simulation.
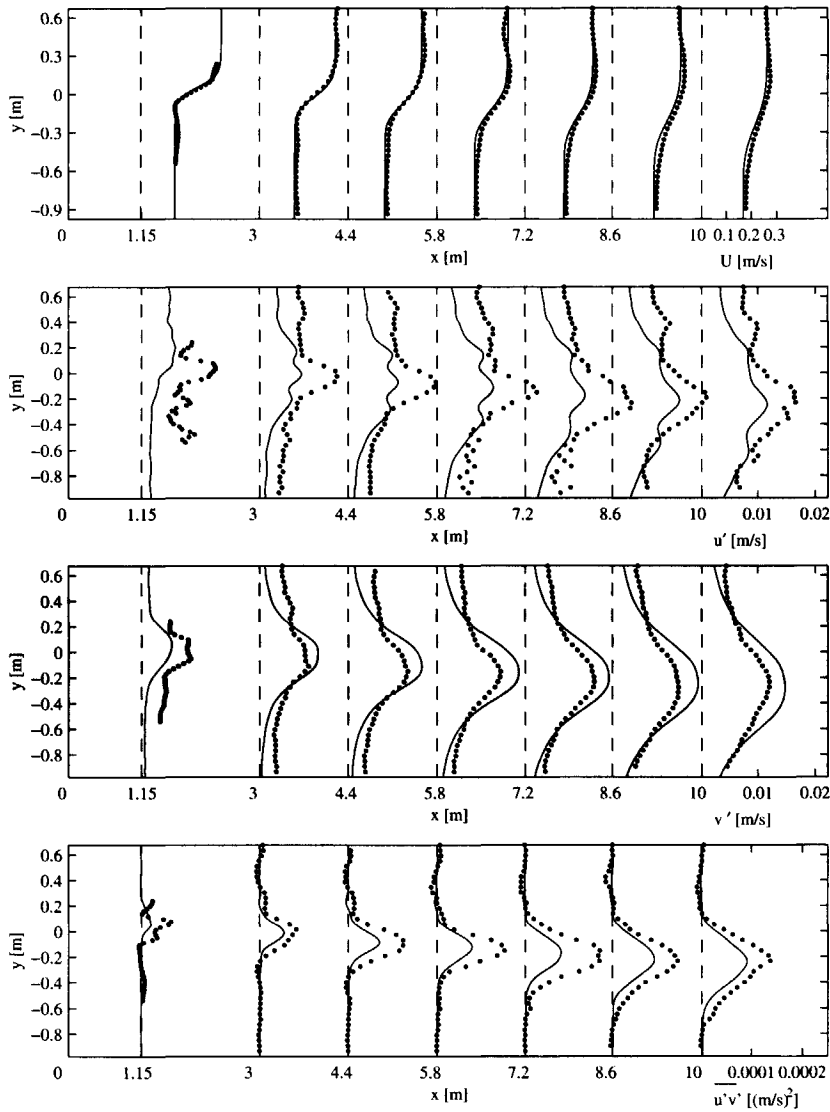
The Reynolds stresses are plotted in Figure 6.1d and Figure 6.2d. A fair agreement is found for Case 42, but the Reynolds stresses for Case 67 are underestimated, especially when considering the fact that free-surface data are compared with depth-averaged data.

From the above comparison it can be concluded that especially for the turbulence intensities discrepancies are found between the simulations and the measurements. These discrepancies will be discussed further. The simulations are essentially two-dimensional; the plotted velocities represent the depth-averaged motion. This is different from the quasi two-dimensional motion of the measurements from which only the surface velocity is measured. The measurements represent the 'footprint' of the quasi two-dimensional flow on the surface velocity. Some effects of the three-dimensional character on the two-dimensional flow are taken into account in the simulations, by the bottom shear stress and the turbulence viscosity. Two effects that are reflected in the measurements will however not be found in the two-dimensional simulations.

The first effect that is not taken into account is the dispersion due to the vertical gradient in streamwise velocity. The part of a horizontal eddy close to the water surface is advected faster than the part at the bottom, resulting in elongation of the vortex. Elongation of vortices leads to convergence of the streamlines on the sides of the vortex and to divergence of the streamlines at the front and the back, see Figure 2.9. Relatively high intensities of the streamwise fluctuations and relatively low intensities of the transverse fluctuations were therefore found in the experiments. The absence of the vertical gradient in the simulations results in less elongated, more isotropic vortices. The streamwise fluctuations will therefore be underestimated and the transverse fluctuations overestimated in two-dimensional simulations.

The second effect of the two-dimensional approach in the simulations is that secondary circulations which have their axes in the horizontal plane are filtered out. These circulations will however be reflected in the velocity fluctuations at the surface as measured by PTV. This has the effect that the measured turbulence intensities will be higher than the simulated ones.

Although these two effects might explain some of the discrepancies found between the measurements and the simulations, a closer look at the distribution of the energy over the different scales is desirable. To that end, spectral analysis is performed in the next section.

6.2.3   Spectral analysis

The energy density spectra of the transverse fluctuations at the center of the mixing layer are plotted in Figure 6.3 for Case 42 and for Case 67 for three different downstream locations. As discussed in Chapter 2, a peak is found in the spectra, associated with the coherent structures. This peak is moving to the low frequency side of the spectra with increasing distance downstream, in accordance with a growth in size. This shift is reasonably well simulated. If we consider for example Case 67, $x = 5.6$m, the measured peak frequency is $f = 0.18$Hz and the simulated one $f = 0.20$Hz. The peak frequencies are fairly well represented. The magnitudes of the peaks are overestimated, but on both sides of the peak, the energy density is strongly underestimated. For both cases, the energy
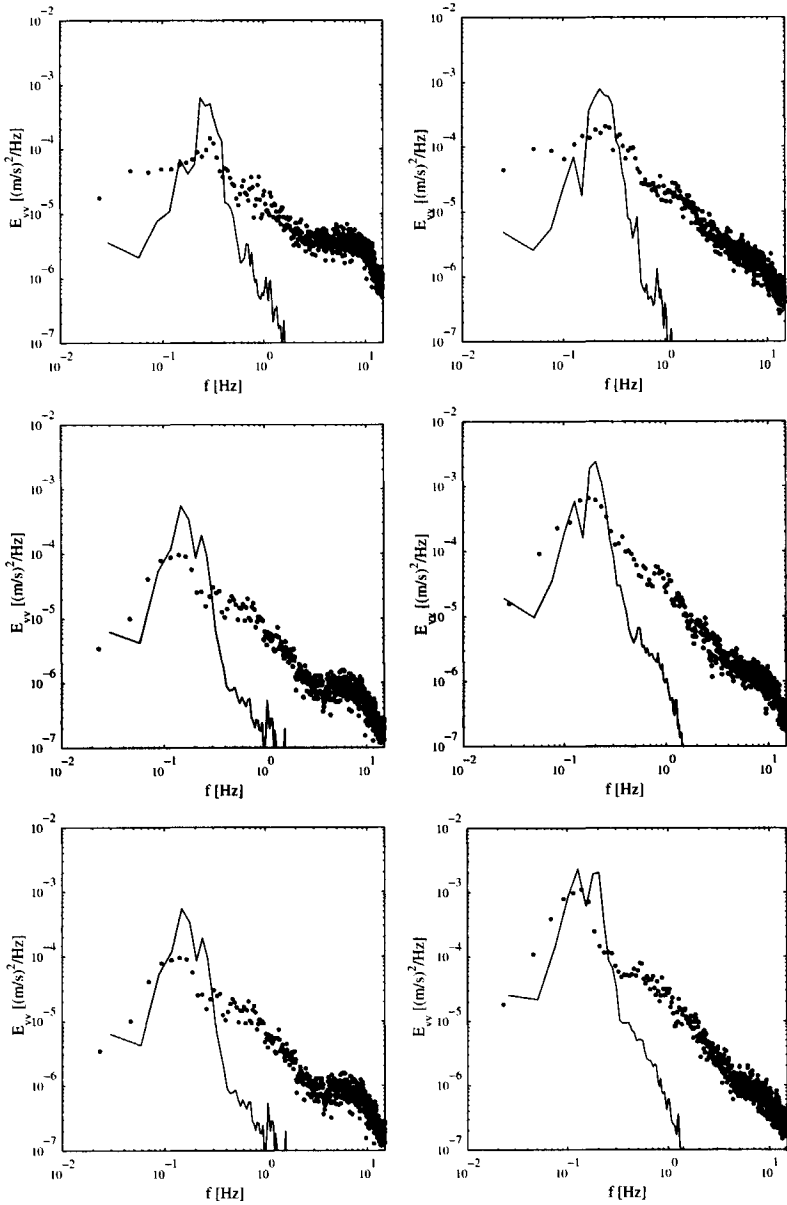
Figure 6.3: Energy density spectra of the transverse velocity fluctuations at the positions $x = 3$m (top), $x = 5.8$m (middle) and $x = 8.6$m (bottom) for Case 42 (left) and Case 67 (right). The dots represent the measurements and the solid lines the simulations.

density is concentrated in too narrow a frequency range relative to the measurements. One of the reasons for this narrow band might be that the simulations represent the depth-averaged energy density, whereas the measured spectra represent the energy density of the surface velocity fluctuations. Possible secondary circulations as mentioned in the former section are not taken into account in the simulations, but might have their footprints in the observed energy density spectra.

The developments of the peak values are similar to the developments as found in the measurements: the peak values decrease for Case 42 and increase for Case 67.

In Figure 6.4, the energy density spectra of the streamwise fluctuations and the cross spectra between the streamwise and transverse fluctuations are plotted for both cases for the downstream position $x = 5.6$m. The energy density levels of the streamwise fluctuations as found in the simulations generally underestimate the measured levels. The peak frequencies and peak values are fairly well represented. This is also the case for the cross spectra. Like in the spectra of the transverse fluctuations, the simulated energy is concentrated in a narrower frequency range than for the measured spectra.

It is concluded that the trends as found in the measured power density spectra are well reproduced by the simulation. Peaks are found for which the associated frequencies and peak values are fairly close to the measured ones. A detailed analysis of the three-dimensional motion is required for a proper understanding of the discrepancies found between the measurements and the simulations, as both the simulations and the measurements are different 2D-projections of the full three-dimensional motion.

6.2.4 Coherent structures

In Chapter 2, conditionally averaged vortices have been determined from the measurements of Case 67 at the downstream positions: $x = 3.0$m and $x = 8.6$m. The same pattern recognition technique as described in Section 2.5 is applied here to the numerical results for the same two downstream positions.

The vector fields, the transverse velocity contours, the vorticity contours and the Weiss-function contours of the conditionally averaged vortices are plotted in Figure 6.5 for $x = 3.0$m and in Figure 6.6 for $x = 8.6$m. For a comparison with the experimental data the results presented in Figure 2.12 and Figure 2.13 can be used. Qualitatively, the simulated vortices are in good agreement with the ones found in the experiments. The orientation of the vortex is for example fairly well reproduced. The amplitudes of the transverse velocity are somewhat overestimated, the vorticity is in good agreement and the values for the Weiss function are overestimated.

The size of the vortex is defined as twice the distance between the positions of the minimum and the maximum value of the transverse velocity, resulting in $L(x = 3.0$m$) = 0.85$m and $L(x = 8.6$m$) = 1.4$m. Comparing these length scales with the ones found for the measurements, $L(x = 3.0$m$) = 0.9$m and $L(x = 8.6$m$) = 1.7$m, we see that especially the length scale at $x = 8.6$m is underestimated. This is again attributed to the incomplete representation of the vertical shear.
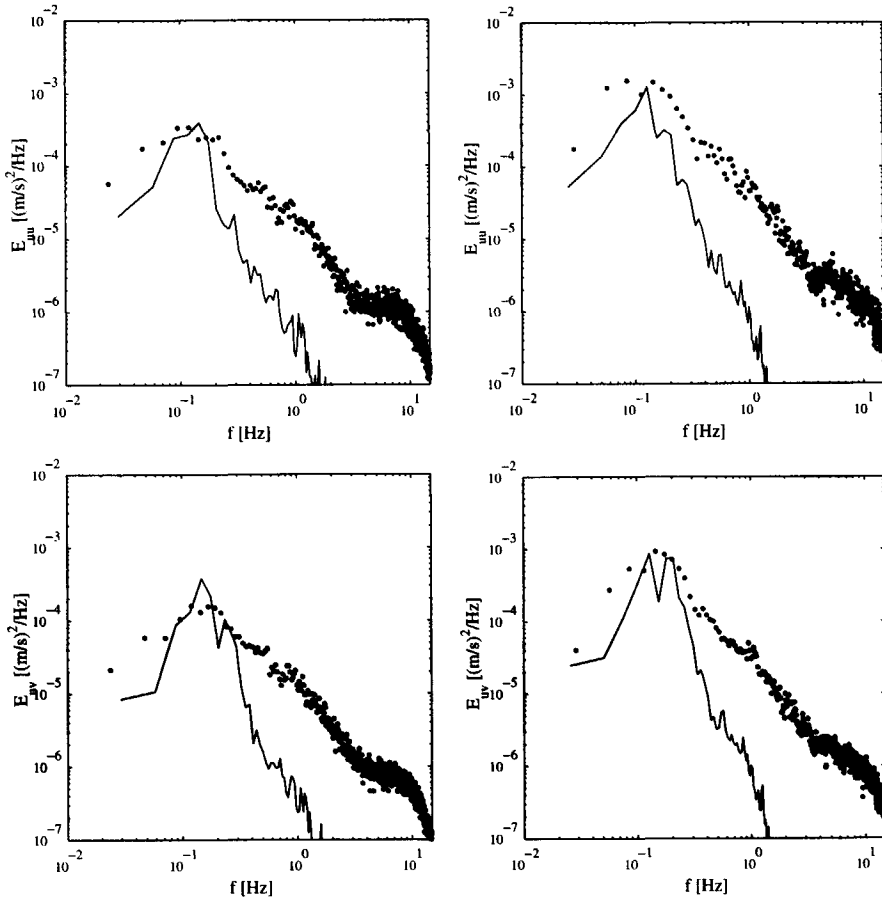
Figure 6.4: Energy density spectra of the streamwise velocity fluctuations (top) and the cross spectra between the streamwise and transverse fluctuations (bottom) at $x = 5.6$m for Case 42 (left) and Case 67 (right).The dots represent the measurements and the solid lines the simulations.

From the analysis of the conditionally averaged vortices it can be concluded that the simulations reproduce the coherent structures fairly well, although the elongation as found in the measurements is underestimated, resulting in too small an amplitude for the transverse velocity, and an underestimation of the values of the Weiss function.
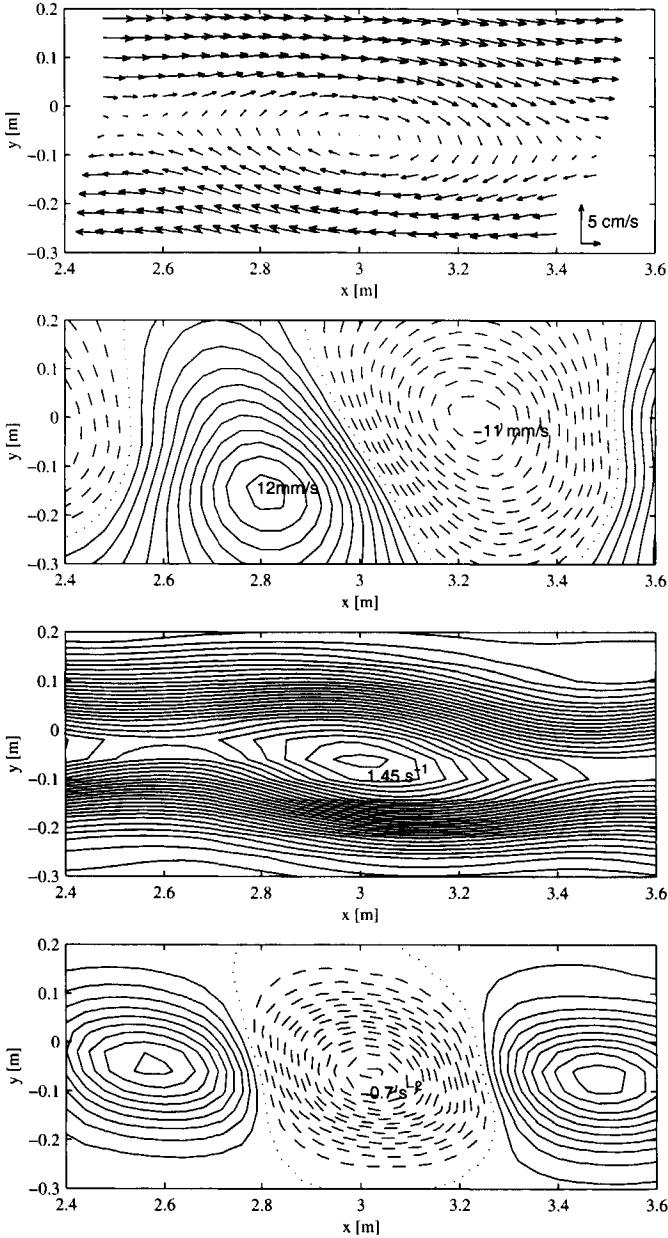
Figure 6.5: Properties of the conditionally averaged vortex at $x = 3.0$m, based on the 2D-TRANS+ks simulations. (a) relative velocity vectors, (b) transverse velocity ($\Delta v = 1$mm/s), (c) vorticity ($\Delta \omega = 0.05$s^{-1}) and (d) Weiss-function ($\Delta Q = 0.05$s^{-2}). Negative values are indicated with a dashed line, positive values with a solid line and zero values with a dotted line.
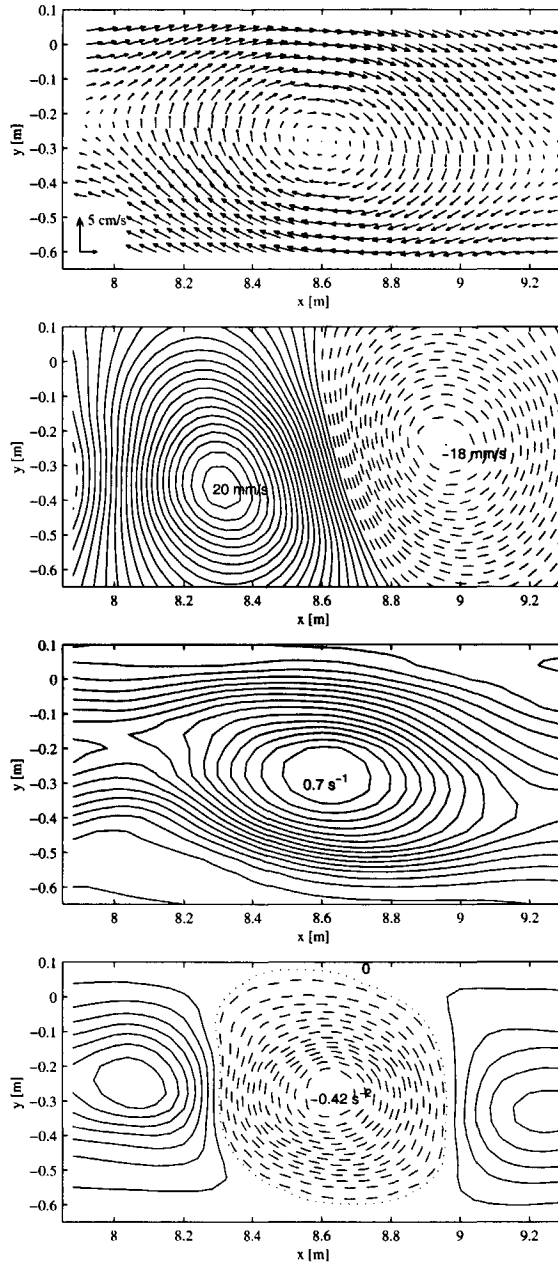
Figure 6.6: Properties of the conditionally averaged vortex at $x = 8.6$m, based on the 2D-TRANS+ks simulations. (a) relative velocity vectors, (b) transverse velocity ($\Delta v = 1$mm/s), (c) vorticity ($\Delta \omega = 0.05$s^{-1}) and (d) Weiss-function ($\Delta Q = 0.03$s^{-2}). Negative values are indicated with a dashed line, positive values with a solid line and zero values with a dotted line.

6.3 Compound channel flow with roughness variation

In order to demonstrate the wider applicability of the developed techniques and to emphasize the need for imposing the kinematic simulation terms, a new flow configuration is introduced: a straight compound channel flow with lateral variation in roughness. Such flow configurations can for example be found in areas which are partly vegetated. Laboratory experiments on these flow types have been carried out by Ikeda&Ohta (1993). Analogous to the shallow mixing layers as discussed in this thesis, large scale vortices were found in the mixing layer at the interface between the rough part and the smooth part.

Simulations are carried out with and without the kinematic simulation terms. Only a qualitative comparison is made to illustrate the effects of the kinematic simulation.

6.3.1 Flow set up

A sketch of the flow configuration is given in figure 6.7. The inflow consists of a uniform rough channel. Further downstream a lateral variation in roughness is imposed. The velocity in the relatively smooth part accelerates and the velocity in the rough part decelerates. A velocity difference develops between the smooth and rough part. At the interface between the rough and the smooth part, a mixing layer will develop. Depending on the flow parameters, coherent structures may be expected.

There are two differences between this flow configuration and the shallow mixing layer downstream of a splitter plate. First, the very steep velocity gradients as found in the initial region of the shallow mixing layer downstream of a splitter plate are absent here. Second, with a rough uniform channel flow upstream of the mixing layer, the effects of the inflow boundary are less important.

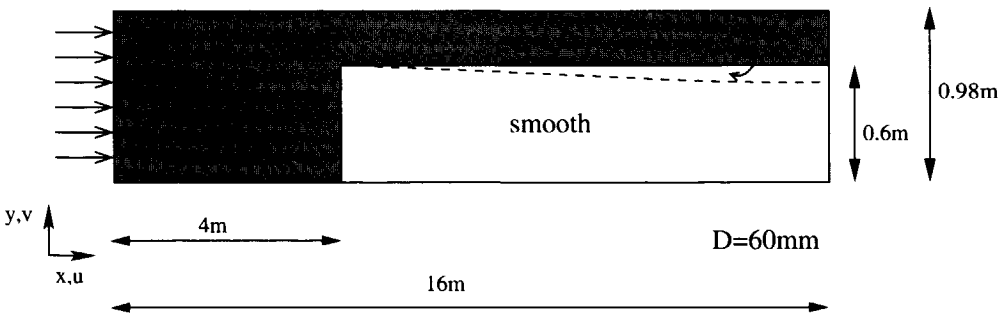|	model	kinematic simulation
Case A	2D-TRANS	-
Case B	2D-TRANS	inflow only
Case C	2D-TRANS+ks	full domain

Figure 6.7: Sketch of the flow configuration (top) and simulation settings (bottom).
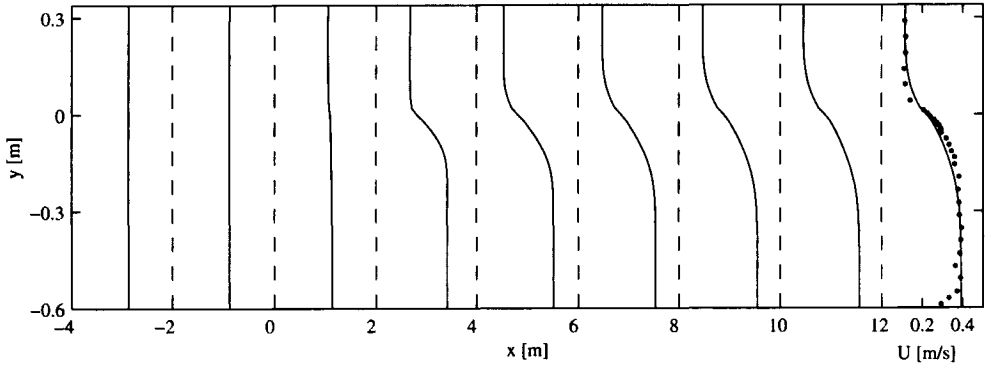
Figure 6.8: Transverse profiles of the mean streamwise velocity of Case C (–). Equilibrium profile as measured by Ikeda&Ohta (1993) (··). The positions of the profiles are indicated by the dashed line (- -).

The flow conditions are chosen the same as the ones used in the experiments carried out by Ikeda&Ohta (1993): a mean streamwise velocity $U = 0.26$m/s and a water depth $D = 6$cm. The friction coefficients of the smooth and rough areas are chosen such that in the far field, the velocities outside the mixing zone equal the experimental values, resulting in $c_{f,rough} = 0.042$ and $c_{f,smooth} = 0.0037$. The width of the computational domain is chosen equal to the width of the experimental set-up of Ikeda&Ohta (1993): $W = 0.98$m. The length of the flow domain is set to $L_{tot} = 16$m, with the length of the inflow channel $L_{inflow} = 4$m.

Three different simulation methods are applied for comparison: (case A) a 2D-TRANS simulation, without any imposed perturbations; (case B) a 2D-TRANS simulation, with perturbations at the inflow only; and (case C) a 2D-TRANS+ks simulation, with perturbations at the inflow and with imposed forcing terms in the entire domain.

6.3.2   Results

Transverse profiles of the mean streamwise velocity of case C are shown in figure 6.8. For comparison the equilibrium profile as measured by Ikeda (1993) is plotted at $x = 12$m. As expected, the flow accelerates on the smooth part until the equilibrium velocity difference is reached. There is a fair agreement between the measured and the simulated equilibrium profiles, although the simulations appear to overestimate the mixing layer width.

The differences between the three cases is discussed using the development of the mixing layer width (Figure 6.9a) and the instantaneous streamwise profiles of the transverse velocity at $y = 0$m, the interface between the rough and the smooth area (Figure 6.9b).

For Case A no fluctuations in transverse velocity are observed, which is clear in the context of Chapter 4. Obviously, the mixing layer is not able to amplify perturbations that

are not there. The flow domain is not long enough to amplify the small numerical errors to significant fluctuations. As a consequence, the mixing layer growth rate is small and only governed by the effective eddy viscosity representing the small scale turbulence.

Perturbations were imposed at the inflow boundary for Case B. As there is no transverse gradient in the streamwise velocity, no production of turbulent kinetic energy takes place in the inflow section. The energy imposed at the inflow boundary will be dissipated as a consequence of the bottom friction and the eddy viscosity. This dissipation is reflected in the decrease of the amplitude of the transverse fluctuations, see Figure 6.9b. At the position where the inflow section ends and the roughness difference starts ($x = 0$), the perturbations have almost vanished. The remaining perturbations are weak and do not play a role in the initial development of the mixing layer. The widening of the mixing layer is initially equal to that found for Case A. Upstream of $x = 4$m perturbations can hardly be detected in the transverse velocity, although a closer look would reveal small amplitude residual perturbations. Downstream of $x = 4$m, the amplitudes of the perturbations grow rapidly until they reach an equilibrium value. The influence of the coherent structures becomes important downstream of $x = 6$m, where the mixing layer width deviates from the width found for Case A. Although it is expected that the mixing layer width will tend to an equilibrium, the domain was not long enough to reach the equilibrium width.

The full 2D-TRANS+ks model is applied in Case C. Perturbations are imposed at the inflow boundary and forcing terms are added to the equations of motion. In contrast to the other two cases, a more or less constant intensity of the transverse fluctuations is obtained for the inflow section, see Figure 6.9b. The imposed forcing terms maintain the inflow perturbation level. Perturbations are therefore present at the start of the mixing layer, which are amplified in the mixing layer. These fluctuations contribute directly to the broadening of the mixing layer, see Figure 6.9a. A monotonically growing mixing layer width is obtained. The mixing layer width tends to an equilibrium that is somewhat higher than the mixing layer width found in the experiments of Ikeda (1993). Clearly, the experiment is more complicated than the simple representation of the vegetation by extra roughness.

From this qualitative analysis, it is concluded that imposed forcing terms in the equations of motion, representing the large scale bottom turbulence, are required for a proper and realistic simulation of a developing mixing layer starting at an arbitrary position in the flow.

6.4 Discussion on practical use of 2D-TRANS+ks

In Chapter 5 a TRANS model with kinematic simulation (2D-TRANS+ks) has been proposed. In this chapter the model has been applied to shallow shear flows. Good results are obtained for the mean flow and reasonable results for the development of the coherent structures. The case of the compound channel flow with roughness variation illustrates the need of imposing perturbations on the entire flow domain.

Although this gives some confidence in favour of the use of the 2D-TRANS+ks model
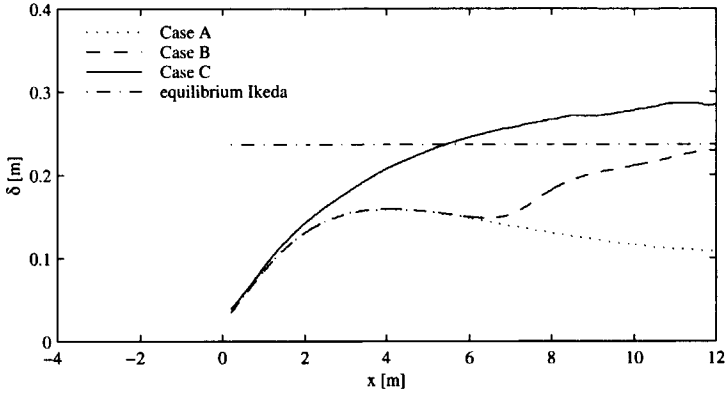
a
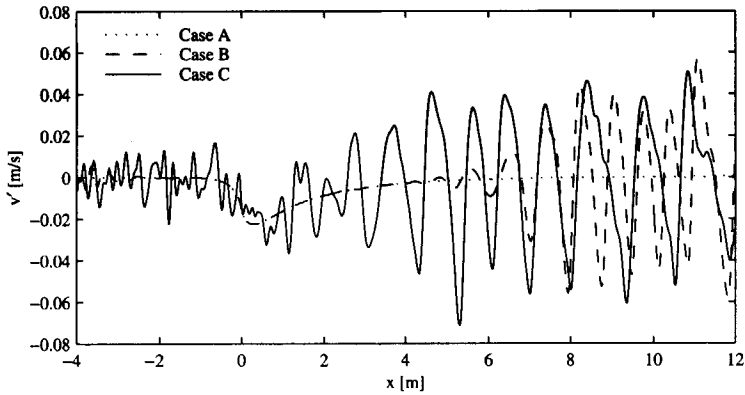
b

Figure 6.9: (a) Mixing layer widths of the simulations and the equilibrium width as measured by Ikeda&Ohta (1993). (b) Instantaneous streamwise variation of the transverse velocity at $y = 0$, the interface between the rough and smooth part.

in the practice of civil and environmental engineering, some comments have to be made.

First, the model as implemented here requires a grid that is aligned to the main flow direction. This dependency is reflected in the different definitions for the amplitudes of the kinematic simulation, see Equation 5.8 and 5.9 and Figure 5.5. The orientation dependency of the grid is also reflected in the way the kinematic simulation is implemented in the shallow water equations, see Equation 5.12-5.13. A more general implementation of the kinematic simulation is therefore needed for complex grids and complex flows, which can be related to the principal axes of the rate-of-strain tensor of the 2D velocity field.

Second, as was mentioned in the first part of this chapter, a constant velocity is used to determine the temporal development of the acceleration terms. Although reasonable results were obtained with a constant value, a sensitivity study on this subject should be carried out to investigate the consequences of this assumption. An example where the assumption of a uniform velocity is probably not allowed is a recirculating flow.

Third, in the simulations the flow was assumed two-dimensional, neglecting the influence of the dispersion of the vortices by the mean vertical shear. As a consequence, the simulated vortices are not stretched by this mechanism, resulting in transverse velocity fluctuations that are too high and streamwise fluctuations that are too low. With a multi-layered simulation these discrepancies might be overcome.

Fourth, the kinematic simulation is based on the turbulence characteristics of a uniform channel flow. Irregularities in the bathymetry may cause different types of fluctuations. Difficulties can for example be expected in cases with river dunes on the bottom.

Fifth, we focused on the generation mechanism known as *internal instabilities* (Jirka, 2001). No attention was paid to the generation type *topographical forcing*, where separation becomes important. Such flow conditions have not been tested with the 2D-TRANS+ks model.

In view of these comments, it is concluded that we should take care with the use of the 2D-TRANS+ks model as an engineering tool for a wide range of applications. Its limitations should be kept in mind when applying it, as with every model. However, the proposed model gives fairly good results without tuning of parameters and it can be considered as an improvement to the current state-of-the-art models. Further improvement may lead to a wider application to more complex flow types.

Chapter 7

Conclusions and recommendations

Shallow mixing layer flows have been investigated with the aim to obtain better insights in the genesis and development of the large scale horizontal coherent structures and to use these insights for tools that can be applied in the practice of civil and environmental engineering. Three methodologies have been followed: laboratory experiments, analytical modeling and numerical modeling. The results of these methods of analysis are combined leading to a description for the development of the mixing layer and horizontal structures (Section 7.1). The insights are used in the development of a better set of models to predict shallow shear flows in the practice of environmental engineering. Quick and simple models, or rules of thumb, are given in Section 7.2. Such models can be used for a first impression of the development of the mean flow and the coherent structures. For a more detailed description of shallow shear flows, numerical models are appropriate, see Section 7.3. In such models the horizontal coherent structures are resolved. Finally, questions that came up during the project and questions that still remain are discussed in Section 7.4, together with suggestions for further research.

7.1 Development of mean flow and coherent structures

The results of the different methodologies are combined in this section, leading to a classification in accordance with the following stages in the development of the mean flow and the coherent structures over a horizontal bottom:

- Stage 1: "near field"
  In the near field downstream of the splitter plate the velocity difference is high and the mixing layer width is of the order of magnitude of the water depth. The transverse profile of the streamwise velocity is influenced by the boundary layers that have developed along the splitter plate. The flow is strongly three-dimensional and non-linear interactions are expected to play an important role. The initial region ends where the mixing layer width is larger than roughly twice the water depth $x < x(\delta \simeq 2D)$.

- Stage 2: "growth of intensity of the dominant mode"
  This stage starts at the position where the mixing layer width is about twice the water depth $x(\delta \simeq 2D)$. The coherent structures grow in size and intensity due to the dominating horizontal shear. This stage ends where the coherent structures start to decay and is found at the position where the growth ratio of the dominant mode becomes zero ($\omega_{i,dom} = 0$).

- Stage 3: "unstable flow, with a decreasing intensity of the dominant mode"
  The dominant mode has reached its highest energy density level and starts to decay: $\omega_{i,dom} < 0$. This does not imply that all modes decay. As the dominant mode is highly determined by the upstream development of the coherent structures, the wavenumber of the dominant mode is generally larger than the wavenumber of the most unstable mode. Unstable modes may therefore still exist. This stage ends where the growth rate of the most unstable mode becomes zero ($\omega_{i,m.u.} = 0$). The bottom friction parameter resches its critical value $S = S_c$. Although the energy density decreases, the length scale of the dominant mode still increases. In this stage the paradoxical situation exists that the flow is unstable but that the mean turbulent kinetic energy of the horizontal coherent structures decreases.

- Stage 4: "stable flow with coherent structures"
  At this stage the flow is stable, as the growth rates of all modes are negative ($\omega_i < 0$ or $S = S_c$), but coherent structures still exist. The end of this stage is reached, where the coherent structures have been dissipated so that the energy density level is similar to the level of the bottom turbulence ($E \simeq E_{bt}$).

- stage 5: "stable flow without coherent structures"
  At this final stage, the horizontal coherent structures are absent. In case a velocity difference still exists, the mixing layer widens due to bottom turbulence until uniform channel flow is reached.

As a mixing layer can be seen as an amplifier of coherent structures, initial perturbations are required for the genesis of coherent structures. It is inferred that the coherent structures in shallow mixing layer flows have their origin in the large scale depth averaged components of the bottom turbulence. These components were found to exist with a large eddy simulation model in which the bottom turbulence was resolved. Regarding the generation mechanism of the turbulence structures as proposed by Jirka (2001), the shallow mixing layer falls in two categories. The large scale bottom turbulence falls in the third category *secondary instabilities of base flow*. The further development, under influence of the horizontal shear, is in accordance with the second type of generation *internal transverse shear instabilities*.

The evolution of the coherent structures is determined by the feeding due to the mean shear and the dissipation by the bottom friction and the eddy viscosity. In the flow configurations investigated here, non-linear interactions turned out to be weak. A linear approximation as proposed in Chapter 3 is found to be a good approximation for the prediction of the development of coherent structures. For intense coherent structures the non-linear

interactions, like vortex merging, can play a role. Further investigation is required to derive criteria for the importance of the non-linear interactions.

7.2 Quick and simple tools

7.2.1 Developing shallow mixing layer

In order to get a first impression of the development of the mean streamwise velocity in a developing mixing layer, the self-similarity model as described in Chapter 3 appears useful. This set of equations describes the mean flow well compared to the measurements. The explicit determination of the size and intensity of coherent structures appeared not to be necessary for this purpose.

A first impression of the presence of coherent structures can be obtained with the bottom friction parameter S (Equation 1.2.3). From the position where the bottom friction has reached its critical value, all modes dissipate. The kinetic energy of the coherent structures is dissipated for the greater part at a position a few times λ downstream of the position where $S = S_c$, with $S_c = 0.05 - 0.12$.

A more sophisticated method to determine the size and intensity of the coherent structures is the method based on linear stability analysis as proposed in Chapter 3. With this method the growth rates obtained by linear stability analysis are integrated in downstream direction, resulting in the development of the amplification of each mode of the inflow perturbation and the determination of the locally dominant mode. The history of the coherent structures is thus taken into account.

7.2.2 Compound channel flow

In slight deviation from the main research line, the uniform flow in a straight prismatic compound channel has been investigated in Appendix I. For the prediction of the conveyance of such a channel, the transverse profile of the mean streamwise velocity in the mixing layer between the relatively deep main channel and the relatively shallow floodplain has to be known. For that purpose, a number of models has been developed in the past for the transverse exchange of momentum. However, most of these models lack a physical background and require empirical constants with a sometimes wide and unrealistic range of values. Therefore a new physically based model has been developed, representing the most important mechanisms for the momentum exchange. This model takes into account the effects of bottom turbulence and the effects of horizontal coherent structures. Special attention was paid to the influence of the lateral depth variation on the dynamics of the horizontal coherent structures. It turned out that the proposed model gives realistic predictions of observed depth averaged mean streamwise velocities and depth averaged transverse shear stresses.

7.3   Numerical modeling

Numerical models can be applied at different levels of detail. A depth-integrated numerical model in which the large scale horizontal motion is resolved and the small scale bottom turbulence is modeled is most appropriate for simulating horizontal coherent structures in shallow shear flows. This way of modeling is referred to as two-dimensional Transient Reynolds Averaged Navier Stokes (2D-TRANS) simulations. More detailed simulations, like three-dimensional Direct Numerical Simulations (DNS) or three-dimensional Large Eddy Simulations (LES), require a very high computer capacity whereas simulations at a lower level of detail, like two- or three-dimensional Reynolds Averaged Navier Stokes (RANS) simulations are computationally less expensive, but they do not resolve the dynamics of the horizontal coherent structures.

Compared to conventional 2D-RANS simulations, a few modifications have to be made to perform 2D-TRANS simulations. The mesh size has to be chosen in the order of magnitude of the water depth. For example, resolving the length scales of the order of twice the water depth requires roughly a mesh size of one third of the water depth. Furthermore, a classical RANS turbulence model should be used for the representation of the small scale bottom turbulence. It is noted that for larger mesh sizes a more sophisticated turbulence model is required to take into account also the non-resolved depth averaged motion (Kernkamp & Uittenbogaard, 2001).

In Chapter 4 it was concluded that imposed perturbations are required to initiate the development of the horizontal coherent structures. These perturbations represent the large scale components of the bottom turbulence, that can principally not be resolved by a depth averaged simulation. This large scale bottom turbulence is therefore mimicked by means of a kinematic simulation, leading to the 2D-TRANS+ks model (see Chapter 5). This kinematic simulation has been implemented as a velocity fluctuation at the inflow boundary and as a forcing over the entire domain. The necessary parameters have been extracted from a full three-dimensional simulation of a uniform channel flow. The 2D-TRANS+ks model was tested in Chapter 6 for shallow shear flows, leading to good results for the mean flow field. However, some discrepancies between the measurements and the simulations have been found for the properties of the coherent structures.

7.4   Further improvements

A number of questions were not answered in the course of this project. Maybe the most striking unresolved question deals with the relation between the mean flow development and the development of the coherent structures. The measured cases of two different depths show a significant difference in intensity of coherent structures, whereas the mean flow development can be described with a self-similarity model, using the same entrainment coefficient. Similar results were obtained with the numerical simulations. Increasing the level of the inflow perturbations has led to significant differences in intensity of coherent structures, but to limited effects on the mean flow, including the mixing layer width. Such

results were also obtained for shallow jet flows (Dracos *et al.*, 1992). The spreading rates of the jets as found by Dracos *et al.* are all within a very narrow range (96%-108% of the mean spreading rate), regardless of the significant differences in intensity of coherent structures. No sound physical explanation has been found for this apparent discrepancy. However, the consequence is convenient from an engineering point of view, as the mean flow appears to be hardly dependent on the intensity of the coherent structures. This property of shear flows partly explains the validity of the analytical approach as proposed in Chapter 3, in which first the mean flow was modeled and subsequently the development of the coherent structures.

In the numerical simulations, a simple turbulence model (Elder formulation) has been used for the dissipation of kinetic energy by the small scale bottom turbulence. The Elder formulation has been validated for uniform channel flows. The empirical constant is determined accounting for the total turbulent motion, including large scale motions. No further improvement of the eddy viscosity model for the three-dimensional turbulent motion was made here. Eddy viscosity models should be tested with a three-dimensional large eddy simulation of for example a shallow mixing layer.

One of the discrepancies between the measurements and the 2D-TRANS+ks simulations was ascribed to the effects of the vertical shear, which was present in the experiments, but absent in the numerical simulations. Due to this shear the coherent structures are elongated in streamwise direction. This dispersion effect could not be quantified properly by the measurements as only the surface velocity was measured.

Another three-dimensional effect that was briefly mentioned is the secondary circulation in the vortices. It could be observed in the experiments that particles, spread over the water surface, tend to move away from the center of the vortices. Although these secondary velocities were small, they might have a net effect on the dispersion of contaminants out of the center of a vortex. Experiments for determining these small secondary effects are expected to be difficult as spatial information is required in all three dimensions. Large eddy simulation seems to be a more appropriate method for the determination of these three-dimensional effects.

No attention was paid here to coherent structures generated by the stronger type of generation reffered to as *topographical forcing*, in which coherent structures are shed from an obstacle (Jirka, 2001). For flow configurations of this type the generation of coherent structures out of bottom turbulence is expected to play a minor role. The local flow and bathymetry properties in the neighborhood of the topographical forcing are likely to be more important.

References

ALAVIAN, V., & CHU, V.H. 1985. Turbulent exchange flow in shallow compound channel. *Pages 446 451 of: Proc. 21st IAHR Congress, Melbourne.*

ASHWORTH, P.J., BENNET, S.J., BEST, J.L., & McLELLAND, S.J. (eds). 1996. *Coherent flow structures in open channels.* John Wiley & Sons. Chap. "Floodplain secondary circulation as a mechanism for flow and shear stress redistribution in straight compound channels", pages 581–608.

BALARAS, E., PIOMELLI, U., & WALLACE, J.M. 2001. Self-similar states in turbulent mixing layers. *Journal of Fluid Mechanics,* **446**, 1–24.

BARBERA, G. (ed). 1983. *Leonardo e le vie d'aqua.* G. Barbera.

BARISHNIKOV, N.B., & IVANOV, G.V. 1971. Role of flood plain in flood discharge of a river channel. *Pages 141–144 of: Proc. 14th congress of the IAHR, Paris.*

BASTIAANS, R.J.M., VAN DER PLAS, G.A.J., & KIEFT, R.N. 2002. The performance of a new PTV algorithm in super-resolution PIV. *Experiments in Fluids,* **32**, 346–356.

BATCHELOR, G.K. 1969. Computation of the energy spectrum in homogeneous two-dimensional turbulence. *Phys. Fluids Suppl. II,* 233–239.

BIJVELDS, M.D.J.P., KRANENBURG, K.C., & STELLING, G.S. 1999. 3d numerical simulation of turbulent shallow-water flow in Square Harbor. *Journal of Hydraulic Engineering,* **125**(1), 26 31.

BOUSMAR, D. 2002. *Flow modelling in compound channels.* Ph.D. thesis, Universite catholique de Louvain.

BROWN, G.L., & ROSHKO, A. 1974. On density effects and large structure in turbulent mixing layers. *Journal of Fluid Mechanics,* **64**, 775–816.

CHASNOV, J.R. 1991. Simulation of the Kolmogorov inertial subrange using an improved subgrid model. *Physics of Fluids A,* **3**(1), 188–200.

CHEN, D., & JIRKA, G.H. 1995. Experimental study of plane turbulent wake in a shallow water layer. *Fluid Dynamics Research,* **16**(11).

CHEN, D., & JIRKA, G.H. 1997. Absolute and convective stabilities of plane turbulent wakes in a shallow water layer. *Journal of Fluid Mechanics*, **338**, 157–172.

CHEN, D., & JIRKA, G.H. 1998. Linear stability analysis of turbulent mixing layers and jets in shallow water layers. *Journal of Hydraulic research*, **36**, 815–830.

CHEN, D., & JIRKA, G.J. 1999. A laser-induced fluorescence study of a plane shallow jet. *Journal of Hydraulic Engineering*, **125**.

CHU, V.H., & BABARUTSI, S. 1988. Confinement and bed-friction effects in shallow turbulent mixing layers. *Journal of Hydraulic Engineering*, **114**, 1257–1274.

CHU, V.H., WU, J.H., & KHAYAT, R.E. 1989. Stability of the transverse shear flow in shallow open channels. *Journal of Hydraulic Engineering*, **117**, 1371–1388.

CRAMP, A., COULSON, M., JAMES, A., & BERRY, J. 1991. A note on the observed and predicted flow patterns around islands - Flat Holm, the Bristol Channel. *Int. Journal Remote Sensing*, **12**(5), 1111–1118.

DE NIJS, M. 2003. *Sensitivity of shallow mixing layers to upstream turbulence*. M.Phil. thesis, Delft University of Technology.

DRACOS, T., GIGER, M., & JIRKA, G.H. 1992. Plane turbulent jets in a bounded fluid layer. *Journal of Fluid Mechanics*, **214**, 587–614.

DRAZIN, P.G., & REID, W.H. 1981. *Hydrodynamic stability*. Cambridge University Press.

EGGELS, J.G.M. 1994. *Direct and Large Eddy Simulation of turbulent flow in a cylindrical Pipe Geometry*. Ph.D. thesis, TU Delft.

EMERY, J.W., & THOMSON, R.E. 1997. *Data analysis methods in physical oceanography*. Pergamon.

ERVINE, D.A., BABAEYAN-KOOPAEI, K., & SELLIN, R.H.J. 2000. Two-dimensional solution for straight and meandering overbank flows. *Journal of Hydraulic Engineering*, **126**(9), 653–669.

FISCHER, H.B., LIST, E.J., KOH, R.C.J., IMBERGER, J., & BROOKS, N.H. 1979. *Mixing in inland and coastal waters*. Academic Press, New York, N.Y.

FLÜGEL, G. 1939. Die berechnung der Strahlapparate auf Grund der Energieleichung. *VDI-Forschungsheft*, **395**.

FUNG, J.C.F., HUNT, J.C.R., MALIK, N.A., & PERKINS, R.J. 1992. Kinematic simulation of homogeneous turbulence by unsteady random Fourier modes. *Journal of Fluid Mechanics*, **236**, 281–318.

GASTER, M. 1962. A note on the relation between temporally-increasing and spatially-increasing disturbances in hydrodynamic stability. *Journal of Fluid Mechanics*, **14**, 222–224.

GERMANO, M., PIOMELLI, U., MOIN, P., & CABOT, W.H. 1991. A dynamic subgrid-scale eddy viscosity model. *Phys. Fluids A*, **3**(7), 1760–1765.

GHIDAOUI, M.S., & KOLYSHKIN, A.A. 1999. Linear stability analysis of lateral motions in compound open channels. *Journal of Hydraulic Engineering*, **125**, 871–880.

HANJALIC, K. 2002. One-point closure models for buoyancy-driven turbulent flows. *Annual review Fluid Mechanics*, **34**, 321–347.

HINTERBERGER, C., FROHLICH, J., & RODI, W. 2002. Depth-averaged large eddy simulation of shallow water flows - modelling aspects. *In: Advances of turbulence IX, Proc. of 9th European Turbulence Conference. Barcelona.*

HUSSAIN, A.K.M.F., & ZEDAN, M.F. 1978a. Effects of the initial condition on the axisymmetric free shear layer: Effects of the initial momentum thickness. *Physics of Fluids*, **21**(7), 1101–1112.

HUSSAIN, A.K.M.F., & ZEDAN, M.F. 1978b. Effects of the initial condition on the axisymmetric free shear layer: Effects of the initial fluctuation level. *Physics of Fluids*, **21**(9), 1475–1481.

IKEDA, S., & OHTA, K. 1993. Instability induced horizontal vortices in shallow open-channel flows. *In: Ninth symposium on "Turbulent Shear Flows", Kyoto.*

IKEDA, S., KAWAMURA, K., TODA, Y., & KASUYA, I. 2002. Quasi-three-dimensional computation and laboratory tests on flow in curved compound channels. *Pages 233–245 of: Proc. Riverflow 2002.*

JIRKA, G.H. 2001. Large scale flow structures and mixing processes in shallow flows. *Journal of Hydraulic Research*, **39**(6), 567.

J.P., BONNET, J., DELVILLE, M.N., GLAUSER, R.A., ANTONIA, D.K., BISSET, D.R., COLE, H.E., FIEDLER, J.H., GAREM, D., HILBERG, J., JEONG, N.K.R., KEVLA-HAN, L.S., UKEILEY, & E., VINCENDEAU. 1998. Collaborative testing of eddy structure identification methods in free turbulent shear flows. *Experiments in Fluids.*

KERNKAMP, H.W.J., & UITTENBOGAARD, R.E. 2001. 2D-LES of a free surface mixing layer. *Pages 409–418 of:* GEURTS, B.J., FRIEDRICH, R., & METAIS, O. (eds), *Direct and Large-Eddy simulation workshop.*

KIM, K.C., & ADRIAN, R.J. 1999. Very large-scale motion in the outer layer. *Physics of Fluids*, **11**(2).

KIMURA, I., HOSADA, T., & ONDA, S. 2002. Prediction of 3D flow structures araound skewed spur dikes by means of a non-linear k-ε model. *Pages 65–73 of:* BOUSMAR, D., & ZECH, Y. (eds), *Riverflow 2002.* Balkema.

KNIGHT, D.W., & SHIONO, K. 1990. Turbulence measurements in a shear layer region of a compound channel. *Journal of Hydraulic Research,* **28**(2), 175–196.

KRAICHNAN, R. 1967. Inertial ranges in two-dimensional turbulence. *Physics of Fluids,* **10**, 1417–1428.

LAMBERT, M.F., & SELLIN, R.H.J. 1996. Discharge prediction in straight compound channels using the mixing length concept. *Journal of Hydraulic Research,* **34**(3), 381–394.

LEITH, C.E. 1990. Stochastic backscatter in a subgrid-scale model: plane shear mixing layer. *Physics of Fluids A,* **3**(2), 297–299.

LESIEUR, M. 1997. *Turbulence in fluids.* Kluwer Academic Publishers.

MICHALKE, A. 1964. On the inviscid instability of the hyperbolic-tangent velocity profile. *Journal of Fluid Mechanics,* **19**, 543–556.

MICHALKE, A. 1965. On spatially growing disturbances in an inviscid shear layer. *Journal of Fluid Mechanics,* **23**, 521–544.

MOIN, P., & KIM, J. 1982. Numerical investigation of turbulent channel flow. *Journal of fluid mechanics,* **118**, 341–377.

MOSER, R.D., KIM, J., & MANSOUR, N.N. 1999. Direct numerical simulation of turbulent channel flow up to $\mathrm{Re}_\tau = 590$. *Physics of Fluids,* **11**(4).

NADAOKA, K., & YAGI, H. 1998. Shallow-water turbulence modeling and horizontal large-eddy computation of river flow. *Journal of Hydraulic Engineering,* **124**(5), 493–500.

NEZU, I., & NAKAGAWA, H. 1993. *Turbulence in open-channel flows.* IAHR monographs series. Balkema Rotterdam.

OGINK, H.J.M. 1985. The effective viscosity coefficient in 2-D depth-averaged flow models. *Pages 475–479 of: Proc.21st IAHR Congress, Melbourne.*

OSTER, D., & WYGNANSKI, I. 1982. The forced mixing layer between two parallel streams. *Journal of Fluid Mechanics,* **123**, 91–130.

PIOMELLI, U., FERZIGER, J., & MOIN, P. 1989. New approximate boundary conditions for large eddy simulations of wall-bounded flows. *Phys. Fluids A,* **1**(6), 1061–1068.

POPE, S.B. 2000. *Turbulent flows.* Cambridge University Press.

SAGAUT. 1998. *Large Eddy Simulation for incompressible flows.* Scientific computation. springer.

SCARANO, F., BENOCCI, C., & RIETHMULLER, M.L. 1999. Pattern recognition analysis of the flow past a backward facing step. *Physics of fluids,* **11**(12), 3808 3818.

SCHUMANN, U. 1975. Subgrid scale model for finite difference simulations of turbulent flows in plane channels and annuli. *J. Comput. Physics,* **18**, 376–404.

SELLIN, R.H.J. 1964. A laboratory investigation into the interaction between the flow in the channel of a river and that over its flood plain. *La Houille Blanche,* **110**, 689–789.

SHIONO, K., & KNIGHT, D.W. 1991. Turbulent open channel flows with variable depth across the channel. *Journal of Fluid Mechanics,* **222**, 617–646.

SLESSOR, M.D., BOND, C.L., & DIMOTAKIS, P.E. 1998. Turbulent shear-layer mixing at high Reynolds numbers: effects of inflow conditions. *Journal of Fluid Mechanics,* **376**, 115–138.

SOFIALIDIS, D., & PRINOS, P. 1998. Compound open-channel flow modeling with nonlinear low-Reynolds k-ε models. *Journal of Hydraulic Engineering,* **3**, 253–262.

SOFIALIDIS, D., & PRINOS, P. 1999. Numerical study of momentum exchange in compound open channel flow. *Journal of Hydraulic Engineering,* **2**, 152–165.

SPALART, P.R. 2000. Strategies for turbulence modeling and simulations. *International Journal of Heat and Fluid Flow,* **21**, 252–263.

TAMAI, N., ASEADA, T., & IKEDA, H. 1986. Study on generation of periodical large surface eddies in a composite channel flow. *Water Resources Research,* **22**(7), 1129–1138.

TENNEKES, H., & LUMLEY, J.L. 1972. *A first course in turbulence.* the MIT Press, Cambridge.

TOMINAGA, A., & NEZU, I. 1991. Turbulent structure in open compound channel flows. *Journal of Hydraulic Engineering, ASCE,* **117**(2), 21–41.

TOWNSEND, A.A. 1976. *The structure of turbulent shear flow.* Cambridge University Press.

TUKKER, J. 1997. *Turbulence structures in shallow free-surface mixing layers.* Ph.D. thesis, TU Delft.

UIJTTEWAAL, W.S.J., & BOOIJ, R. 2000. Effects of shallowness on the development of free-surface mixing layers. *Physics of Fluids,* **12**(2), 392–420.

VAN PROOIJEN, B.C., & UIJTTEWAAL, W.S.J. 2002a. A linear approach for the evolution of coherent structures in shallow mixing layers. *Physics of Fluids*, **14**(12), 4105–4114.

VAN PROOIJEN, B.C., & UIJTTEWAAL, W.S.J. 2002b. On the initiation of large scale turbulence structures in the numerical simulation of shallow mixing layers. *Pages 57–64 of:* BOUSMAR, D., & ZECH, Y. (eds), *Riverflow 2002*. Balkema.

VAN PROOIJEN, B.C., BATTJES, J.A., & W.S.J.UIJTTEWAAL. 2003. Momentum exchange in uniform compound channel flows. *to be submitted*.

VON CARMER, C.F., WEITBRECHT, V., & JIRKA, G.H. 2001. On the genesis and fate of large coherent vortical structures in turbulent shallow wake flows. *In: Proc. of Int. Symposium on Environmental Hydraulics, Tempe, Arizona*.

VREMAN, B. 1995. *Direct and Large-Eddy Simulation of the Compressible Turbulent Mixing Layer*. Ph.D. thesis, University of Twente.

VREUGDENHIL, C.B. 1994. *Numerical methods for shallow-water flow*. Kluwer Academic Publishers, Dordrecht, The Netherlands.

WINANT, C.D., & BROWAND, F.K. 1974. Vortex pairing: the mechanism of turbulent mixing layer growth at moderate Reynolds number. *Journal of Fluid Mechanics*, **63**, 237–255.

WORMLEATON, P.R. 1988. Determination of discharge in compound channels using the dynamic equation for lateral velocity distribution. *Pages 98–103 of: Int. Conf. on Fluvial Hydraulics*. IAHR.

WORMLEATON, P.R. 1996. *Coherent flow structures in open channels*. John Wiley & Sons. Chap. "Floodplain secondary circulation as a mechanism for flow and shear stress redistribution in straight compound channels", pages 581–608.

ZHOU, M. DE, & WYGNANSKI, I. 2001. The response of a mixing layer formed between parallel streams to a concomitant excitation at two frequencies. *Journal of Fluid Mechanics*, **441**, 139–168.

Appendix A

Momentum exchange in straight uniform compound channel flow

abstract

Transverse exchange of momentum between the channel and the floodplain in straight uniform compound channel flow is considered in this paper. This process results in the so-called 'kinematic effect', a lowering of the total discharge capacity of a compound channel compared to the case where the channel and the floodplain are considered separately. The mechanisms responsible for the momentum exchange are considered. The transverse shear stress in the mixing region is modeled using a newly developed effective eddy viscosity concept, that contains (1) the effects of horizontal coherent structures moving on an uneven bottom, taking compression and stretching of the vortices into account, and (2) the effects of the three-dimensional bottom turbulence. The model gives a good prediction of the transverse profiles of the streamwise velocity and the transverse shear stress of the Flood Channel Facility experiments. Characteristic features of the lateral profile of the eddy viscosity are also well predicted qualitatively, but in a quantitative sense there is room for improvement. Secondary circulations are shown to be of minor importance in straight uniform compound channel flows.

Introduction

Many rivers consist of a channel with adjacent floodplains. The bottom of the floodplain is generally higher and rougher than the bottom of the main channel, so that during flood the river consists of a relatively deep channel and shallow floodplains, a so-called compound channel. In this paper we consider uniform flow in straight compound channels to investigate in particular the influence of the lateral depth variation on the flow. The schematised cross section of such a compound channel is shown in Figure A.1. Due to the difference in water depth and bottom friction, a difference in streamwise velocity is generated, the velocity on the floodplain being lower than that in the channel. The cross section of a river can now be divided in transversely uniform zones (assuming sufficiently high width/depth ratios) and a mixing zone, see Figure A.1. The depth-integrated transverse exchange of mass and momentum in the transversely uniform zones is zero. In the mixing zone, trans-
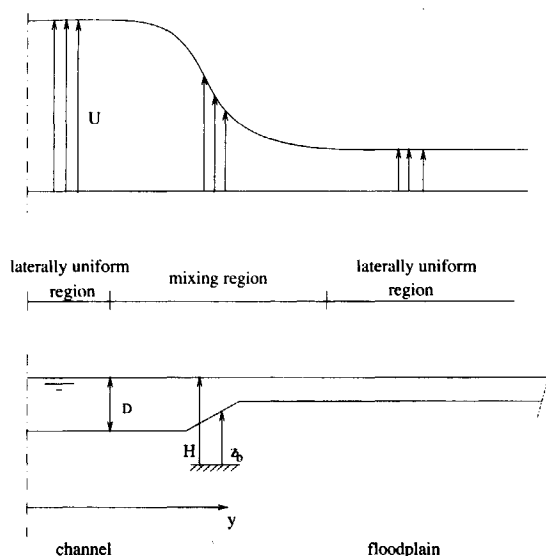
Figure A.1: Sketch of half the cross section of a compound channel

verse gradients in bottom level and/or the velocity are present, causing exchange of mass and momentum.

An important consequence of the presence of the mixing region is the reduction of discharge capacity of the river compared to a situation in which the channel and the floodplain are considered as separated channels. This is called the 'kinematic effect' (Barishnikov & Ivanov, 1971). In order to determine the stage-discharge relationship for a compound channel, the transverse profile of the streamwise velocity in the mixing region has to be known. A number of studies has been devoted to the determination and prediction of these profiles (Alavian & Chu, 1985; Shiono & Knight, 1991; Lambert & Sellin, 1996; Ervine et al., 2000).

Transverse exchange of momentum is caused by mean flow and turbulence. The mean-flow contribution can be separated in a contribution by the depth-averaged downstream and lateral velocities and another one by the effect of the vertical variation of these velocities, the so-called advective dispersion. The latter is usually associated with secondary circulations, i.e. vortex tubes with their axes in the streamwise direction. They are found in the compound channel flow experiments of Tominaga&Nezu (1991) and Shiono&Knight (Shiono & Knight, 1991) and they were successfully simulated with a three-dimensional numerical model by Sofialidis&Prinos (1999).

The turbulence contribution is due to small-scale turbulence induced by the bottom resistance and by turbulence generated by lateral shear of the mean flow, which manifests itself primarily in the form of large coherent structures, with their axes more or less perpendicular to the bottom. They are generally much larger than the water depth. Examples of

these horizontal coherent structures can be found in many different types of shallow flows, such as island wakes (Cramp *et al.*, 1991), shallow jets (Dracos *et al.*, 1992) or shallow mixing layers (Uijttewaal & Booij, 2000; van Prooijen & Uijttewaal, 2002a). The first visualizations of large scale coherent structures in compound channel flows were made by Sellin (1964). High resolution numerical simulations, in which the large scale motion is resolved, have recently been performed by Nadaoka&Yagi (1998) and Ikeda&Toda (2002).

Bottom turbulence is induced by the no-slip condition at the bottom. This turbulent motion contains the characteristic burst phenomena as found in wall flows. The typical turbulence length scale is of the order of the water depth.

Accurate modeling of the above-mentioned mechanisms of momentum exchange turned out to be difficult, as is evident from the use of a variety of exchange models (Alavian & Chu, 1985; Shiono & Knight, 1991; Lambert & Sellin, 1996; Ervine *et al.*, 2000). In each study, one of the mechanisms is generally considered most important and modeled with an effective eddy viscosity. Most of the models for the transverse profile of the streamwise velocity turned out to be reasonably capable of predicting the transverse profiles of the streamwise velocity, but only after calibration of one or more empirical constants. The large diversity in the mechanisms that have been modeled, and their empirical character, makes the general applicability of the models questionable. Besides, no explicit comparisons have been made between the measured and modeled transverse shear stress or eddy viscosity in, for example, Alavian&Chu (1985), Shiono&Knight (1991), Lambert&Sellin (1996), and Ervine et al. (2000).

In this paper different mechanisms responsible for the momentum exchange in a straight compound channel are briefly examined. Subsequently, the mechanisms considered most important are modeled with a new physically based eddy viscosity in which large coherent structures play a key role. The results compare favorably well with the transverse profiles of the mean streamwise velocity and the transverse shear stress measured in the Flood Channel Facility experiments (Knight&Shiono, 1990).

Governing equations

In order to study the processes in steady open channel flow, the depth-integrated and time-averaged shallow water equations are used as a starting point:

$$\frac{\partial D\overline{U}}{\partial x} + \frac{\partial D\overline{V}}{\partial y} = 0$$

$$\frac{\partial D\overline{U}\,\overline{U}}{\partial x} + \frac{\partial D\overline{U}\,\overline{V}}{\partial y} = -gD\frac{\partial H}{\partial x} - \tau_b + \frac{\partial D\overline{T}_{xx}}{\partial x} + \frac{\partial D\overline{T}_{xy}}{\partial y} \qquad (A.1)$$

where x, y are the streamwise and transverse coordinates, $\overline{U}, \overline{V}$ are the time- and depth-averaged streamwise and transverse velocities, D is the water depth, H the water level above an arbitrary horizontal reference plane, τ_b the bottom shear stress, parameterised as $\tau_b = c_f\rho\overline{U}|\overline{U}|$, with c_f the bottom friction coefficient, $\overline{T}_{xx}$ the sum of depth averaged downstream normal stresses and $\overline{T}_{xy}$ the sum of the depth averaged transverse shear stresses due

to advective dispersion, turbulence and viscosity (Vreugdenhil, 1994). Capitals indicate time-averaged quantities and the overline denotes the depth-averaging operator.

In this paper streamwise uniform flows are studied, in which $\partial H/\partial x = \partial z_b/\partial x = -S_0$, with z_b the bottom elevation and S_0 the bottom slope and $\overline{V} = 0$ due to impermeable lateral boundaries. The remaining downstream derivatives are zero. The balance for the streamwise momentum (A.1) then reduces to

$$gDS_0 - c_f\overline{U}|\overline{U}| = -\frac{\mathrm{d}D\overline{T}_{xy}}{\mathrm{d}y} \tag{A.2}$$

in which the depth-averaged transverse shear stress (transverse exchange of downstream momentum) is given by

$$\overline{T}_{xy} = -\overline{(U - \overline{U})(V - \overline{V})} - \overline{\langle uv \rangle} \tag{A.3}$$

in which $-\overline{\langle uv \rangle}$ is the depth averaged Reynolds stress with u and v the streamwise and transverse velocity fluctuations and the brackets representing the time-averaging operator. Here we have neglected the viscous contribution relative to the depth averaged Reynolds stress, which is justified for sufficiently high Reynolds numbers. The left-hand-side of equation (A.2) can be interpreted as the deviation of the flow from an equilibrium channel flow without transverse exchange. The right-hand-side represents the transverse exchange of streamwise momentum between the channel and the floodplain, with $\overline{T}_{xy}$ given in equation (A.3), consisting of a contribution by the advective dispersion and the Reynolds stress. If this exchange is small, the flow tends to the solution of two separated channels. The transverse momentum exchange is the only term left to be modeled.

Existing models for transverse exchange of momentum

A variety of models for estimating the transverse momentum exchange in compound channels has been proposed in the literature. It is not our aim to discuss all of them here. Only five different models are chosen, see Table A.1.

A constant eddy viscosity was adopted by Ogink (1985). It turned out that a constant value of $\nu_t = 0.5$ m^2/s could be used for a branch of the River Rhine.

A mixing length approach was proposed by Alavian&Chu (1985), using the mixing layer width δ as length scale and the velocity difference between the channel and the floodplain $\Delta\overline{U}$ as velocity scale. They assume that horizontal coherent structures are the dominant mechanism for momentum exchange. The necessary empirical constant is in the range of the values found for mixing layers.

Lambert&Sellin (1996) also employed a mixing length approach, but they used the water depth as a length scale, suggesting that the bottom turbulence is playing a major role. The specific characteristics of compound channel flow are not reflected in this approach.

Secondary circulations are modeled by Shiono&Knight (1991) in combination with an Elder formulation for the contribution of bottom turbulence. However, the contribution

of the secondary circulation was switched off at the slope between the channel and the floodplain and taken into account in the channel and on the floodplain only. This is surprising because, if secondary circulations play a role, it will be in the mixing region (Tominaga & Nezu, 1991). The range of the empirical constant λ used in the Elder formulation (see Table A.1 for a definition and numerical values) is very high and not in agreement with the range found for simple straight channel flow. $\lambda \simeq 0.05 - 0.2$, for which the Elder formulation has a physical basis.

Secondary circulations were also modeled by Ervine et al. (2000), in combination with an Elder formulation. Their contribution is maximal in the mixing region as it scales with the gradient of the squared velocity. The possible contribution of secondary circulations is discussed later in this paper.

After tuning, all the aforementioned models give a fairly good estimate for the transverse profile of the depth-averaged mean streamwise velocity, despite differences in underlying mechanisms and the way these are modeled. Yet not all models are sufficiently credible. For example, changing the water depth will not influence the transverse exchange in the model of Alavian&Chu (1985), where it will change the momentum exchange if we use the model of Shiono&Knight (1991). On the other hand, the model of Shiono&Knight (1991) contains the bottom slope (S_0), which is present in none of the other models.

A striking feature found in the experiments of Knight&Shiono (1990) is the very high eddy viscosity on the floodplain, close to the interface (see Figure A.7 below). Such a phenomenon cannot be modeled with an Elder formulation, nor with a conventional mixing length model, unless the empirical parameters are changed dramatically and on an *ad hoc* basis. The models mentioned above are therefore expected to be applicable only in the parameter range in which they were calibrated.

Table A.1: Selected existing models for transverse exchange of streamwise momentum.

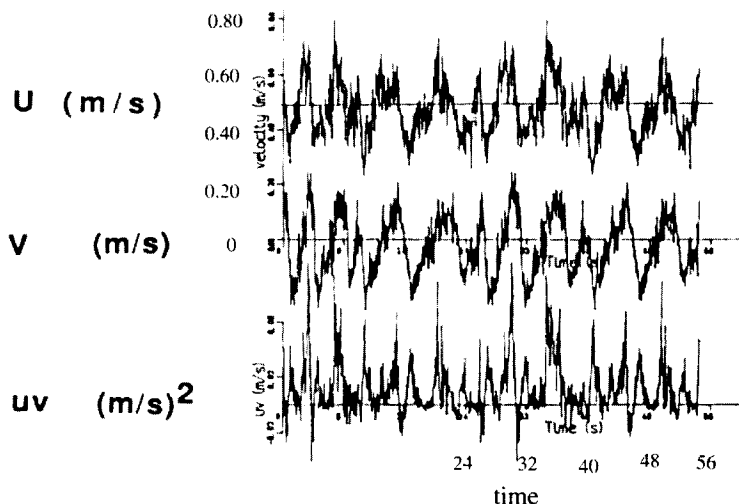| author	$\overline{T}_{xy}$	constants
Ogink 1985	$\nu_t \frac{\mathrm{d}\overline{U}}{\mathrm{d}y}$	$\nu_t = 0.5$ [m²/s]
Alavian&Chu1985	$\lambda \Delta \overline{U} \delta \frac{\mathrm{d}\overline{U}}{\mathrm{d}y}$	$\lambda = 0.05..0.15$
Shiono&Knight1991	$\lambda u_* D \frac{\mathrm{d}\overline{U}}{\mathrm{d}y} - \int_{y_1}^{y_2} \Gamma g S_0 \mathrm{d}y$	$\lambda = 0.07..40$, $\Gamma = -0.25..0.15$
Lambert&Sellin1996	$(C_{ml}D)^2 \frac{\mathrm{d}\overline{U}}{\mathrm{d}y} \left\| \frac{\mathrm{d}\overline{U}}{\mathrm{d}y} \right\|$	$C_{ml} = 0.6$
Ervine et al 2000	$\lambda u_* D \frac{\mathrm{d}\overline{U}}{\mathrm{d}y} - K \overline{U}^2$	$\lambda = 0.07..0.5$, $K = 0..0.04$

Figure A.2: Timeseries of the streamwise and transverse velocity (u and v) and their product (uv), from Knight&Shiono (1990) with permission of *Journal of Hydraulic Research*.

Modeling the transverse momentum exchange

It is well known (for example: Sellin (1964) and Van Prooijen&Uijttewaal (2002a)) that coherent structures develop in a shallow mixing region, with length and time scales much greater than those of the bottom induced turbulence. They are also present in the experiments of Knight&Shiono (1990). Figure A.2 shows the time signal of the streamwise and transverse velocity and the cross product of the streamwise and transverse velocity fluctuations from one of their measurements. A large scale motion can be clearly distinguished with superposed on it a small scale fluctuation which is due to bottom induced turbulence. The effects of this large scale motion and the small scale bottom turbulence are considered important and have to be taken into account in the modeling of the transverse momentum exchange. We shall initially neglect the contribution from advective dispersion, but we return to that later. The depth averaged turbulent shear stress is thus assumed to account for the total momentum exchange: $T_{xy} \approx -\overline{\langle uv \rangle}$.

To model the turbulent shear stress, we adopt the eddy viscosity concept, or Boussinesq approach:

$$-\overline{\langle uv \rangle} = \nu_t \frac{d\overline{U}}{dy} \tag{A.4}$$

with ν_t the eddy viscosity. The determination of the momentum exchange is shifted to the determination of a proper eddy viscosity. Following Wormleaton (1988), the eddy viscosity is split into two components: a contribution due to bottom turbulence (ν_t') and a

contribution due to transverse shear (ν_t'').

$$\nu_t = \nu_t' + \nu_t'' \tag{A.5}$$

Both contributions are modeled as the product of a typical length and velocity scale, $\mathcal{L}\mathcal{U}$, associated with the underlying mechanisms. The contribution due to lateral shear is assumed here to be caused by the horizontal coherent structures as visualized by the large scale fluctuations in the time signal of Figure A.2. In view of the schematized approximation we propose in this paper, the interaction between the horizontal coherent structures and the bottom turbulence is neglected.

For the bottom turbulence part, the Elder formulation is adopted, whith the water depth as the length scale ($\mathcal{L} = D$) and the friction velocity as the velocity scale ($\mathcal{U} = U_* = \sqrt{c_f}\overline{U}$):

$$\nu_t'(y) = \alpha D \sqrt{c_f}\overline{U} \tag{A.6}$$

with α a constant of the order 10^{-1} (Fischer *et al.*, 1979).

The contribution of the horizontal coherent structures to the total momentum exchange is modeled by means of Prandtl's mixing length model. This model turns out to work well for free shear flows (Tennekes & Lumley, 1972), if the length scale is taken proportional to the width of the mixing region δ. Accordingly, we write:

$$\nu_t''(y) = \beta^2 \, \delta^2 \left| \frac{\mathrm{d}\overline{U}}{\mathrm{d}y} \right| \tag{A.7}$$

in which β is a proportionality constant. As shown in Pope (2000) the turbulent eddy viscosity in the center of a developing plane turbulent mixing layer can be approximated by $\nu_t \simeq 0.156\delta\Delta\overline{U}S$, with the spreading rate $S = \mathrm{d}\delta/\mathrm{d}x \simeq 0.05 - 0.10$. The associated values of β would then be in the range $0.088 - 0.124$.

The width of the mixing layer is determined as indicated in Figure A.3. The distance between the position $y_{25\%}$, where $\overline{U}(y_{25\%}) = \overline{U}_f + 0.25(\overline{U}_c - \overline{U}_f)$ and $y_{75\%}$, where $\overline{U}(y_{75\%}) = \overline{U}_f + 0.75(\overline{U}_c - \overline{U}_f)$, determines half the mixing layer width:

$$\delta = 2(y_{75\%} - y_{25\%}) \tag{A.8}$$

This definition allows a possible asymmetry in the velocity profile.

The conventional mixing length approach applies to mixing layers with a constant depth and does not account for lateral depth variation, although that has considerable consequences for the large scale vortices. As demonstrated in Sellin (1964) and Tamai (1986), the coherent structures move partly in the main channel and partly on the floodplain. Considering the motion within a single vortex in a simplified way, it can be seen that the transverse component of the velocity of the coherent structure at the front (downstream) part is in the direction from the main channel onto the shallow floodplain. In view of continuity the transverse component of the velocity of the coherent structure will therefore increase roughly inversely proportional to the local water depth ($1/D(y)$). In the same

way, it can be argued that the transverse component of the velocity of the coherent structure at the back (downstream side) of the coherent structure will decrease proportional with $1/D(y)$. A sketch of this concept is given in Figure A.4.

In order to account for these variations in lateral velocity in the coherent structures, an extra factor which depends on the local water depth is incorporated in the model for ν_t'', changing the expression of equation A.7 to:

$$\nu_t''(y) = \frac{D_m}{D(y)}\beta^2\,\delta^2 \left|\frac{\mathrm{d}\overline{U}(y)}{\mathrm{d}y}\right| \tag{A.9}$$

in which $D(y)$ is the local water depth and D_m is the mean water depth: $D_m = (D_c + D_f)/2$.

The total eddy viscosity is now determined by the sum of equation (A.6) and equation (A.9):

$$\nu_t = \alpha\sqrt{c_f\overline{U}}D + \frac{D_m}{D}(\beta\delta)^2\frac{\mathrm{d}\overline{U}}{\mathrm{d}y} \tag{A.10}$$

Substituting this total eddy viscosity in equation (A.2), using equations (A.3) and (A.4) as intermediate steps, results in:

$$gDS_0 - c_f\overline{U}|\overline{U}| = -\frac{\mathrm{d}}{\mathrm{d}y}\left(D\nu_t\frac{\mathrm{d}\overline{U}}{\mathrm{d}y}\right) \tag{A.11}$$

The depth averaged mean streamwise velocities in the channel ($\overline{U}_c$) and on the floodplain ($\overline{U}_f$), far from the mixing region, are used as boundary conditions to this second-order nonlinear ordinary differential equation:

$$\overline{U}(y_c) = \overline{U}_c \quad , \quad \overline{U}(y_f) = \overline{U}_f \tag{A.12}$$

The equations (A.8), (A.10), (A.11) and (A.12) form a closed set, requiring as input a depth profile $D(y)$ and values for the coefficients c_f, α and β. With this input, equation
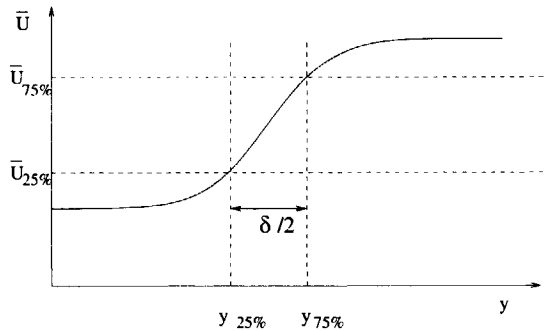

Figure A.3: Definition sketch for the determination of the width of the mixing layer δ.
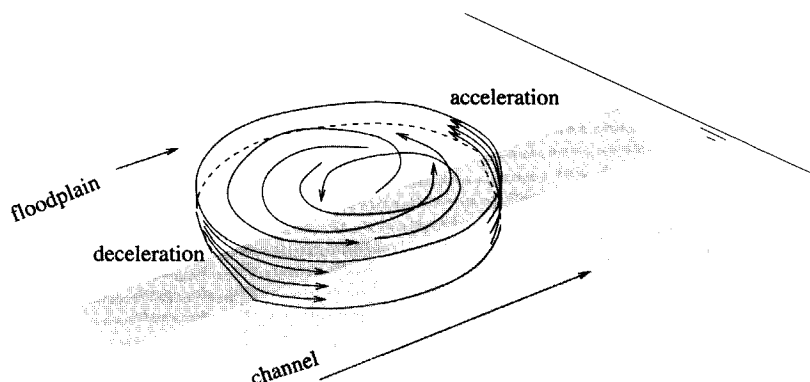
Figure A.4: Sketch of a vortex moving on an uneven bottom. The transverse velocity increases at the front and decreases at the back of the vortex.

(A.11) can be integrated. We used a Newton iteration method. The iteration starts with an assumed tanh-profile for the streamwise velocity $\overline{U}(y)$, with an initial value of δ equal to the width of the transition between channel bottom and floodplain bottom. The width of the mixing layer as determined from the profile in each iteration step according to equation (A.8) is used as a known constant in the next step. The profile evolves to a final form which is independent of the initial profile.

Comparison with FCF data

The results of the closure model described above will now be compared with the SERC Flood Channel Facility data (FCF). The FCF is a large scale flow facility (56 m long and 10 m wide) at HR Wallingford for studying compound channel flows. A number of cases (series A) concerned flow in straight, prismatic compound channels. The four best documented cases of these (Series 02) are used here to validate the model. These differ in water level, as indicated with the relative water depth $Dr = D_f/D_c$. The bottom slope was constant and common to all cases: $S_0 = 1.027 \ 10^{-3}$. Details can be found in Knight&Shiono (1990).

The constants α and β in equation (A.11) are the same for all four cases. The constant α is set *a priori* to $\alpha = 0.10$ according to for example Fischer et al. (1979). The constant β has to be in the range of $\beta = 0.088 - 0.124$ for unbounded mixing layers, according to Pope (2000). After tuning, a value of $\beta = 0.07$ is chosen here for an optimum fit for all four cases. It is noted that this weak tuning was the only fitting required for the prediction of the profiles of the depth averaged mean streamwise velocity, transverse shear stress and eddy viscosity for four different cases. The data used here have been obtained from four different papers. The profiles of the depth-averaged mean streamwise velocities

Table A.2: Flow conditions of the FCF experiments: $\overline{U}$ and D from Ervine et al. (2000) and Lambert&Sellin (1996), c_f from Equation A.13. (Knight & Shiono, 1990; Shiono & Knight, 1991; Wormleaton, 1996)

Dr[-]	D_c(mm)	$\overline{U}_c$(m/s)	D_f(mm)	$\overline{U}_f$(m/s)	$c_{f,c}$[-]	$c_{f,f}$[-]
0.11	169	0.85	19	0.25	0.0023	0.0030
0.15	177	0.86	27	0.30	0.0023	0.0029
0.20	188	0.90	38	0.45	0.0023	0.0018
0.25	200	0.92	50	0.45	0.0023	0.0023

have been obtained from Lambert&Sellin (1996) for Cases Dr=0.15 and 0.20 and from Ervine et al. (2000) for Cases Dr=0.11 and 0.25. The profiles of the transverse depth-averaged turbulent shear stress and the transverse profiles of the eddy viscosities have been taken from Knight&Shiono (1990). The bottom shear stresses have been obtained from
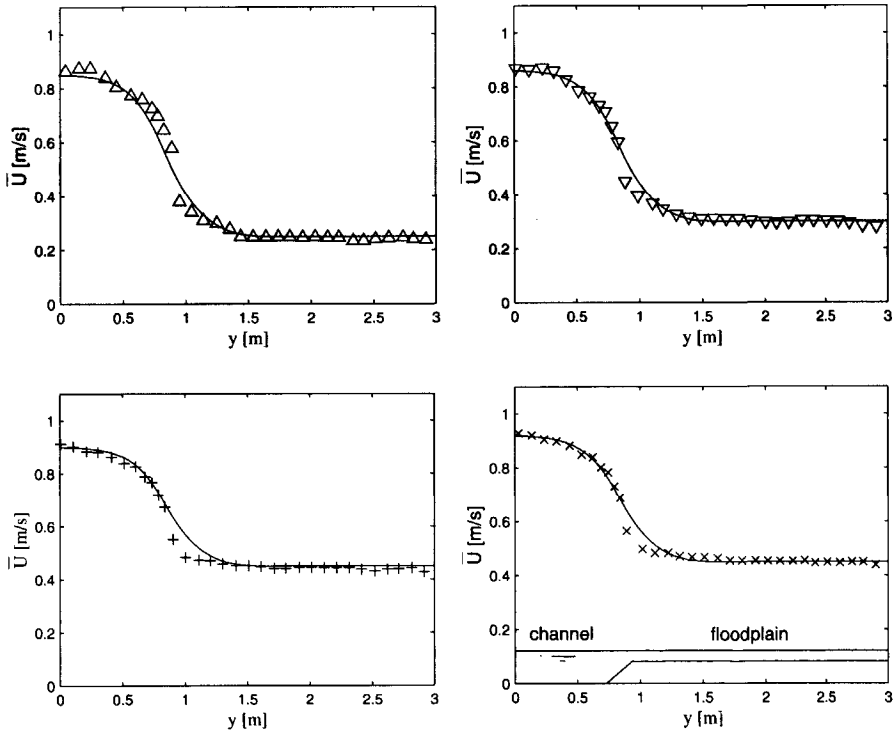

Figure A.5: Transverse profiles of the measured depth averaged mean streamwise velocity for the cases Dr=0.11($\triangle$), 0.15 ($\triangledown$), 0.20 (+) and 0.25 ($\times$) (Lambert & Sellin, 1996; Ervine *et al.*, 2000). The solid lines represent the modeled profiles. The cross section is shown in the lower right panel.

Shiono&Knight (1991). Relevant flow characteristics are summarized in Table A.2.

The bottom friction parameter c_f is here determined separately for the main channel and for the floodplain according to equation A.13:

$$c_{f.f} = \frac{gD_fS_0}{\overline{U_f}^2} \quad , \quad c_{f.c} = \frac{gD_cS_0}{\overline{U_c}^2} \tag{A.13}$$

These definitions ensure that in our model the pressure gradient and the bottom friction balance outside the mixing layer, i.e. in the transversely uniform zones.

At the interface, c_f is determined by linear interpolation between the values of the channel and the floodplain. This is justified according to the measured friction factor (Knight&Shiono (1990), Figure 17).

Figure A.5 shows a comparison between the modeled and measured transverse profiles of the depth-averaged mean streamwise velocity. They are in good agreement. The velocity on the floodplain close to the interface is somewhat overestimated, especially for the cases Dr=0.20 and 0.25.
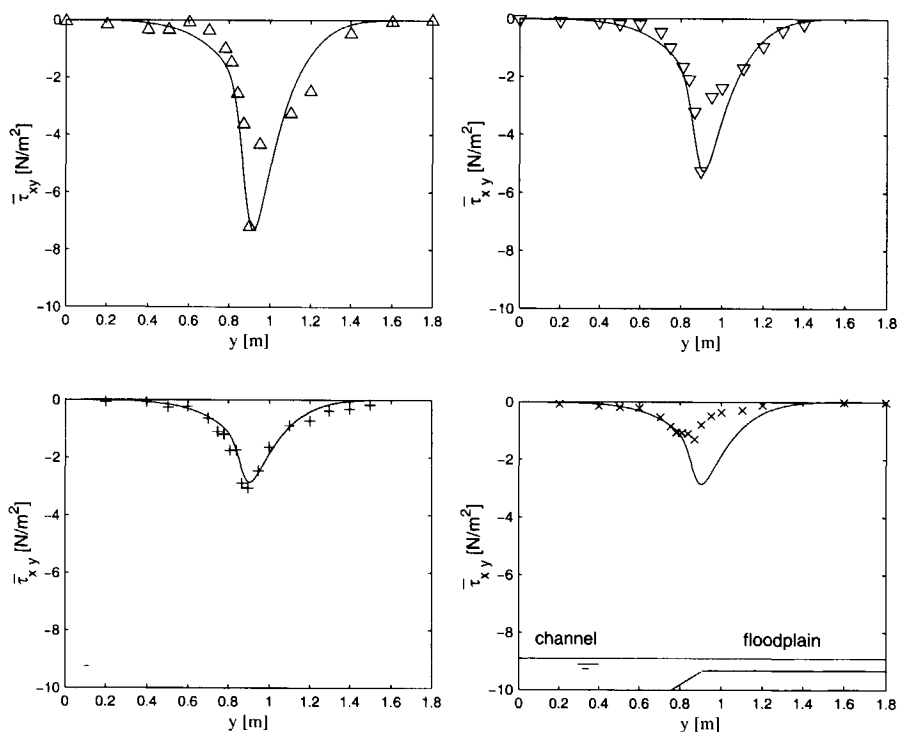

Figure A.6: Transverse profiles of measured (Knight & Shiono, 1990) and modeled depth averaged transverse shear stress, see Figure A.5 for caption.

The modeled and the simulated depth-averaged transverse shear stress profiles are plotted in Figure A.6. The measured values are obtained from averaging the transverse shear stresses obtained from several measurement points over the depth (Knight&Shiono (1990), Figure 14). There is a fair agreement for the cases Dr=0.11, 0.15 and 0.20. The peak is well represented as well as the asymmetry between the channel and the floodplain. The shear stress in case Dr=0.25 is overestimated.

The eddy viscosity is plotted in Figure A.7. The simulated profiles agree with the experimental data in a qualitative sense. In particular the higher value on the floodplain when compared with the main channel, and the decrease further onto the floodplain, are well reflected in the results. So is the location of the maximum eddy viscosity on the floodplain side of the interface. The good reproduction of this characteristic lateral profile of the eddy viscosity is due to our depth-dependent modeling of the contribution from the coherent structures. However, the eddy viscosity is overestimated in the main channel and underestimated on the floodplain for all cases. Obviously, more details should be included in order to obtain better quantitative agreement.

The contributions of the two mechanisms to the total modeled eddy viscosity are shown in Figure A.8 for the cases $Dr = 0.11$ and $Dr = 0.25$. On the floodplain the horizontal coherent structures dominate. In the main channel the bottom turbulence part plays an important role, as the depth is relatively large and the velocity relatively high compared to the floodplain. It is also seen that the influence of the horizontal coherent structures reduces with increasing relative depth while the influence of the bottom turbulence increases.

Overall, the agreement is good, taken into account the simplicity of the model. Admittedly, the proportionality coefficients in the eddy viscosity model have been optimised on the basis of the same FCF data, implying some degree of calibration, but it must be noted that this required only a minor adjustment of the conventional values found in classical literature. Moreover, using the same values for all the cases presented gave good predic-
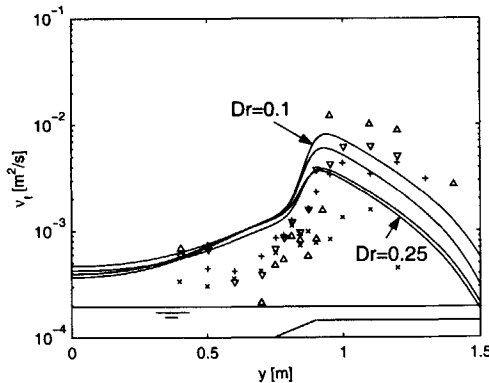

Figure A.7: Transverse profiles of the measured (Knight & Shiono, 1990) and modeled effective eddy viscosity ν_t, see figure A.5 for caption.
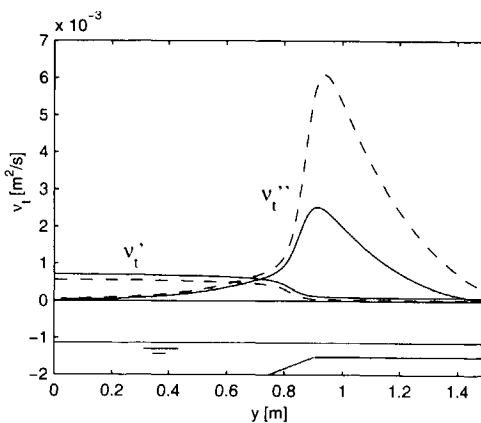
Figure A.8: The modeled effective eddy viscosity of the bottom turbulence ν'_t and the horizontal coherent structures ν''_t for the Cases $Dr = 0.11$ (- -) and $Dr = 0.25$ (–).

tions of the cross-flow *profiles* of downstream velocity and lateral shear stress, which is an aspect of validation. The good results obtained lend credibility to the model.

Secondary circulations

According to Shiono&Knight (1991), secondary circulations in the Flood Channel Facility play a role in the lateral momentum exchange in the mixing region, and they would account for an imbalance between the pressure gradient and the bottom friction in the transversely uniform zones. However, Shiono&Knight (1991) did not verify this on the basis of measured secondary flow velocities. The secondary flow velocity required to explain the observed imbalance is estimated below and compared to the expected and the observed values, based on the following consideration. If secondary circulations are to play a significant role in the momentum exchange in the mixing region, their contribution should be of the same order of magnitude as the turbulent Reynolds stress. Knowledge of the latter then allows an estimate of the strength of the secondary flow velocities required to achieve this equivalence. To quantify this, we use essentially the same procedure as followed by Wormleaton (1996) in an analysis of the flow in the laterally uniform regions on the floodplain.

The streamwise velocity is assumed to follow a logarithmic profile (Knight & Shiono, 1990; Sofialidis & Prinos, 1999). Wormleaton (1996) has in fact shown that this holds in good approximation for most FCF Series A data. The profile of the transverse velocity is more difficult to determine as (to the authors' knowledge) no experimental data were published for the vertical profile of the mean transverse velocity in the FCF. For an order of magnitude estimation, which is all that is required for the present purpose, we use a simple half-cosine approximation for the transverse secondary velocity. This leads to the
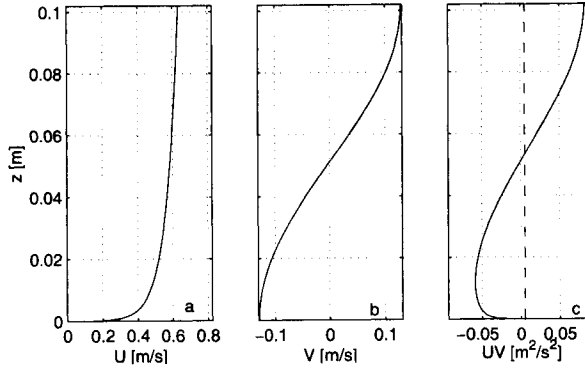
Figure A.9: Vertical profiles of the streamwise velocity $U(z)$, transverse velocity $V(z)$ ($\hat{V} = 0.15$m/s) and the product $U(z)V(z)$. The dashed line indicates the depth averaged product $\overline{UV}$.

following formulation for the advective dispersion due to the secondary circulations, using $\overline{V} = 0$ (see also Figure A.9):

$$-\rho\overline{UV} = -\rho \int_{z_b}^{z_b+D} \underbrace{\frac{\overline{U}\sqrt{c_f}}{\kappa} \ln\left(\frac{z}{z_0}\right)}_{U(z)} \underbrace{\left(-\hat{V}\cos\left(\pi\frac{z}{D}\right)\right)}_{V(z)} \; \mathrm{d}z \qquad (A.14)$$

with $\kappa = 0.41$ the Von Karman constant, z_0 the elevation above the bed where the (extrapolated) logarithmic velocity profile goes through zero (determined from the relation $1/\sqrt{c_f} = \kappa^{-1}\ln(e^{-1}D/z_0)$, or $z_0 = D\exp(-\kappa/\sqrt{c_f} - 1)$, using the local friction coefficient c_f and depth D), and $\hat{V}$ the maximum value of the transverse mean velocity.

Figure A.9 shows the two velocity profiles $U(z)$ and $V(z)$ as well as the resulting product $U(z)V(z)$ and its depth-averaged value. Note that the latter is an order of magnitude smaller than the product $\overline{U}\hat{V}$. If the stress due to advective dispersion is important in the mixing region, it should be of the same order of magnitude as the Reynolds stress: $-\rho\overline{UV} = \mathcal{O}(\overline{\tau}_{xy})$. In order to get an estimate of the secondary motion that is required for such a resulting advective dispersion, we take Case $Dr = 0.15$ as an example. According to Figure 10 of Shiono&Knight (1991), the apparent imbalance is highest at the interface just on the floodplain ($y = 0.90$m). Therefore we estimate the required strength of the secondary circulation at this position. At $y = 0.90$m the depth is $D = 27$mm, the mean streamwise velocity is $\overline{U} = 0.45$m/s (Figure A.5), the depth-averaged turbulent shear stress is $\overline{\tau}_{xy} = -5.25$N/m^2 (Figure A.6) and the bottom friction coefficient on the floodplain is $c_{f,f} = 0.0029$ (Table A.2). These values are substituted in equation A.14, which results in a required maximum transverse velocity $\hat{V} = 0.15$m/s. This is one order of magnitude greater than the observed values, which are 2cm/s at most (Shiono&Knight (1991), Figure 11). It is concluded that the influence of the secondary circulations on the momentum exchange in the mixing region can be neglected.

Conclusions

In this paper the momentum exchange in straight uniform compound channel flow is studied. Different mechanisms that could play a role have been investigated. It turned out that the momentum exchange is dominated by the horizontal coherent structures and the bottom turbulence. Secondary circulation turns out to be of minor importance.

A new eddy viscosity model is proposed, in which the horizontal coherent structures and the bottom turbulence are incorporated. The bottom turbulence is modeled with an Elder formulation and the contribution of the horizontal coherent structures by a modified mixing length approach which takes into account the effect of transverse depth variation on the coherent structures. The results obtained with the proposed model are in good agreement with the Flood Channel Facility data. The modeled depth averaged mean streamwise velocities and the depth averaged transverse shear stresses are in good agreement with the measured profiles. The peak of the eddy viscosity on the floodplain is well reproduced due to the inclusion of the influence of the depth variation on the large coherent structures. The proposed model still needs two empirical constants, which however have their origin in the fundamental flow types, wall flow and mixing layer flow, with corresponding realistic values.

The developed model can be used for the prediction of the stage-discharge relation of straight uniform compound channels, in a similar way as performed by Lambert&Sellin (1996). An other application is the implementation of the eddy viscosity model in one-dimensional conveyance models as used in the practice of civil engineering.

Although the model turned out to work well, we do not claim that it can be used for a very wide range of applications. The present investigation was restricted to straight uniform compound channels, with a mild slope on the interface. In case of meandering, roughened floodplains, steep slopes (or vertical walls) at the interface, or non-uniformity it should be reconsidered what mechanisms dominate the momentum exchange.

Further study is required to validate the assumptions on the local stretching and compressing of the coherent structures, the interaction between the horizontal coherent structures and the bottom turbulence and the general applicability of the estimated parameter values. Sophisticated numerical modeling is recommended for such further research.

Acknowledgments

Notation

c_f	=	friction coefficient
C_{ml}	=	coefficient used by Lambert & Sellin (1996)
D	=	depth
D_m	=	mean depth $(D_f + D_c)/2$
Dr	=	relative depth D_f/D_c
g	=	gravitational acceleration
H	=	waterlevel
Δi	=	streamwise gradient of water depth
K	=	coefficient used by Ervine et al. (2000)
S	=	spreading rate of a developing mixing layer
S_0	=	bottom slope
T	=	stress
u	=	streamwise velocity fluctuation
u_*	=	friction velocity
U	=	time-averaged streamwise velocity
v	=	transverse velocity fluctuation
V	=	time-averaged transverse velocity
W	=	width
x	=	streamwise coordinate
y	=	transverse coordinate
z	=	vertical coordinate
z_0	=	integration constant
α	=	coefficient in eddy viscosity due to bottom turbulence
β	=	coefficient in eddy viscosity due to large horizontal structures
δ	=	mixing layer width
κ	=	Von Karman constant
λ	=	coefficient used by Alavian&Chu (1985)
λ	=	coefficient used by Shiono&Knight (1991)
ν_t	=	total eddy viscosity
ν_t'	=	eddy viscosity due to large horizontal structures
ν_t''	=	eddy viscosity due to bottom turbulence
ρ	=	mass density
τ	=	bottom shear stress
Γ	=	coefficient used by Shiono&Knight (1991)

Subscripts
b	=	bottom
c	=	main channel
f	=	floodplain

References

Alavian, V. and Chu, V.H. (1985). "Turbulent exchange flow in shallow compound channel." *Proc. 21st IAHR Congress,* Melbourne, Australia, 446 451.

Barishnikov N.B. and Ivanov G.V. (1971). "Role of flood plain in flood discharge of a river channel." *Proc. 14th IAHR Congress,* Paris, France, 141–144.

Cramp A., Coulson M., James A. and Berry J. (1991). "A note on the observed and predicted flow patterns around islands - Flat Holm, the Bristol Channel." *Int. Journal Remote Sensing.* 12(5).1111-1118.

Dracos T., Giger M. and Jirka G.H. (1992). "Plane turbulent jets in a bounded fluid layer." *Journal of Fluid Mechanics.* 214, 587 614.

Ervine D.A., Babaeyan-Koopaei K. and Sellin R.H.J. (2000). "Two-dimensional solution for straight and meandering overbank flows." *Journal of Hydraulic Engineering,* 126(9), 653–669.

Fischer H.B., List E.J. Koh R.C.J., Imberger J. and Brooks N.H. (1979). "Mixing in inland and coastal waters". Academic Press, New York, US.

Ikeda S. Kawamura K. Toda Y. and Kasuya I. (2002). "Quasi-three-dimensional computation and laboratory tests on flow in curved compound channels." *Proc. Riverflow 2002,* Louvain-la-Neuve, Belgium, 233-245.

Kinoshita H. (1984). "Present status and future prospects of river flow analysis by aerial photography." *Proc. Japan Society of Civil Engineers* 345, 31–40.

Knight D.W. and Shiono K. (1990). "Turbulence measurements in a shear layer region of a compound channel." *Journal of Hydraulic Research,* 28(2), 175–196.

Lambert M.F. and Sellin R.H.J. (1996). "Discharge prediction in straight compound channels using the mixing length concept" *Journal of Hydraulic Research,* 34(3), 381–394.

Nadaoka K. and H. Yagi (1998). "Shallow-water turbulence modeling and horizontal large-eddy computation of river flow." *Journal of Hydraulic Engineering,* 124(5),493–500.

Ogink H.J.M. (1985). "The effective viscosity coefficient in 2-D depth-averaged flow models", *Proc. 21st IAHR Congress,* Melbourne, Australia, 475–479.

Sellin R.H.J. (1964). "A laboratory investigation into the interaction between the flow in the channel of a river and that over its flood plain." *La Houille Blanche,* 110, 689–789.

Shiono K. and Knight D.W. (1991). "Turbulent open channel flows with variable depth across the channel." *Journal of Fluid Mechanics*, 222, 617–646.

Sofialidis D. and Prinos P. (1998). "Compound open-channel flow modeling with nonlinear low-Reynolds k-ε models." *Journal of Hydraulic Engineering*, 124(3), 253–262.

Sofialidis D. and Prinos P. (1999). " Numerical study of momentum exchange in compound open channel flow." *Journal of Hydraulic Engineering*, 125(2), 237–255.

Tamai N., Aseada T. and Ikeda H. (1986). "Study on generation of periodical large surface eddies in a composite channel flow." *Water Resources Research*, 22(7),1129–1138.

Tennekes H. and J.L. Lumley (1972). "A first course in turbulence" *The MIT Press*, Cambridge, US.

Tominaga A. and Nezu I. (1991). "Turbulent structure in open compound channel flows." *Journal of Hydraulic Engineering*, 117(2), 21–41.

Uijttewaal W.S.J. and Booij R. (2000). "Effects of shallowness on the development of free-surface mixing layers." *Physics of Fluids*, 12(2), 392–420.

Van Prooijen B.C. and Uijttewaal W.S.J. (2002). "A linear approach for the evolution of coherent structures in shallow mixing layers." *Physics of Fluids*, 14(12), 4105–4114.

Vreugdenhil C.B. (1994). "Numerical methods for shallow-water flow." *Kluwer Academic Publishers*, Dordrecht, The Netherlands.

Wormleaton P.R. (1988). "Determination of discharge in compound channels using the dynamic equation for lateral velocity distribution." *Int. Conf. on Fluvial Hydraulics*, IAHR, Budapest, Hungary, 98–103.

Wormleaton P.R. (1996). "Coherent flow structures in open channels.", P.J. Ashworth and S.J. Bennet and J.L. Best and S.J. McLelland, eds, chapter "Floodplain secondary circulation as a mechanism for flow and shear stress redistribution in straight compound channels", John Wiley & Sons, Chichester, England, 581–608.

Appendix B

Notation

Roman symbols

c_f	friction coefficient
C	cross-covariance
C_s	Smagorinsky coefficient
D	depth
E	energy density spectrum
f	frequency
f_1	shape function
f_2	shape function
F	amplification function
Fr	Froude number
g	gravity
k	wave number
$\mathcal{L}$	typical length scale
L	typical length scale
n	counter
N	integer
p	pressure
P	time-averaged pressure
Q	Weiss function
Re	Reynolds number
S	bottom friction parameter
S_c	critical bottom friction parameter
T	duration
Δt	time step
u	streamwise velocity
$\hat{u}$	streamwise velocity amplitude
u_*	friction velocity
u'	intensity of large scale streamwise velocity fluctuations
u''	intensity of small scale streamwise velocity fluctuations

u_i	velocity in direction i
U	time-averaged streamwise velocity
U_1	streamwise velocity on high velocity side
U_2	streamwise velocity on low velocity side
U_c	streamwise velocity in the center of a mixing layer
ΔU	velocity difference over a mixing layer
$\mathcal{U}$	typical velocity scale
v'	intensity of large scale transverse velocity fluctuation
v''	intensity of small scale transverse velocity fluctuation
V	time-averaged transverse velocity
W	width
x	streamwise coordinate
Δx	grid spacing in streamwise direction
y	transverse coordinate
y_c	transverse position of the center of the mixing layer
Δy	grid spacing in transverse direction
z	spanwise coordinate
Δz	grid spacing in spanwise direction

Greek symbols

α	entrainment coefficient
α	emperical constant
β	emperical constant
δ	mixing layer width
δ	mixing layer width
Δ	mesh size
η	dimensionless transvers coordinate
κ	Von Karman constant
λ	emperical constant
ν	kinematic viscosity
ν_t	eddy viscosity
ρ	density
$theta$	angle
τ	time scale
τ_w	wall shear stress
τ^{SGS}	subgrid-scale shear stress
ω	vorticity
ω_i	growth rate
ω_r	frequency

ϕ phase shift

Subscipts

0	at the tip of the splitterplate
c	center of the mixing layer
ks	kinematic simulation
max	maximum
min	minimum

Abbreviations

2D	two dimensional
3D	three dimensional
DNS	Direct Numerical Simulation
HLES	Horizontal Large Eddy Simulation
LDA	Laser Doppler Anemometer
LES	Large Eddy Simulation
MKM	Moser, Moin and Mansour
PTV	Particle Tracking Velocimetry
RANS	Reynolds Averaged Navier Stokes
TRANS	Transient Reynolds Averaged Navier Stokes
TRANS+ks	Reynolds Averaged Navier Stokes with kinematic simulation
SDS-2DH	Sub Depth Scale 2-Dimensional Horizontal
SGS	SubGrid Scale
URANS	Unsteady Reynolds Averaged Navier Stokes
VLES	Very Large Eddy Simulation

Dankbetuiging

Curriculum Vitae

Bram van Prooijen werd op 6 april 1975 geboren te 's-Gravenhage. Het voorbereidend wetenschappelijk onderwijs volgde hij vanaf 1987 aan het Lambert Franckens College te Elburg. In 1993 werd begonnen aan de studie Civiele Techniek aan de Technische Universiteit Delft. Als afstudeerproject is experimenteel onderzoek gedaan naar de stroming in een rivier met uiterwaarden (een *compound channel*) onder leiding van de drs Booij en prof. dr ir De Vriend. In 1999 is begonnen aan het promotieproject onder begeleiding van prof. dr ir J.A. Battjes en dr ir W.S.J. Uijttewaal. In oktober 2003 werd het promotieproject afgerond met het voorliggende proefschrift *Shallow Mixing Layers*. Sinds november 2003 is Bram van Prooijen werkzaam als adviseur/onderzoeker bij Svašek Hydraulics.